Control of blood clotting using gold nanorods

by

Helena de Puig Guixé

Industrial Engineer (2011)

Institut Químic de Sarrià, Universitat Ramon Llull

Submitted to the Department of Mechanical Engineering

in partial fulfilment of the requirements for the degree of

Master of Science in Mechanical Engineering

at the

MASSACHUSETTS INSTITUTE OF TECHNOLOGY

June 2013

Author.....

Department of Mechanical Engineering

May 8th, 2013

Certified by.....

Kimberly Hamad-Schifferli

Visiting Scientist, Department of Mechanical Engineering

& Technical Staff, MIT Lincoln Laboratory

Thesis supervisor

Accepted by.....

David E. Hardt

Chairman, Department Committee on Graduate Students

Control of blood clotting using gold nanorods

by

Helena de Puig Guixé

Submitted to the Department of Mechanical Engineering, on May 8th,
in partial fulfilment of the requirements for the degree of
Master of Science in Mechanical Engineering

Abstract

We have developed a method to externally control blood clotting using gold nanoparticles. Gold nanorods (NRs) have unique size and shape-dependent optical properties that can be used for externally controlled release of biomolecules by laser excitation. Femtosecond pulsed laser irradiation at the NR longitudinal surface plasmon resonance peak (LSPR) can excite the NRs and induce melting, and thus cause release of drug or biomolecular payload on the NR. Because the peak wavelength of the LSPR changes with NR aspect ratio, NRs with different aspect ratios can be independently excited at different wavelengths to release different payloads in a mutually exclusive fashion. This approach can be used to create a biological switch for blood clotting by releasing a single stranded (ssDNA) thrombin binding aptamer (TBA) upon laser irradiation. It is possible to control blood clotting by releasing TBA that binds and inhibits thrombin, and an antidote consisting of a complementary ssDNA sequence that binds to TBA and restores thrombin activity. Both the TBA and the antidote are loaded onto NRs with different aspect ratios. This enables us to use laser excitation at one wavelength to deliver the TBA and inhibit thrombin and consequently blood clotting. We then use a different wavelength to deliver the antidote and reverse the effect of the TBA. We use covalent attachment techniques (thiol-gold binding) for loading the ssDNA

on the NRs and study the interface between the NRs and the biomolecules. We also take advantage of serum protein coronas for loading, which enable enhanced loading capacities. This localized, selective and externally controlled release of biomolecules represents an advance that could impact a number of biological applications, where the current practice is systemically administering drugs though the whole bloodstream and relying on physiological clearance to restore the system.

Thesis supervisor: Kimberly Hamad-Schifferli

Title: Visiting Scientist, Department of Mechanical Engineering & Technical Staff, MIT Lincoln Laboratory

Acknowledgements

First of all, I would like to thank Prof. Kimberly Hamad-Schifferli, for her advise during the years I spent in her research group at MIT. Doing research with her has been a great learning experience, due to her kind character and her ability to discuss and share ideas, without those, this research project would have not been feasible. The time she has shared with me has a priceless value, as it has helped me grow both as a researcher and personally. I am as well thankful for the opportunities she has given me to present our work in conferences, both in the US and in Europe. These experiences are very important for my initiation in a research career.

I am grateful for having been able to work also in Prof. Lee Gehrke's lab. I am thankful for his lab support and also for the help I received from his research group, especially Chunwan, Ann, Irene and José.

I would also like to thank Prof. Mercedes Balcells and Prof. Salvador Borrós, who enabled me to contact Prof. Hamad-Schifferli on the first place. Prof. Mercedes Balcells, as a co-director of the MIT-Spain Program, welcomed me on my arrival in Boston; she has been a helpful guide during my stay at MIT.

I am very thankful for all the people I have worked with in the lab. Especially Anna Cifuentes and Paula Ciaurriz, for the hours we spent together in the lab ("¡felices

domingos de laboratorio!"); Dr. Salmaan H. Baxamusa who has taught me the basics of working in research. The rest of Hamad-Schifferli's group: Dr. James Kah, Dr. Stefania Federici, Dr. Niraj Sinha, Dr. Sunho Park, Edurne Tellechea and Prof. Paolo Bergese, for fruitful discussions and help throughout these years. I would also like to thank Dr. Zhichuan Xu, for taking amazing TEM pictures, and for his nice character. Also, the undergraduate students who have helped me in the lab: Helen D'Couto, Dorma C. Flemister, Nate Miska and Ashley Fletcher.

I thank our collaborators at MIT. First, Prof. Andrei Tokmakoff and his students: Sam, Aritra, Luigi, Paul, Carlos, Krupa and Kevin, for the use of their lasers. Prof. Kristala Jones-Prather, Prof. Krystyn Van Vliet, Prof. Moungi Bawendi, Prof. Alexandra A. Techet, for the use of their equipment. Also, the Center for Materials Science and Engineering (CMSE) and the Biophysical Instrumentation Facility (BIF), for the use of their equipment.

I would also like to thank Denise MacPhail and Joan Hutchins for assistance, and Obra Social La Caixa, for my postgraduate fellowship.

I would finally like to thank my parents, family and friends, who have greatly contributed to making this experience even more enjoyable, my roomates: Maria, Sagi, Nuria, Martu, Majo and Gemma, for fruitful philosophical discussions. I thank Bayridge residence and its staff, Irene and Sara. I thank my friends in "headquarters", Spain@MIT group and the IQS crew, especially Enrique, Marcel, Jose, and Jorge. Gràcies!

Table of contents

1. Introduction: On the control of blood clotting 25

1.1. Motivation 25

1.2. Objectives and strategies 28

1.3. Background 31

1.3.1. Gold nanoparticles 31

1.3.1.1. Surface chemistry 33

1.3.1.2. Optical properties 35

Nanoparticle assembly 38

Photothermal heating of gold nanorods 39

Selective photothermal heating of gold nanorods with different SPR 42

1.3.2. Thrombin and the coagulation cascade 45

1.3.2.1. Thrombin binding aptamer 48

1.4. Thesis outline 53

1.5. Bibliography 54

2. Materials and Methods 67

2.1. Synthesis of gold nanoparticles 67

2.1.1. Gold nanorods 67

2.1.2 Gold nanocapsules and Gold nanobones 68

2.1.3. Gold nanospheres 71

2.2. Loading of DNA on NPs by thiol chemistry 76

2.2.1. Ligand exchange of gold nanoparticles 76

2.2.2. Salt stability of the gold nanoparticles 81

2.2.3. DNA conjugation of gold nanoparticles 82

2.2.4. Surface modifications on the DNA-conjugated NRs 87

2.2.4.1. HSA block 87

2.2.4.2. PEG backfill 88

2.3. HS Corona conjugation on NP surfaces 90

Carbon nanotube solubilization and characterization 90

2.4. Laser Irradiation of NR 92

2.5. Blood clotting tests 93

2.7. Bibliography 94

3. Characterization of the covalently bound aptamer-NP conjugates 99

3.1. Introduction 99

3.2. Thermodynamic study of the binding of the aptamer-thrombin on the surface of a NP 101

3.2.1. Analysis methods 104

3.2.1.1. Langmuir isotherm 104

3.2.1.2. Van't Hoff equation 106

3.2.2. Theoretical 108

3.2.3. Results and discussion 113

3.2.3.1. Synthesis and characterization of TBA decorated NRs 113

3.2.3.2. Probing thrombin directed self-assembly 116

3.2.3.3. Nanomachinery of TBA on NRs 121

3.2.4. Conclusions 133

3.3. Kinetics of biomolecule-induced nanoparticle assembly 136

3.3.1. Theoretical 141

3.3.2. Results and discussion 141

3.3.2.1. Different surface chemistries 143

3.3.2.2. Different concentrations of biomolecule added 148

3.3.4. Conclusions 152

3.4. Reversible nanomachinery at the nanoparticle-biomolecule interface 154

3.4.1. Theoretical 155

3.4.2. Results and discussion 158

3.4.3. Conclusions 160

3.5. Quantifying DNA hybridization at the nanoparticle interface 161

3.5.1. Theoretical 162

3.5.2. Results and discussion 165

3.5.3. Conclusions 170

3.6. Conclusions 172

3.7. Bibliography 174

4. Release of covalently bound aptamers from NPs 183

4.1. Introduction 183

4.2. Melting the NR-CTAB and NB-CTAB 186

4.2.1. Melting NRs and NBs at their SPR 187

4.2.2. Control experiments with single NRs and NBs 188

4.2.3. Selective melting of a mixture of NRs and NBs 190

4.3. Release of thiolated ssDNA from NRs 193

4.3.1. Increasing the loading of thiolated TBA with intramolecular G-quadruplexes 193

4.3.2. Aptamers and antidotes effect in blood clotting 194

4.3.3. Melting and release of TBA from NRs 196

4.3.4. Effect of NPs in blood clotting time 199

4.4. Release of dsDNA from NRs 201

4.5. Conclusions 204

4.6. Bibliography 205

5. Increasing loading capacity: NR coronas 209

5.1. Introduction 209

5.2. Characterization methods for NR-coronas 211

5.3. Optimizing the protein corona 216

5.3.1. Different binding strategies and proteins 216

5.3.2. 5/5/5 Optimal Conditions 223

5.3.2.1. Effect of phosphate buffer 223

5.3.2.2. Effect of CTAB concentration 225

5.3.2.3. Effect of HS concentration 226

5.3.3 Effect of particle material on loading 227

5.4. Kinetics of formation of the protein coronas 229

5.5. Leakage from the NR-coronas 230

5.6. Conclusions 238

5.7. Bibliography 239

6. Switching on and off blood clotting with light 243

6.1. Introduction 243

6.2. Effect of TBA and antidote in thrombin clotting tests 247

6.3. Preparation and characterization of NR-coronas 249

6.4. Single laser irradiations for the release of TBA and antidote 253

6.5. Selective release of TBA and antidote for the control of blood clotting 257

6.4. Conclusions 262

6.5. Bibliography 263

7. Conclusions and future directions 267

7.1. Summary of the work 267

7.1.1. Limitations and further studies 271

7.1.2. Advantages 274

7.2. Future prospects and applications 276

7.2.1. Control of blood clotting using gold nanorods in vivo 276

7.2.2. Triggered release for combinational therapy 277

7.2.3. Switchable enhancement of *in vitro* translation with light 278

7.2.4. Nanobiomachinery and protein-NR / DNA-NR origamis 279

7.3. Bibliography 281

List of figures

Figure 1-1: Scheme 29

Figure 1-2: Published articles on nanotechnology since 1990. Searched "nanoparticle" in google scholar 32

Figure 1-3: Surface Plasmon Absorption of Spherical Nanoparticles[17] 36

Figure 1-4: Overview of the selective release[69]. Reprinted with permission from Wijaya A, Schaffer SB, Pallares IG, Hamad-Schifferli K. Selective Release of Multiple DNA Oligonucleotides from Gold Nanorods. ACS Nano 2008;3:80. Copyright 2008 American Chemical Society. 42

Figure 1-5: Absorbance and TEM image of the NRs and NB after irradiation[69]. Reprinted with permission from Wijaya A, Schaffer SB, Pallares IG, Hamad-Schifferli K. Selective Release of Multiple DNA Oligonucleotides from Gold Nanorods. ACS Nano 2008;3:80. Copyright 2008 American Chemical Society. 44

Figure 1-6: Fluorecense of the DNA released after the irradiation[69] Reprinted with permission from Wijaya A, Schaffer SB, Pallares IG, Hamad-Schifferli K. Selective Release of Multiple DNA Oligonucleotides from Gold Nanorods. ACS Nano 2008;3:80. Copyright 2008 American Chemical Society. 45

Figure 1-7: Coagulation cascade 46

Figure 1-8: TBA-thrombin cycle 52

Figure 2-1: TEM image and absorbance graph of synthesized NR 68

Figure 2-2: Extinction plot, TEM and histogram of the synthesized NC..... 70

Figure 2-3: Extinction plot and TEM of the synthesized NBs 71

Figure 2-4: TEM Histogram (left), DLS (middle) and extinction (right) of the synthesized NS 72

Figure 2-5: TEM images of the NS 73

Figure 2-6: Method for NR ligand exchange[17]. Adapted with permission from Wijaya A, Schaffer SB, Pallares IG, Hamad-Schifferli K. Selective Release of Multiple DNA Oligonucleotides from Gold Nanorods. ACS Nano 2008;3:80. Copyright 2008 American Chemical Society. 77

Figure 2-7: Gel electrophoresis of the NRs-CTAB; NRs-MUDA and NRs-MHDA 80

Figure 2-8: Gel electrophoresis of PEG-NRs 81

Figure 2-9: NR-CTAB; NR-MHA and NR-DNA 84

Figure 2-10: Secondary structure of the thrombin binding aptamer (TBA) 87

Figure 2-11: Gel of PEG-backfilled NRs 88

Figure 3-1: Thermodynamic cycle describing the assembly of NR-TBA in the presence of thrombin. Adapted with permission from de Puig H, Federici S, Baxamusa SH, Bergese P, Hamad-Schifferli K. Quantifying the Nanomachinery of the Nanoparticle-Biomolecule Interface. Small 2011;7. Copyright 2011 WILEY-VCH Verlag GmbH & Co. KGaA, Weinheim. 109

Figure 3-2: Samples probed. Adapted with permission from de Puig H, Federici S, Baxamusa SH, Bergese P, Hamad-Schifferli K. Quantifying the Nanomachinery of the Nanoparticle-Biomolecule Interface. Small 2011;7. Copyright 2011 WILEY-VCH Verlag GmbH & Co. KGaA, Weinheim. 116

Figure 3-3: Change in absorption spectra of NR-T_{15}-TBA high coverage as a function of time upon incubation with 121 nM of thrombin (arrow indicates increasing time). Adapted with permission from de Puig H, Federici S, Baxamusa SH, Bergese P, Hamad-Schifferli K. Quantifying the Nanomachinery of the Nanoparticle-Biomolecule Interface. Small 2011;7. Copyright 2011 WILEY-VCH Verlag GmbH & Co. KGaA, Weinheim....117

Figure 3-4: A400/A800 as a function of time for NR-T_{15}-TBA high coverage for different thrombin concentrations. Adapted with permission from de Puig H, Federici S, Baxamusa SH, Bergese P, Hamad-Schifferli K. Quantifying the Nanomachinery of the Nanoparticle-Biomolecule Interface. Small 2011;7. Copyright 2011 WILEY-VCH Verlag GmbH & Co. KGaA, Weinheim. 118

Figure 3-5: Aggregation isotherm for NR-T_{15}-TBA high coverage. Adapted with permission from de Puig H, Federici S, Baxamusa SH, Bergese P, Hamad-Schifferli K. Quantifying the Nanomachinery of the Nanoparticle-Biomolecule Interface. Small 2011;7. Copyright 2011 WILEY-VCH Verlag GmbH & Co. KGaA, Weinheim.....118

Figure 3-6: A400/A800 as a function of time upon incubation with thrombin (t = 0 min) and complementary DNA sequence (gray area, 60 min). Adapted with permission from de Puig H, Federici S, Baxamusa SH, Bergese P, Hamad-Schifferli K. Quantifying the

Nanomachinery of the Nanoparticle-Biomolecule Interface. Small 2011;7. Copyright 2011 WILEY-VCH Verlag GmbH & Co. KGaA, Weinheim. 119

Figure 3-7: A400/A800 of already formed NR-T_{15}-TBA -thrombin aggregates as a function of changing the temperature from 25^{o}C to 80^{o}C and back down to 25^{o}C (arrows indicate direction). Adapted with permission from de Puig H, Federici S, Baxamusa SH, Bergese P, Hamad-Schifferli K. Quantifying the Nanomachinery of the Nanoparticle-Biomolecule Interface. Small 2011;7. Copyright 2011 WILEY-VCH Verlag GmbH & Co. KGaA, Weinheim. 120

Figure 3-8: Modified Langmuir aggregation isotherms for a) NR-T_{15}-TBA high coverage, b) NR-T_{15}-TBA low coverage, c) NR-T_{15}-TBA mPEG backfill 0.5:1 mPEG:TBA, d) fits for plots a-c , e) NR-TBA without poly T spacer (the dashed line is the average value), f) NR-T_{15}-TBA HSA block (the dashed line is the average value), g) NR- T_{15}-TBA high coverage mPEG backfill 5:1 mPEG:TBA. Reprinted with permission from de Puig H, Federici S, Baxamusa SH, Bergese P, Hamad-Schifferli K. Quantifying the Nanomachinery of the Nanoparticle-Biomolecule Interface. Small 2011;7. Copyright 2011 WILEY-VCH Verlag GmbH & Co. KGaA, Weinheim. 124

Figure 3-9: a) ϑ vs. -W^{σ} for NR-T_{15}-TBA high coverage (square), NR-T_{15}-TBA low coverage (triangle), and NR-T_{15}-TBA -PEG backfill 0.5:1 (circle), b) ThT vs. - W^{σ} for NR-T_{15}-TBA high coverage (square), NR-T_{15}-TBA low coverage (triangle), and NR- T_{15}-TBA -mPEG backfill. Adapted with permission from de Puig H, Federici S, Baxamusa SH, Bergese P, Hamad-Schifferli K. Quantifying the Nanomachinery of the Nanoparticle-

Biomolecule Interface. Small 2011;7. Copyright 2011 WILEY-VCH Verlag GmbH & Co. KGaA, Weinheim. 126

Figure 3-10: Melting profile of the NR-thrombin conjugates and fitted model 132

Figure 3-11. Nanorod assembly kinetics scheme 137

Figure 3-12: Formation of the unit blocks of aggregation scheme 138

Figure 3-13: Subsequent monomer addition scheme 139

Figure 3-14: Overall kinetic scheme of NR assembly 139

Figure 3-15: Evolution of the extinction of the NRs with time 142

Figure 3-16: Assembly of the NRs at 121nm thrombin 142

Figure 3-17: Kinetic fits with different surface chemistries 144

Figure 3-18: Comparison of the fits between different surface chemistries 145

Figure 3-19: T_{15}-TBA high coverage kinetics at different thrombin concentrations 149

Figure 3-20: T_{15}-TBA low coverage kinetics at different thrombin concentrations 150

Figure 3-21: PEG Backfill kinetics at differetn thrombin concentrations 151

Figure 3.22: Thrombin-TBA nanomachine 155

Figure 3.23: Thermodynamic cycle of NRs disassembly 157

Figure 3-24: Reverisble assembly of NRs after the addition of thrombin and anti-TBA 159

Figure 3-25: Disassembly of NRs after antidote addition 160

Figure 3-26: DNA hybridization on the NRs surface 163

Figure 3-27: FRET curve at 25^{o}C and 80^{o}C 164

Figure 3-28: DNA hybridization on high coverage NCs 166

Figure 3-29: DNA hybridization on high coverage NRs 166

Figure 3-30: DNA hybridization on TBA NRs 167

Figure 3-31: DNA hybridization on mid-Coverage NRs 167

Figure 3-32: DNA hybridization on Low-coverage NRs 168

Figure 3-33: Sigmoidal fit for the DNA hybridization (r^2=0.998) 169

Figure 4-1. Absorbance spectra of NRs (red) and NBs (blue). 184

Figure 4-2. Scheme of the selective release of thiolated ssDNA 185

Figure 4-3. CTAB-NRs and CTAB-NBs 186

Figure 4-4. Melting CTAB-NRs at 800nm 187

Figure 4-5. Melting CTAB-NBs at 1100nm 188

Figure 4-6. Minimal melting of the CTAB-NRs at 1100nm 189

Figure 4-7. No melting of the CTAB-NBs at 800nm 189

Figure 4-8. Selective melting of CTAB-NR-NB at 800nm 191

Figure 4-9. Selective melting of CTAB-NR-NB at 1100nm 192

Figure 4-10. Loading of thiolated TBA with and without PolyT spacer 194

Figure 4-11. Effect of TBA in blood and effect of antidote on TBA 195

Figure 4-12. ABS spectra of 5nM TBA-NRs at increasing irradiation times 196

Figure 4-13. TBA release as a function of irradiation time 197

Figure 4-14. ABS spectra of TBA-NRs irradiated for 30 min 198

Figure 4-15. TBA release as a function of irradiation time 198

Figure 4-16. Functionality of the released TBA 199

Figure 4-17. Effect of thiolated TBA-NRs in blood 200

Figure 4-18. Scheme of CW irradiation.....201

Figure 4-19. Absorbance of CW irradiated NRs 202

Figure 4-20. Released TBA and thiolated T_{15}-antidote after 800nm CW laser irradiation 203

Figure 5-1. Scheme of combined and sequential assembly 211

Figure 5-2. Absorbance spectra of the protein coronas 213

Figure 5-3. TEM images of NR, NB, CNT and CoNR, CoNB, CoCNT 214

Figure 5-4. DLS measurements (top) and Zeta potentials (bottom) of NR, NB, CNT and CoNR, CoNB, CoCNT.....215

Figure 5-5. Variation of the corona components.....217

Figure 5-6. Absorbance of NR-coronas.....217

Figure 5-7. Absorbance of SeNR.....219

Figure 5-8. Loading from coronas as measured by supernatant loss 220

Figure 5-9. Loading of NR-coronas measured by heat displacement.....221

Figure 5-10. DLS of coronas formed with HS, ES and HSA 222

Figure 5-11. Loading of CoNRs, as a function of [PB].....224

Figure 5-12. Stability of NR-coronas in different buffer strengths and buffers. 224

Figure 5-13. Loading of the NRs as a function of CTAB concentrations.....226

Figure 5-14. Loading of the NRs as a function of HS concentrations 227

Figure 5-15. Loading of the NRs, NBs and CNTs.....228

Figure 5-16. Formation of the protein coronas.....229

Figure 5-17. Leakage from NP-coronas, by tuning corona formation.....232

Figure 5-18. Changing the PB after formation of coronas 233

Figure 5-19. Formation of the protein coronas.....236

Figure 6-1. Scheme of the selective release approach 245

Figure 6-2. Calibration of TBA (top) and antidote:TBA, with [TBA]=500nM(bottom) 248

Figure 6-3. Absorbance spectra of NR, NB, NR-HS-TBA and NB-HS-anti.....250

Figure 6-4. Loading of NR-HS-TBA and NB-HS-anti.....251

Figure 6-5. DLS and Zeta potential of NB-CTAB, NB-HS-anti, NRs-CTAB and NR-HS-anti.....252

Figure 6-6. 1100nm irradiation of NB-HS-anti. Melting and release (inset).....253

Figure 6-7. 800nm irradiation of NR-HS-TBA. Melting and release (inset).....254

Figure 6-8. Comparison of HS-TBA-Bock release, thiolated TBA-NRs and calibrations 255

Figure 6-9. Comparison of HS-TBA-Bock release and thiolated TBA-NRs 256

Figure 6-10. Comparison of HS-TBA-Bock release and thiolated TBA-NRs 257

Figure 6-11. Comparison of HS-TBA-Bock release and thiolated TBA-NRs 258

Figure 6-12. Comparison of HS-TBA-Bock release and thiolated TBA-NRs 259

Figure 6-13. 1100nm irradiation of the NR-HS-TBA and NB-HS-antidote. Left: Absorbance. Right: fluorescence of the released species 260

Figure 6-14. Measurement of the effect of particles in blood. 261

List of tables

Table 1-1: Specificities of aptamers to heparin-binding molecules[73] 50

Table 1-2: Kinetic parameters of some aptamers[73] 50

Table 2-1: Parameters for the synthesis of NS of different sizes 72

Table 3-1: Kinetic binding constants for different surface chemistries 143

Table 3-2: Assembly kinetic constants of different surface chemistries 146

Table 3-3: Kinetic binding constants for High Coverage NR-T_{15}-TBA 148

Table 3-4: Calculated kinetic binding constants for high coverage T_{15}-TBA 149

Table 3-5: Kinetic binding constants for Low coverage NR-T_{15}-TBA.....150

Table 3-6: Calculated binding constants for T_{15}-TBA with Low coverage.....151

Table 3-7: Kinetic binding constants for PEG backfilled NR-T_{15}-TBA 151

Table 3-8: Calculated kinetic binding constants for PEG-backfilled NR-T_{15}-TBA 152

Table 3-9: Compared values of DNA hybridization on different surfaces 168

1. Introduction: On the control of blood clotting

1.1. Motivation

The coagulation of blood is necessary to avoid bleeding and is achieved by the blood clotting cascade, which is an enzymatic cascade that ensures a rapid and localized response to injury. However, there are a number of thrombophylic disorders, such as deep venous thrombosis (DVT), stokes, heart attacks, peripheral vascular diseases, and many others where precise control of blood clotting by the use of anticoagulants is required. The most widespread anticoagulants are (1) heparin –which acts rapidly by its presence in the blood-, (2) warfarin –which is acts after some delay- and (3) aspirin.

The discovery of heparin by McLean and Howell on 1916[1, 2] is one of the most important advances in medicine. Heparin is a mucopolysaccharide that is extracted from bovine and porcine gut mucosa[3]. Even nowadays, injectable heparin is the most commonly used anticoagulant due to its rapid effectiveness, availability and low cost. It prevents blood coagulation by inhibiting thromboplastin –by depressing factors V, IX, XI and XII- and by enhancing fibrinolysis –and inhibiting the polymerization of fibrinogen- [4].

Warfarin was discovered in the 1920s, when cattle in northern US and Canada started dying of internal bleeding, due to sweet clover disease. Later, in 1948, warfarin was used as rat poison, with rodents dying of internal haemorrhage. In 1950s, warfarin started being used as an anticoagulant, with the name 'Coumadin', and is currently the most widespread oral anticoagulant[2]. However, its effect in preventing blood clotting is not immediate, and it requires a controlled dosage and the use of heparin before it can be administered. Warfarin prevents blood clotting by lowering the amount of active vitamin K available for the activation of clotting factors II, VII, IX and X[5].

Aspirin was discovered by Hoffmann in 1898, and was initially used as an antipyretic and anti-inflammatory drug. Aspirin also has antithrombotic effects, and it prevents the coagulation of blood by preventing platelet aggregation, increasing blood clot lysis, and lowering the formation of thrombin by decreasing tissue factor expression[6].

All these anticoagulants have side effects, the most common of them being a high risk of bleeding, if dosage is not correctly monitored[1, 5]. Moreover, anticoagulants are administered to the entire bloodstream, and most of them do not have a specific antidote, so their effect can only be reduced by clearance. Therefore, when surgery is required, it needs to be postponed for several days, until the anticoagulants are cleared from the body, during which time blood clots could be produced and transported in the

bloodstream, with the possibility of eventually causing strokes-. Moreover, in the early 2000's several deaths were caused by contaminated batches of heparin that were distributed in the US [7-10]. Other adverse reactions of anticoagulants include thrombocytopenia, acute heparin reaction, heparin associated osteoporosis, heparin and warfarin-related skin reactions, abnormal liver functioning, and eosinophilia, among others [4, 11].

Therefore the possibility of manipulating blood clotting in a way that is *specific* –by using an anticoagulant that can inhibit only one protein in the blood clotting cascade-, *reversible* –by using an antidote that can stop the activity of the anticoagulant-, *localized* –by enabling the control of blood clotting in a confined area- and *externally controlled,* would represent a great improvement over the current practice of administering anticoagulants over the whole bloodstream and relying in physiological clearance to restore the system's activity.

1.2. Objectives and strategies

With the use of gold nanoparticles, it is possible to achieve a localized and external release of biomolecules. The conjugation of gold nanoparticles with biomolecules has enabled important advances in diagnostic and therapeutic nanomedicine. The biocompatibility and unique optical properties of gold nanoparticles has enabled their use in sensing, imaging, drug release and assembly applications.

The interaction of light with noble metal nanoparticles results in collective oscillations of the electrons in the metal known as surface plasmon resonance (SPR). The SPR is dependent on the size and shape of the particles, and can be tuned throughout the visible and IR regions. Gold nanoparticles have a SPR peak, and therefore can be melted by ultrafast laser irradiation at the SPR to release a drug or biomolecule on their surface. Thus, gold nanoparticles of different sizes and shapes have been used for photothermal therapy and delivery.

We have developed a method to **externally control blood clotting by exploiting the optical properties of gold nanoparticles**. Nanoparticles are attractive for interfacing to biological systems and have been used to manipulate biological processes and reactions in a way that is specific, reversible and spatially localized. Here we use gold nanoparticles conjugated with a biomolecule (ssDNA aptamer, TBA) that can specifically

inhibit human thrombin, and an antidote (ssDNA complementary sequence) that restores its activity. We use gold nanorods (NRs), as they can be synthesized to absorb light in the infrared region, where biological tissue has minimal absorption. The SPR is tunable by changing the NR aspect ratio (AR); therefore, NRs with different ARs can be independently excited at different wavelengths to release different payloads[12]. By using this approach, we use laser excitation at one wavelength to release the aptamer and trigger the inhibition of thrombin, and then use a different wavelength to deliver the antidote and specifically reverse the effects of the aptamer (Fig. 1-1). Thus, the pair of NRs acts an on/off switch for blood clotting.

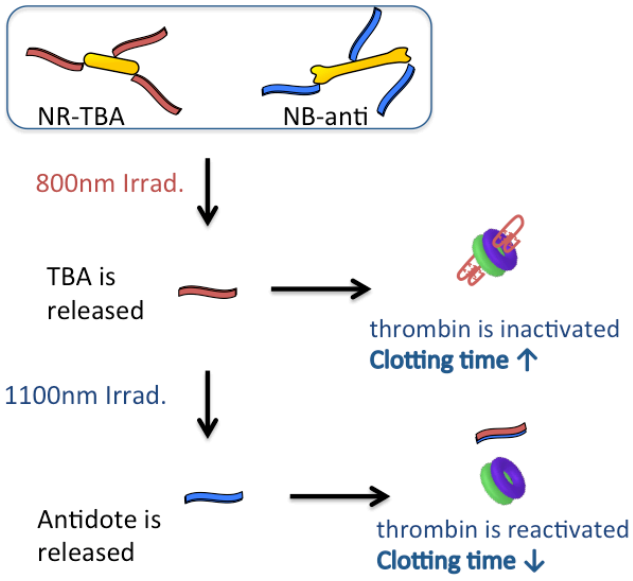

Figure 1-1: Scheme

We study the binding of the TBA by thiol chemistry and by taking advantage of protein coronas that naturally form around nanoparticles in biological fluids for enhanced loading[13]. We also quantify the interactions of thrombin with gold nanoparticles at the interface, the formation of protein coronas, and the passive release of ssDNA from protein coronas weakly bound to nanoparticles.

1.3. Background

1.3.1. Gold nanoparticles

It was in the Middle Ages when artisans started using gold nanoparticles to give color to stained glasses in the cathedrals. This fact was not recognized until 1857, in M. Faraday's Bakerian Lecture on the "Experimental Relations of Gold (and other Metals) to Light" [14], when he observed that the red color of colloidal gold comes from the presence of aggregates of gold atoms. Nevertheless, it was not until the twentieth century when colloidal chemistry received a huge growth due to the works of Oswald, Mie [15], Svedberg and Zsigmondy[16].

One fact that was already noticed more than a 100 years ago is how the amount of surface atoms increases with decreasing the particle size. If we imagine a cube of 1cm edge, the percentage of surface atoms would be around 10^{-5}%. Moreover, in a cube of 10nm edge, this percentage would increase to 10%; and in a cube of 1nm edge, each atom would be a surface atom [17]. This is one of the reasons why one can expect very different physical and chemical properties in a nanoparticle than those expected in bulk materials.

Nanotechnology comprises all the methods and techniques to study, design and fabricate devices that work in the nanometer scale (1-100nm). Its interest has increased in the last decade, where more than 35 countries have developed programs in nanotechnology since 2000[18], and the number of published articles regarding nanotechnology has rapidly increased during the last years (Fig. 1-2). The interest on nanotechnology is based on the fact that all biological systems have their first level of organization at the nanoscale [19]; therefore, nanotechnology can lead to important improvements in biology, biotechnology, medicine and healthcare.

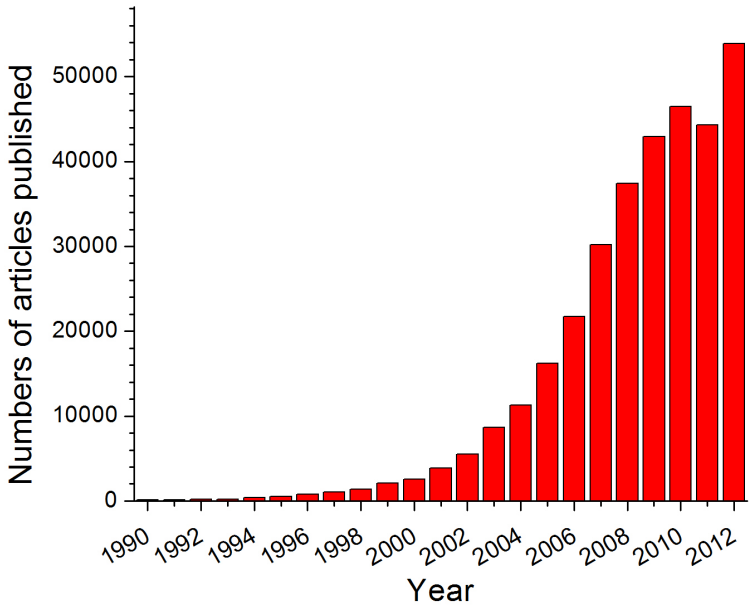

Figure 1-2: Published articles on nanotechnology since 1990. Searched "nanoparticle" in google scholar

The nanoscale interactions of organic and inorganic matter lead to the construction of cells and more complex organisms –the brain and the human body-. Therefore, nanotechnology plays a key role in understanding these processes and in the progress of biological sciences and biotechnology. A significant amount of research has been devoted to studying the interactions of many types of nanoparticles, including quantum dots [20], polymeric nanoparticles[21], carbon nanotubes[22] or gold nanoparticles[23-28], with biological systems.

Gold nanoparticles are especially interesting for interacting with biological systems due to their surface chemistry and optical properties. They can be synthesized with different sizes and shapes, such as spherical[23], stars[29], shells[30-32], bones[33] or rods[34, 35] –among others-, resulting in diverse physical and chemical properties.

Gold nanorods (NRs) are particularly attractive due to the fact that tuning their size tunes their optical properties. They can be synthesized to absorb light in the infrared region, where biological tissue does not absorb. Moreover, their surface properties make them amenable for biological applications.

1.3.1.1. Surface chemistry

The surface chemistry of gold nanoparticles varies depending on their size and shape. Moreover, as the size of the nanoparticles increases they need to be stabilized by ligand

in order to be stable in solution, particularly in the case of gold nanorods. This coating on the particles plays a key role in the nanoscale interactions of the nanoparticles with biological materials.

Usually, gold nanoparticles are synthesized in a surfactant solution that keeps them stable [35, 36]. Thiol-gold chemistry has been widely used when working with gold nanoparticles[37-39]. After the synthesis of the nanoparticles, it will usually be necessary to perform a ligand exchange[38, 40] for biofunctionalization and to lower the cytotoxicity, of the synthesizing surfactant in the case of NRs. After the ligand exchange, a DNA conjugation, PEG backfill[41] or other modification to the particles' surface can be achieved. Therefore, the ligand on the particle surface is the most important parameter when studying its interactions with biological molecules.

Other approaches for nanoparticle functionalization include the use of protein coronas. Its greatest advantage is that it enables for an enhanced loading[13] on the particles, and a potential reduction on biocompatibility, as the proteins that mask the particle surface are already present in blood.

An important parameter to study when working with gold nanoparticles is their toxicity, which not only depends on the ligand on the particle's surface, but also on their size and shape. In the case of gold nanoparticles, several studies of their toxicity have been

conducted [42-44]. These studies show that the toxicity of nanoparticles both *in vivo* and *in vitro* is low.

1.3.1.2. Optical properties

The optical properties of a material are due to the motion its surface electrons can execute. The electrons in metals are highly delocalized, therefore, when we reduce the size of a metal until it is comparable to the electron mean free path, one can observe an intense absorption in the visible-near-UV, which results from coherent oscillation of the free electrons from one surface of the particle to the other and is called surface plasmon resonance (SPR). Such strong absorption induces strong coupling of the nanoparticles to the electromagnetic radiation of light.

In figure 1-3, we can observe a scheme illustrating the excitation of the dipole surface plasmon oscillation. The electric field of an incoming light wave induces polarization of the free conduction electrons in respect to the core of the spherical gold nanoparticle. There is a net charge difference at the nanoparticle's boundaries. In this way, the SPR is the dipolar oscillation of the electrons with period T. This condition can be observed in absorption and scattering spectroscopy and depends on the shape, size and dielectric constants of the metal and the surrounding material. The SPR is the physical characteristic most responsible for the optical properties of gold nanoparticles[45]. Mie

was the first to solve Maxwell's equations of an electromagnetic field interacting with a spherical gold particle under the appropriate boundary conditions.

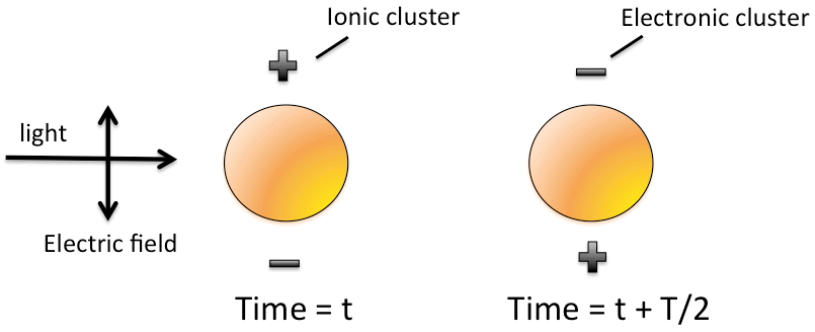

Figure 1-3: Surface Plasmon Absorption of Spherical Nanoparticles[17]

In the case of gold nanorods, their unique optical properties rely on their lack of symmetry. The aspect ratio (length divided by width) of gold nanorods can be tuned by the synthesis conditions, and it determines the wavelength of the Surface Plasmon Resonance. Therefore, gold nanorods with different aspect ratios will have different SPRs. Gans extended Mie's theory to account for ellipsoids –which are similar to the shape of gold nanorods[46]-. The extinction coefficient of randomly oriented NRs (ε_{NR}) according to Gans is:

$$\varepsilon_{NR} = \frac{2\pi[NR]V_{NR}\varepsilon_m^{3/2}}{3\lambda}\sum_i \frac{\frac{\varepsilon_2}{P_i^2}}{\left[\varepsilon_1 + \left(\frac{1-P_i}{P_i}\right)\varepsilon_m\right] + \varepsilon_2^2}$$

Where ε_m is the relative dielectric constant of the medium immediately surrounding the particle, ε_i is the wavelength-dependent relative complex dielectric constant of gold (Imaginary: ε_2; Real: ε_1). The wavelength of the interacting light is symbolized by λ, V_{NR} is the volume of one nanorod and P_i is the depolarization factors for the three axes A,B and C for the rod, where A > B =C. They are dependent on the aspect ratio (AR) of the NR, following the equation:

$$P_A = \frac{1-e^2}{e^2}\left[\frac{1}{2e} ln\left(\frac{1+e}{1-e}\right) - 1\right]$$

$$P_B = P_C = \frac{1-P_A}{2}$$

Where e is a function of the AR of the NR:

$$e = \sqrt{1-\frac{1}{AR^2}}$$

The previous equations predict that as the AR of the particles approaches to 1 (spherical particles), there is a peak in the extinction coefficient at around 530nm. As the AR increases, this peak splits in two. The redder peak is due to the plasmon resonance of the longitudinal direction of the NR; while the bluer peak is due to the plasmon resonance of the transverse direction of the NR. The extinction coefficient increases as the AR increases.

Nanoparticle assembly

The assembly of gold nanoparticles to form larger structures leads to a change in their optical properties [47-49], which can be observed as a shift in their SPR peaks. El-Sayed group[50] simulated the changes in the absorption spectra of gold NR after their attachment to form dimers and trimers. They observed that if the NRs attach side by side, their SPR longitudinal absorption peak shifts to the blue region of the spectra, and if the NR attach head to tail, their spectra shifts to the red region of the spectra, resulting from plasmon coupling of neighboring particles interacting in the assembly. Authors agree that the optical properties of gold nanoparticle assemblies depend mainly on the size of the aggregate[49], and that they cannot be explained using small aggregate models[47].

In the last years, the use of nanoparticles as building blocks to form functional devices has gained increasing attention for a number of applications, such as sensing, *in vivo* targeting and imaging, of single molecule detection by surface enhanced Raman spectroscopy [51, 52]. NRs are especially interesting as they absorb light both in the infrared and in the visible regions. Some authors have reported the design and formation of NR assemblies of controlled size and shape[53-57] in one, two and three dimensions. Also, biorecognition systems[58] such as antibody-antigen pairs (biotin-streptavidin)[59],

DNA hybridization[48, 53], or aptamer-protein[55, 60] recognition has gained much attention in the last years.

Photothermal heating of gold nanorods

Photothermal heating is the phenomenon based on the conversion of the optical energy that certain materials selectively absorb to heat. Gold nanorods can be used as strong absorbers due to their high absorption coefficient in the SPR peak. Moreover, the fact that their absorption peak can be tuned –and therefore the wavelength of the incoming light- by the synthesis conditions, makes them attractive for photothermal therapy[30].

By using photothermal therapy, it is possible selectively kill targeted cells, or enable externally controlled drug delivery. In order to do so, the absorption peak of the gold nanorods has to be inside the "tissue window", between 600 and 1300nm, where the penetration of light in tissue is maximal. This ensures that the gold nanorods with SPRs inside the tissue window will absorb light preferentially.

Photothermal heating can be accomplished by a variety of sources, such as continuous wave (CW) laser, nanosecond-pulsed laser or femtosecond-pulsed lasers[62]. The local temperature of the NRs will be higher as the laser pulse width decreases, taking into account the same energy per pulse.

During the femtosecond laser irradiation of the gold nanorods at their SPR there is a collective motion of the electrons in the metal nanoparticle that resonantly couples with the oscillating electric field of the incident light. The energy of the photons absorbed is converted to heat via a multi-step process. First, (1) the photons excite the electron cloud during the pulse duration. (2) The electrons transfer the energy to phonons in the lattice; the particle's temperature increases as a result of the electron-phonon scattering. (3)This heat is dissipated to the surrounding media though phonon-phonon interactions. The dissipation of heat is dependent on the nanoparticle size, ligand and surrounding media.[63]

Photon-Electron

Once the gold nanoparticle is irradiated with light at their SPR, the energy from the photons is transferred to the electron cloud. Exciting the coherent motion of the free electrons by use of femtosecond laser pulses leads to a rapid dephasing of the electronic coherent oscillation due to strong electron-electron repulsion. This leads to the formation of a pulse of hot electrons of tens of thousands of degrees (approaching 1000K) on the femtosecond time scale (~4fs).

Electron-phonon

When the electron cloud is raised to a high temperature, there is an imbalance in the energy level of the electrons and the crystal lattice. This imbalance is relaxed by collisions of the hot electrons with the lattice ions; it results in heating the gold nanocrystal lattice homogenously via electron-phonon interactions, which happens in the picosecond time-scale (≈1.5-4ps)[64, 65]. The energy transfer to the lattice induces vibrations of the lattice ions from their mean position that leads to thermal expansion of the nanoparticle.

Phonon-phonon

As the lattice starts to vibrate, there is an imbalance between the phonons in the nanoparticle lattice and the surrounding fluid. This energy imbalance is relaxed through phonon-phonon interactions, and conduction will be the dominant mode of heat transfer. Therefore, classical diffusion equations characterize nanoparticle cooling. The energy transfer in phonon-phonon interactions happens in the picoseconds time scale (≈100ps)[62, 64].

Ultrafast photothermal heating of the gold nanorods at their SPR induces the melting of the particles. For NRs, this results in a shape transformation to spheres. The timescale of the melting process of gold nanorods has been measured by El-Sayed group to be ~35ps

[66]. Also, the energy needed to melt gold nanorods with fs laser pulses is around $0.01 J/cm^2$ [62, 67]. Moreover, the photothermal heating and melting of the gold nanorods cause the dissociation of the thiol-gold bonds on the surface of the gold nanorods[68].

Selective photothermal heating of gold nanorods with different SPR

Previous work from Hamad-Schifferli group shows that it is possible to selectively release different ssDNA sequences from NRs with different AR (Fig 1-4)[69]. Such experiments were performed by mixing DNA conjugated NRs with SPR maximum at 800nm wavelength and DNA-conjugated gold nanobones (NBs) with SPR maximum at 1100nm, and irradiating them at 1100nm and 800nm with fs lasers at different fluences.

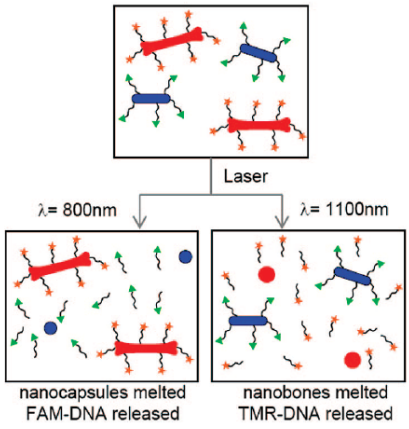

Figure 1-4: Overview of the selective release[69]. Reprinted with permission from Wijaya A, Schaffer SB, Pallares IG, Hamad-Schifferli K. Selective Release of Multiple DNA Oligonucleotides from Gold Nanorods. ACS Nano 2008;3:80. Copyright 2008 American Chemical Society.

The results showed that when the mixture was irradiated at 1100nm, only the ssDNA attached on the NBs was released; and when the mixture was irradiated at 800nm, only the DNA attached on the NRs was released.

They could observe the decrease in the SPR of the nanoparticles as they were irradiated with different fluences (Fig 1-5). In the top image, the particles were irradiated with a 800nm fs laser, and one can observe, both in the absorbance spectrum and in the TEM image, that only the NRs melted. On the bottom image, the mixture was irradiated at 1100nm wavelength, with a femtosecond pulsed (fs) laser. It can be observed both in the TEM image and in the absorbance spectrum that only the NBs melted.

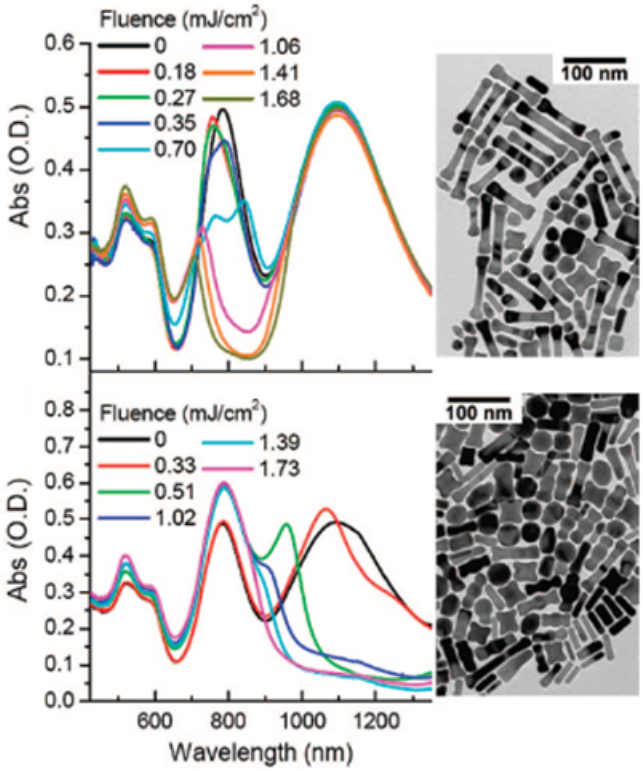

Figure 1-5: Absorbance and TEM image of the NRs and NB after irradiation[69]. Reprinted with permission from Wijaya A, Schaffer SB, Pallares IG, Hamad-Schifferli K. Selective Release of Multiple DNA Oligonucleotides from Gold Nanorods. ACS Nano 2008;3:80. Copyright 2008 American Chemical Society.

Selective DNA release from the gold nanoparticles was also demonstrated (Fig. 1-6). In the image on the left, the mixture was irradiated at 800nm, releasing the DNA attached to the NRs and not the DNA attached on the NB. Moreover, this DNA was still functional as shown in the melting curve of the DNA (Image 10, left on the top). In the

image on the right, one can see the results after the laser irradiation of the mixture at 1100nm.

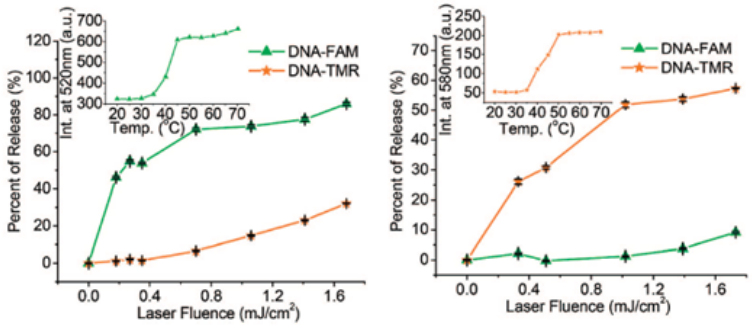

Figure 1-6: Fluorecense of the DNA released after the irradiation[69] Reprinted with permission from Wijaya A, Schaffer SB, Pallares IG, Hamad-Schifferli K. Selective Release of Multiple DNA Oligonucleotides from Gold Nanorods. ACS Nano 2008;3:80. Copyright 2008 American Chemical Society.

In this thesis we will use this approach and selectively release ssDNA aptamers and antidotes from NRs and NBs, by irradiating them at different wavelengths.

1.3.2. Thrombin and the coagulation cascade

The blood clotting cascade is an enzymatic cascade. Enzymatic cascades are efficient at reaching a rapid response, and can often do so with both temporal and spatial precision. In a cascade, an initial signal starts a series of steps, each of them catalyzed by an enzyme. The signal is amplified at each step[70]. Therefore, small amounts of the initial factors are enough to start the cascade, and ensure a rapid response to trauma.

Blood clotting is initialized by the intrinsic and the extrinsic pathways (Fig 1-7). The intrinsic pathway starts with the activation of factor XII by contact with abnormal surfaces produced after an injury. The extrinsic pathway is started by trauma, which activates factor VII and releases tissue factor from blood vessels. The extrinsic and intrinsic pathways meet on the common final step where the conversion of fibrinogen into fibrin by thrombin, leads to the formation of a blood clot. The two pathways interact with each other and both are needed for proper clotting. For instance, in patients suffering from Hemophilia A, the factor VIII has a severe loss of activity or is missing. Factor VIII stimulates the formation of factor Xa, by factor IXa. Therefore, the activation of the intrinsic pathway is severely damaged in hemophilia.

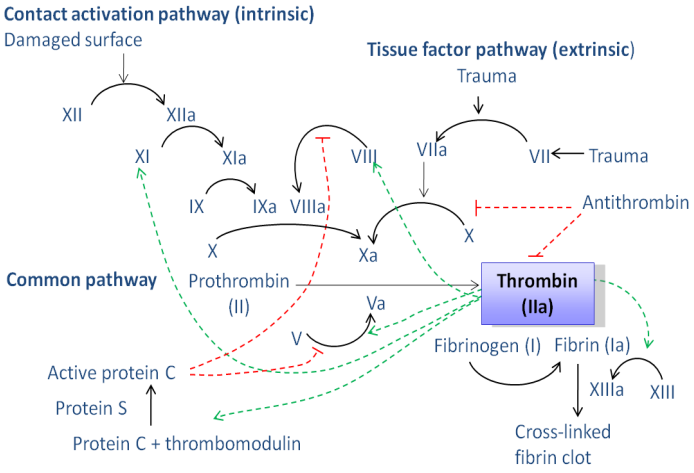

Figure 1-7: Coagulation cascade

Vitamin K is also essential for the synthesis of prothrombin and other clotting factors. Therefore, vitamin K antagonists such as dicoumarol or warfarin are used as anticoagulants in patients prone to clot formation.

The termination of clotting is achieved due to the short life that activated factors have, as they are diluted by blood flow, and degraded by proteases. For example, the factors V_a and $VIII_a$ are degraded by protein C, a protease that is switched on by the action of thrombin. Thus, thrombin has a dual function: it catalyzes the formation of fibrin and it initiates the deactivation of the clotting cascade.

Moreover, there are specific inhibitors of clotting factors that are important in the clotting termination. The most important one is antithrombin III, a plasma protein that inactivates thrombin. Antithrombin III also blocks other serine proteases in the clotting cascade: factors XII_a, XI_a, IX_a, and X_a. The inhibitory action of antithrombin III is enhanced by heparin, which acts as an anticoagulant by increasing the rate of formation of irreversible complexes between antithrombin III and the serine protease clotting factors.

Therefore, in some surgical procedures, such as heart surgery, it is extremely important to control the blood clotting cascade. Moreover, thrombosis is a serious cause of illness and death. The drugs typically given to patients suffering these illnesses are heparin and

warfarin. These drugs are anticoagulants and prevent the formation of blood clots; therefore, it is extremely important to control the doses, as an overdose could lead to bleeding. Warfarin takes a few days to affect the coagulation cascade, has different reactions in different patients and it is very difficult to dose[71]. In the case of heparin, some patients develop antibodies against it, and there have been cases of adulterated heparin that have causes the death of many people[10]. Common factors of both drugs are that their activity is stopped by clearance of the drug and therefore cannot be effectively controlled. Furthermore, they have an effect in the whole bloodstream and they do not affect specifically one protein in the coagulation cascade.

As thrombin is a key regulatory enzyme in the coagulation cascade[72], a drug that could directly control its activity would be an important step while solving the aforementioned issues. Thrombin is a seriene protease, produced from prothrombin by the action of factor Xa, and converts fibrinogen to fibrin, which is the building block of the fibrin matrix of blood clots. Among other effects, it activates platelets by initiating a change in their shape.

1.3.2.1. Thrombin binding aptamer

Aptamers are sequences of RNA or DNA that serve as powerful binders to small molecules for many applications -they can interact with proteins, polypeptides, viruses or

even cells-. Nowadays, they can be generated against most target proteins with binding affinities as high as Kd ~ nM, and in most cases they are also able to inhibit the activity of the target protein.

Aptamers are isolated by systematic evolution of ligands by exponential enrichment (SELEX). Initially, a DNA library containing random sequences is –in the case of RNA, transcribed to an RNA pool, and- applied to selection procedures, such as affinity chromatography. The ligand against which the selection is being performed is attached covalently to the column resin. DNA or RNA molecules that do not bind to the ligand are washed off the column, and those that are specifically binding are eluted with the ligand. These sequences are reverse-transcribed -in the case of RNA- and amplified using polymerase chain reaction (PCR) resulting in a selected DNA pool which is submitted to consecutive rounds of selection[73].

Aptamers bind their targets with affinities comparable to those observed for antibodies, with K_d values that range from the low picomolar to the mid-nanomolar range[73]. For instance, thrombin binding aptamer (TBA) binds to thrombin with a K_d of 0.5nmol/l[74]; the aptamer to P-selectin can bind its target with an affinity of 29pmol/l[75] and the aptamer developed to target amyloid beta 4 has an affinity of 29nmol/l[76].

Generally, aptamers are specific binders. In fact, aptamers to heparin binding members of the coagulation cascade are very specific for their targets versus the other members of the coagulation cascade, as illustrated in table 1-1[73]:

Aptamer	**VEGF K_d (nmol/l)**	**bFGF K_d (nmol/l)**	**KGF K_d (nmol/l)**	**PDGF-AB K_d (nmol/l)**	**Thrombin K_d (nmol/l)**
VEGF (NX-213)	0.14	286	NA	91	3060
bFGF (m21a)	426	0.35	450	140	>10μmol/l
KGF (14F3'T)	NA	10	0.0008	50	>10μmol/l

Table 1-1: Specificities of aptamers to heparin-binding molecules[73]

The kinetics of a few aptamer-target pairs have also been studied, usually by calculating the k_{off} by forming the complexes with radiolabeled aptamers, and monitoring the decay of aptamer-protein complexes after the addition of an excess of unlabeled aptamers. k_{on} can be calculated using the approximation $k_{on}=k_{off}/K_d$:

Aptamer	**Target**	**k_{off} (s^{-1})**	**k_{on} (l/mol.s)**	**K_d (nmol/l)**	**$t_{\frac{1}{2}}$ (min)**	**T (ºC)**
NX-213	NEGF	$1.4x10^{-3}$	$1.0x10^{7}$	0.14	8.2	37
m21a	bFGF	$1.96x10^{-3}$	$5.6x10^{6}$	0.35	5.9	37

Table 1-2:Kinetic parameters of some aptamers[73]

One of the first therapeutic aptamers isolated by SELEX was against human thrombin [74, 77, 78]. The 15mer TBA DNA aptamer (TBA): 5' GGTTGGTGTGGTTGG 3', prolongs clotting time from 25s to 169s in purified fibrinogen, and from 25s to 43s in human plasma. Moreover, it inhibits platelet aggregation and prolongs thrombin-induced platelet activation [79, 80]. This DNA aptamer has a G-quadruplex secondary structure while binding to thrombin [81, 82], which is stabilized by K^+, and other ions in solution [83-87]; and can be even induced in the presence of thrombin[88]. TBA can bind to thrombin at either exosite I or II. As a consequence, two TBAs can bind to one thrombin [55, 81, 89]. As mentioned earlier, thrombin-TBA interaction is highly specific, with a K_d in the picomolar range. Other aptamers that bind and inhibit human thrombin have been discovered[77], however, in this work we will focus on the TBA-thrombin binding.

Thrombin-TBA interaction is reversible. Because TBA needs to be in a G-quadruplex structure in order to bind to thrombin, it is possible to unbind it by unfolding the G-quadruplex structure of TBA. Some authors have reported the use of poryphrins[90]. But the complementary DNA sequence of the aptamer may be used as well to dissociate the TBA-thrombin complexes. Therefore, it is possible to picture a biomachine that can cycle through states of binding and unbinding from thrombin after the addition of ssDNA[91]. On a first stage, TBA would fold in its G-quadruplex structure and bind to thrombin,

and after the addition of the ssDNA complement, TBA would bind to its complement and release thrombin.

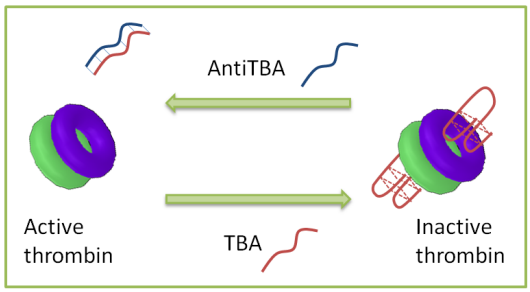

Figure 1-8: TBA-thrombin cycle

One can interface such a biomachine to a surface, for example gold nanorods (NRs), by conjugating the surface of the NRs with TBA via a thiol bond. In this case, because TBA can bind to both exosite I and II of thrombin, the binding of thrombin to TBA-NRs results in NRs self-assembly, that can be monitored by optical absorption. Once the complementary ssDNA sequence to TBA is added, the assembly process is reversed. This procedure is useful for obtaining the binding energies of the TBA with thrombin, when the TBA is bound to gold nanoparticles, and will provide insight on the binding energies that are involved in the process.

1.4. Thesis outline

In this thesis we will first explain the Methods used in all of the following projects. Then, we will introduce the first approach we used for the biomolecular control of blood clotting. This involved binding the TBA covalently to gold nanoparticles and testing the release of TBA and its effects on blood clotting. We performed characterization on the interactions of thrombin and antidote with covalently bound TBA on the NPs (Chapter 3). Chapter 4 focuses on the release of the covalently bound TBA from gold nanoparticles. In Chapter 4, we also observe the limitations that binding TBA covalently to the NPs have, such as the loss of activity of the released TBA, and the low binding of TBA to the NPs. In order to increase the loading on the particles and the activity of the released drug, we will test the use of protein coronas (Chapter 5), that enables increased loading on the NPs, and therefore, higher released concentrations of the aptamer. We will characterize the protein coronas, study their formation and the leakage rates that arise from their non-covalent binding nature. In Chapter 6, we will test the selective release idea with protein coronas and observe that blood clotting time can be selectively and externally controlled by taking advantage of the capacities of protein coronas.

1.5. Bibliography

[1] Ehrlich J, Stivala SS. Chemistry and pharmacology of heparin. Journal of Pharmaceutical Sciences 1973;62:517.

[2] Wardrop D, Keeling D. The story of the discovery of heparin and warfarin. British Journal of Haematology 2008;141:757.

[3] Kearon C, Kahn SR, Agnelli G, Goldhaber S, Raskob GE, Comerota AJ. Antithrombotic therapy for venous thromboembolic disease. Chest 2008;133:454S.

[4] Bick RL, Frenkel EP. Clinical aspects of heparin-induced thrombocytopenia and thrombosis and other side effects of heparin therapy. Clinical and Applied Thrombosis-Hemostasis 1999;5:S7.

[5] Holbrook AM, Pereira JA, Labiris R, McDonald H, Douketis JD, Crowther M, Wells PS. Systematic overview of warfarin and its drug and food interactions. Archives of Internal Medicine 2005;165:1095.

[6] Undas A, Brummel-Ziedins KE, Mann KG. Antithrombotic properties of aspirin and resistance to aspirin: beyond strictly antiplatelet actions. Blood 2007;109:2285.

[7] Blossom DB, Kallen AJ, Patel PR, Elward A, Robinson L, Gao G, Langer R, Perkins KM, Jaeger JL, Kurkjian KM, Jones M, Schillie SF, Shehab N, Ketterer D, Venkataraman G, Kishimoto TK, Shriver Z, McMahon AW, Austen KF, Kozlowski S, Srinivasan A, Turabelidze G, Gould CV, Arduino MJ, Sasisekharan R. Outbreak of Adverse Reactions Associated with Contaminated Heparin. New England Journal of Medicine 2008;359.

[8] Guerrini M, Beccati D, Shriver Z, Naggi A, Viswanathan K, Bisio A, Capila I, Lansing JC, Guglieri S, Fraser B, Al-Hakim A, Gunay NS, Zhang Z, Robinson L, Buhse L, Nasr M, Woodcock J, Langer R, Venkataraman G, Linhardt RJ, Casu B, Torri G, Sasisekharan R. Oversulfated chondroitin sulfate is a contaminant in heparin associated with adverse clinical events. Nature Biotechnology 2008;26.

[9] Kishimoto TK, Viswanathan K, Ganguly T, Elankumaran S, Smith S, Pelzer K, Lansing JC, Sriranganathan N, Zhao G, Galcheva-Gargova Z, Al-Hakim A, Bailey GS, Fraser B, Roy S, Rogers-Cotrone T, Buhse L, Whary M, Fox J, Nasr M, Dal Pan GJ, Shriver Z, Langer RS, Venkataraman G, Austen KF, Woodcock J, Sasisekharan R. Contaminated heparin associated with adverse clinical events and activation of the contact system. New England Journal of Medicine 2008;358.

[10] Kemsley J. Heparin Undone - A consortium of scientists raced against the clock to identify the cause of adverse reactions. vol. 86: Chemical & Engineering News, 2008. p.38.

[11] Essex DW, Wynn SS, Jin DK. Late-onset warfarin-induced skin necrosis: Case report and review of the literature. American Journal of Hematology 1998;57:233.

[12] Wijaya A, Schaffer SB, Pallares IG, Hamad-Schifferli K. Selective Release of Multiple DNA Oligonucleotides from Gold Nanorods. ACS Nano 2008;3:80.

[13] Kah JCY, Chen J, Zubieta A, Hamad-Schifferli K. Exploiting the protein corona around gold nanorods for loading and triggered release. ACS Nano 2012:Just Accepted.

[14] Faraday M. The Bakerian Lecture: Experimental Relations of Gold (and other Metals) to Light. Phil. Trans. R. Soc. Lond., 1857.

[15] Mie G. Articles on the optical characteristics of turbid tubes, especially colloidal metal solutions. Annalen Der Physik 1908;25:377.

[16] Zsigmondy R. Richard Zsigmondy - Nobel Lecture. 1925.

[17] Link S, El-Sayed MA. Shape and size dependence of radiative, non-radiative and photothermal properties of gold nanocrystals. International Reviews in Physical Chemistry 2000;19:409.

[18] Roco MC. Nanotechnology: convergence with modern biology and medicine. Current Opinion in Biotechnology 2003;14:337.

[19] Roco MC. National Nanotechnology Initiative - Past, Present, Future. Handbook on Nanoscience, Engineering and Technology, 2007.

[20] Obonyo O, Fisher E, Edwards M, Douroumis D. Quantum dots synthesis and biological applications as imaging and drug delivery systems. Critical Reviews in Biotechnology 2010;30:283.

[21] Leobandung W, Ichikawa H, Fukumori Y, Peppas NA. Preparation of stable insulin-loaded nanospheres of poly(ethylene glycol) macromers and N-isopropyl acrylamide. Journal of Controlled Release 2002;80:357.

[22] Bianco A, Kostarelos K, Prato M. Applications of carbon nanotubes in drug delivery. Current Opinion in Chemical Biology 2005;9:674.

[23] Liu YL, Shipton MK, Ryan J, Kaufman ED, Franzen S, Feldheim DL. Synthesis, stability, and cellular internalization of gold nanoparticles containing mixed peptide-poly(ethylene glycol) monolayers. Analytical Chemistry 2007;79:2221.

[24] Jain PK, Huang X, El-Sayed IH, El-Sayad MA. Review of some interesting surface plasmon resonance-enhanced properties of noble metal nanoparticles and their applications to biosystems. Plasmonics 2007;2:107.

[25] Huang XH, Neretina S, El-Sayed MA. Gold Nanorods: From Synthesis and Properties to Biological and Biomedical Applications. Advanced Materials 2009;21:4880.

[26] Daniel MC, Astruc D. Gold nanoparticles: Assembly, supramolecular chemistry, quantum-size-related properties, and applications toward biology, catalysis, and nanotechnology. Chemical Reviews 2004;104:293.

[27] Han G, Ghosh P, Rotello VM. Functionalized gold nanoparticles for drug delivery. Nanomedicine 2007;2:113.

[28] Liao HW, Nehl CL, Hafner JH. Biomedical applications of plasmon resonant metal nanoparticles. Nanomedicine 2006;1:201.

[29] Cabrera-Trujillo JM, Montejano-Carrizales JM, Rodriguez-Lopez JL, Zhang W, Velazquez-Salazar JJ, Jose-Yacaman M. Nucleation and Growth of Stellated Gold Clusters: Experimental Synthesis and Theoretical Study. Journal of Physical Chemistry C 2010;114:21051.

[30] Huang XH, Jain PK, El-Sayed IH, El-Sayed MA. Plasmonic photothermal therapy (PPTT) using gold nanoparticles. Lasers in Medical Science 2008;23:217.

[31] Schartl W. Current directions in core-shell nanoparticle design. Nanoscale 2010;2:829.

[32] Lou XW, Archer LA, Yang ZC. Hollow Micro-/Nanostructures: Synthesis and Applications. Advanced Materials 2008;20:3987.

[33] Gou L, Murphy CJ. Fine-Tuning the Shape of Gold Nanorods. Chemistry of Materials 2005:3668

[34] Sau TK, Murphy CJ. Seeded high yield synthesis of short Au nanorods in aqueous solution. Langmuir 2004;20:6414.

[35] Nikoocakht B, El-Sayed MA. Preparation and Growth Mechanism of Gold Nanorods (NRs) Using Seed-Mediated Growth Method. Chemistry of Materials 2003;15:1957

[36] Stakenborg T, Peeters S, Reekmans G, Laureyn W, Jans H, Borghs G, Imberechts H. Increasing the stability of DNA-functionalized gold nanoparticles using mercaptoalkanes. Journal of Nanoparticle Research 2008;10:143.

[37] Hasan M, Bethell D, Brust M. The fate of sulfur-bound hydrogen on formation of self-assembled thiol monolayers on gold: H-1 NMR spectroscopic evidence from solutions of gold clusters. Journal of the American Chemical Society 2002;124:1132.

[38] Wijaya A, Hamad-Schifferli K. Ligand customization and DNA functionalization of gold nanorods via round-trip phase transfer ligand exchange. Langmuir 2008;24:9966.

[39] Larsson JA, Nolan M, Greer JC. Interactions between thiol molecular linkers and the Au-13 nanoparticle. Journal of Physical Chemistry B 2002;106:5931.

[40] Kah JC, Zubieta A, Saavedra RA, Hamad-Schifferli K. Stability of gold nanorods passivated with amphiphilic ligands. Langmuir 2012;28:8834.

[41] Park S, Hamad-Schifferli K. Evaluation of hydrodynamic size and zeta-potential of surface-modified an nanoparticle-DNA conjugates via Ferguson analysis. Journal of Physical Chemistry C 2008;112:7611.

[42] Lewinski N, Colvin V, Drezek R. Cytotoxicity of nanoparticles. Small 2008;4:26.

[43] Fadeel B, Garcia-Bennett AE. Better safe than sorry: Understanding the toxicological properties of inorganic nanoparticles manufactured for biomedical applications. Advanced Drug Delivery Reviews 2010;62:362.

[44] Johnston HJ, Hutchison G, Christensen FM, Peters S, Hankin S, Stone V. A review of the in vivo and in vitro toxicity of silver and gold particulates: Particle attributes and biological mechanisms responsible for the observed toxicity. Critical Reviews in Toxicology 2010;40:328.

[45] Eustis S, El-Sayed MA. Why gold nanoparticles are more precious than pretty gold: Noble metal surface plasmon resonance and its enhancement of the radiative and nonradiative properties of nanocrystals of different shapes. Chemical Society Reviews 2006;35:209.

[46] Lee KS, El-Sayed MA. Dependence of the enhanced optical scattering efficiency relative to that of absorption for gold metal nanorods on aspect ratio, size, end-cap shape, and medium refractive index. Journal of Physical Chemistry B 2005;109:20331.

[47] Lazarides AA, Schatz GC. DNA-linked metal nanosphere materials: Structural basis for the optical properties. Journal of Physical Chemistry B 2000;104:460.

[48] Jin RC, Wu GS, Li Z, Mirkin CA, Schatz GC. What controls the melting properties of DNA-linked gold nanoparticle assemblies? Journal of the American Chemical Society 2003;125:1643.

[49] Ghosh SK, Pal T. Interparticle coupling effect on the surface plasmon resonance of gold nanoparticles: From theory to applications. Chemical Reviews 2007;107:4797.

[50] Jain PK, Eustis S, El-Sayed MA. Plasmon coupling in nanorod assemblies: Optical absorption, discrete dipole approximation simulation, and exciton-coupling model. Journal of Physical Chemistry B 2006;110:18243.

[51] Mannelli I, Marco MP. Recent advances in analytical and bioanalysis applications of noble metal nanorods. Anal Bioanal Chem 2010;398:2451.

[52] Mitamura K, Imae T. Functionalization of Gold Nanorods Toward Their Applications. Plasmonics 2009;4:23.

[53] Westerlund F, Bjornholm T. Directed assembly of gold nanoparticles. Current Opinion in Colloid & Interface Science 2009;14:126.

[54] Kim F, Kwan S, Akana J, Yang PD. Langmuir-Blodgett nanorod assembly. Journal of the American Chemical Society 2001;123:4360.

[55] Zhen SJ, Huang CZ, Wang J, Li YF. End-to-End Assembly of Gold Nanorods on the Basis of Aptamer-Protein Recognition. Journal of Physical Chemistry C 2009;113:21543.

[56] Wang Y, DePrince AE, Gray SK, Lin XM, Pelton M. Solvent-Mediated End-to-End Assembly of Gold Nanorods. Journal of Physical Chemistry Letters 2010;1:2692.

[57] Nie ZH, Fava D, Kumacheva E, Ruda HE, Shik A. Plasmon spectra in two-dimensional nanorod arrays. Nanotechnology 2009;20:9.

[58] Chang JY, Wu HM, Chen H, Ling YC, Tan WH. Oriented assembly of Au nanorods using biorecognition system. Chemical Communications 2005:1092.

[59] Connolly S, Cobbe S, Fitzmaurice D. Effects of ligand-receptor geometry and stoichiometry on protein-induced aggregation of biotin-modified colloidal gold. Journal of Physical Chemistry B 2001;105:2222.

[60] Wang WJ, Chen CL, Qian MX, Zhao XS. Aptamer biosensor for protein detection using gold nanoparticles. Analytical Biochemistry 2008;373:213.

[61] Ying-Ying Huang MHaAC-HC. Low-level laser therapy: an emerging clinical paradigm. SPIE Newsroom, 2009.

[62] Link S, Burda C, Nikoobakht B, El-Sayed MA. Laser-induced shape changes of colloidal gold nanorods using femtosecond and nanosecond laser pulses. Journal of Physical Chemistry B 2000;104:6152.

[63] Alpert J, Hamad-Schifferli K. Effect of Ligands on Thermal Dissipation from Gold Nanorods. Langmuir 2010;26:3786.

[64] Link S, Burda C, Mohamed MB, Nikoobakht B, El-Sayed MA. Laser photothermal melting and fragmentation of gold nanorods: Energy and laser pulse-width dependence. Journal of Physical Chemistry A 1999;103:1165.

[65] Link S, El-Sayed MA. Spectral properties and relaxation dynamics of surface plasmon electronic oscillations in gold and silver nanodots and nanorods. Journal of Physical Chemistry B 1999;103:8410.

[66] Link S, Burda C, Nikoobakht B, El-Sayed MA. How long does it take to melt a gold nanorod? A femtosecond pump-probe absorption spectroscopic study. Chemical Physics Letters 1999;315:12.

[67] Link S, El-Sayed MA. Spectroscopic determination of the melting energy of a gold nanorod. Journal of Chemical Physics 2001;114:2362.

[68] Jain PK, Qian W, El-Sayed MA. Ultrafast cooling of photoexcited electrons in gold nanoparticle-thiolated DNA conjugates involves the dissociation of the gold-thiol bond. Journal of the American Chemical Society 2006;128:2426.

[69] Wijaya A, Schaffer SB, Pallares IG, Hamad-Schifferli K. Selective Release of Multiple DNA Oligonucleotides from Gold Nanorods. Acs Nano 2009;3:80.

[70] Stryer L. Biochemistry. New York: W.H. Freeman, 1995.

[71] Drahl C. To Clot, Or Not. vol. 88: Chemical & Engineering News, 2010. p.15.

[72] Coughlin SR. Thrombin signalling and protease-activated receptors. Nature 2000;407:258.

[73] Klussman S. The Aptamer Handbook: Functional Oligonucleotides and Their Applications. Weinheim: Wiley-VCH, 2006.

[74] Bock LC, Griffin LC, Latham JA, Vermaas EH, Toole JJ. Selection of single-stranded DNA molecules that bind and inhibit human thrombin. 1992;355:564.

[75] Jenison RD, Jennings SD, Walker DW, Bargatze RF, Parma D. Oligonucleotide inhibitors of P-selectin-dependent neutrophil-platelet adhesion. Antisense & Nucleic Acid Drug Development 1998;8:265.

[76] Rhie A, Kirby L, Sayer N, Wellesley R, Disterer P, Sylvester I, Gill A, Hope J, James W, Tahiri-Alaoui A. Characterization of 2 '-fluoro-RNA aptamers that bind preferentially to disease-associated conformations of prion protein and inhibit conversion. Journal of Biological Chemistry 2003;278:39697.

[77] Tasset DM, Kubik MF, Steiner W. Oligonucleotide inhibitors of human thrombin that bind distinct epitopes. 1997;272:688.

[78] Pagano B, Martino L, Randazzo A, Giancola C. Stability and binding properties of a modified thrombin binding aptamer. Biophysical Journal 2008;94:562.

[79] Griffin LC, Toole JJ, Leung LLK. The discovery and characterization of a novel nucleotide-based thrombin inhibitor. Gene 1993;137:25.

[80] Griffin LC, Tidmarsh GF, Bock LC, Toole JJ, Leung LLK. Invivo anticoagulant properties of a novel nucleotide-based thrombin inhibitor and demonstration of regional anticoagulation in extracorporeal circuits. Blood 1993;81:3271.

[81] Macaya RF, Schultze P, Smith FW, Roe JA, Feigon J. Thrombin-binding dna aptamer forms a unimolecular quadruplex structure in solution. Proceedings of the National Academy of Sciences of the United States of America 1993;90:3745.

[82] Pagba CV, Lane SM, Cho HS, Wachsmann-Hogiu S. Direct detection of aptamer-thrombin binding via surface-enhanced Raman spectroscopy. Journal of Biomedical Optics 2010;15:8.

[83] Mao XA, Marky LA, Gmeiner WH. NMR structure of the thrombin-binding DNA aptamer stabilized by Sr2+. Journal of Biomolecular Structure & Dynamics 2004;22:25.

[84] Hong ES, Yoon HJ, Kim B, Yim YH, So HY, Shin SK. Mass Spectrometric Studies of Alkali Metal Ion Binding on Thrombin-Binding Aptamer DNA. Journal of the American Society for Mass Spectrometry 2010;21:1245.

[85] Kankia BI, Marky LA. Folding of the thrombin aptamer into a G-quadruplex with Sr2+: Stability, heat, and hydration. Journal of the American Chemical Society 2001;123:10799.

[86] Trajkovski M, Sket P, Plavec J. Cation localization and movement within DNA thrombin binding aptamer in solution. Org Biomol Chem 2009;7:4677.

[87] Hianik T, Ostatna V, Sonlajtnerova M, Grman I. Influence of ionic strength, pH and aptamer configuration for binding affinity to thrombin. Bioelectrochemistry 2007;70:127.

[88] Baldrich E, O'Sullivan CK. Ability of thrombin to act as molecular chaperone, inducing formation of quadruplex structure of thrombin-binding aptamer. Analytical Biochemistry 2005;341:194.

[89] Pavlov V, Xiao Y, Shlyahovsky B, Willner I. Aptamer-functionalized Au nanoparticles for the amplified optical detection of thrombin. Journal of the American Chemical Society 2004;126:11768.

[90] Joachimi A, Mayer G, Hartig JS. A new anticoagulant-antidote pair: Control of thrombin activity by aptamers and porphyrins. Journal of the American Chemical Society 2007;129:3036.

[91] Dittmer WU, Reuter A, Simmel FC. A DNA-based machine that can cyclically bind and release thrombin. Angewandte Chemie-International Edition 2004;43:3550.

2. Materials and Methods

2.1. Synthesis of gold nanoparticles

The optical properties of gold nanoparticles (NP) strongly depend on their morphology. Therefore, in recent years, there has been intense research on the synthesis methods to produce gold nanoparticles of precise sizes and shapes. The optical properties of spherical gold nanoparticles slightly vary depending on their diameter. However, if the particles are anisotropic, a slight change in one of their dimensions leads to a huge difference in the absorption spectrum of the particles. This Chapter will cover some synthesis procedures of gold nanorods (NRs), long gold nanocapsules (NCs), gold nanobones (NBs) and different sizes of gold nanospheres (NS).

2.1.1. Gold nanorods

Gold nanorods (NRs) are synthesized using a single surfactant non-seed-mediated growth method[1] in 200mL batches. In a typical synthesis, 2.4mL of 50mM gold chloride trihydrate ($HAuCl_4$) are added to 189.6ml of 150mM cetyltrimethylammonium bromide (CTAB) solution mixed with 3ml of 100mM sodium chloride (NaCl), and the solution turns orange; 2.4ml of 10mM silver nitrate ($AgNO_3$) are added to the solution, followed by gentle mixing; 2.4 ml of 100mM ascorbic acid (AA) are added, followed by inversion

until the solution turns colorless. Finally, 0.128 ml of 3.125mM sodium borohydride ($NaBH_4$) is added. The solution sits on the bench undisturbed overnight, during which time it turns reddish brown, indicating the presence of NRs. TEM analysis shows that the NRs have a length of 34.7 ±5.3nm a width of 9.6 ±1.2nm (Fig. 2-1, left) and an aspect ratio of 3.6±0.7. The absorbance of the NRs shows one absorbance peak at 770 nm, and another peak at 511nm (Fig 2-1, right). The absorbance ratio for these particles is around 3.7.

$HAuCl_4$ + CTAB + $AgNO_3$ + ascorbic acid + $NaBH_4$ → AuNR

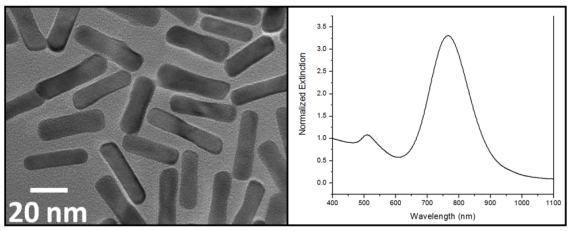

Figure 2-1: TEM image and absorbance graph of synthesized NR

2.1.2 Gold nanocapsules and Gold nanobones

Long gold nanocapsules (NC) and gold nanobones (NB) are synthesized by a binary-surfactant seed-mediated growth method. The co-surfactants are CTAB and benyldimethylhexadecylammonium chloride (BDAC). This synthesis method is typically divided in two steps: preparation of the gold seeds and the growth of the NC.

The seed preparation step consists in a rapid reduction of the gold ion in the presence of CTAB. In a typical protocol, 7.5ml of a 0.2M CTAB solution are mixed with 0.25ml of 0.001M$HAuCl_4$ in a beaker. While the solution is vigorously stirred, 0.6ml of ice-cold 0.01M $NaBH_4$ is added and the solution turns brownish yellow. Vigorous stirring continues for 2 minutes.

During the growth step of nanorods, there is a slow deposition of gold atoms onto the added seeds in anisotropic way, which results in elongation of the seeds to form gold nanocapsules. In a typical protocol, 25ml of 0.001M $HAuCl_4$ is added into a mixture of 10ml of 0.2M CTAB and 15ml of 0.3M BDAC in a glass bottle, and the solution turns orange. 1ml of 0.004M $AgNO_3$ is added to the solution, followed by gentle mixing until the solution turns colorless. 0.05ml of the seed solution is added to the growth solution. The solution sits undisturbed overnight and turns reddish-purple, and NCs are formed. In order to turn these long nanocapsules into nanobones, it is necessary to add 1ml of 100mM AA to 54ml of synthesized NC solution, in order to finally reduce the gold salt that has not reacted overnight. The reason for preferable binding of the gold on the sides of the NCs is due to molecular rearrangements of the BDAC and CTAB overnight, after the synthesis of the long capsules has finished. It is believed that the CTAB and BDAC[2] rearrangement after the formation of the NCs creates a preferable binding of

the gold ions on the sides of the NCs. This AA will reduce the gold that is still in solution preferably on the sides of the NC, due to the presence of CTAB and BDAC. TEM imaging shows that the NCs have a length of 80-90nm a width of 10-12nm (Fig 2-2, middle) and an aspect ratio of 7-10. The absorbance of the NCs shows one absorbance peak at 1050-1100 nm (Fig. 2-2, left), and another peak at around 530nm. The absorbance ratio for these particles is 2.

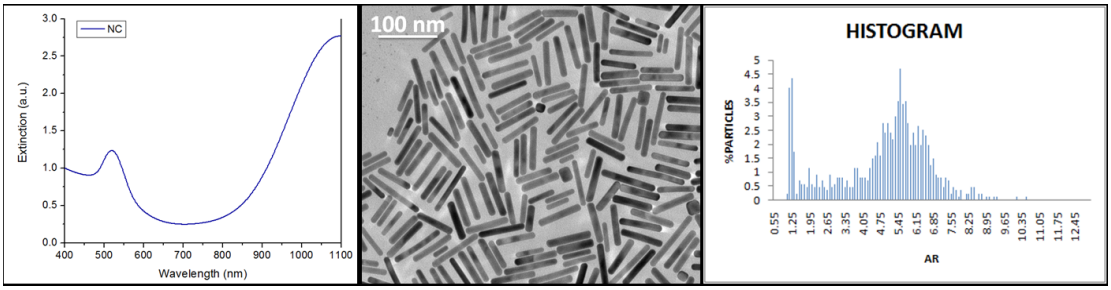

Figure 2-2: Extinction plot, TEM and histogram of the synthesized NC

Gold nanobones were synthesized by adding AA to the prepared NCs, to further increase their dimensions. AA was added to reduce remaining Au^{+} present in the synthesis solution that bound preferentially to the sides of the NCs, forming dogbone-shaped particles TEM imaging shows that the NBs measured 59.4 ± 13.7 nm × 12.5 ± 2.4 nm, with an AR of 4.8 (image 2-3, right). The absorbance of the NCs shows one absorbance peak at 1050-1150 nm (Fig. 2-3, left), and another peak at around 530nm.

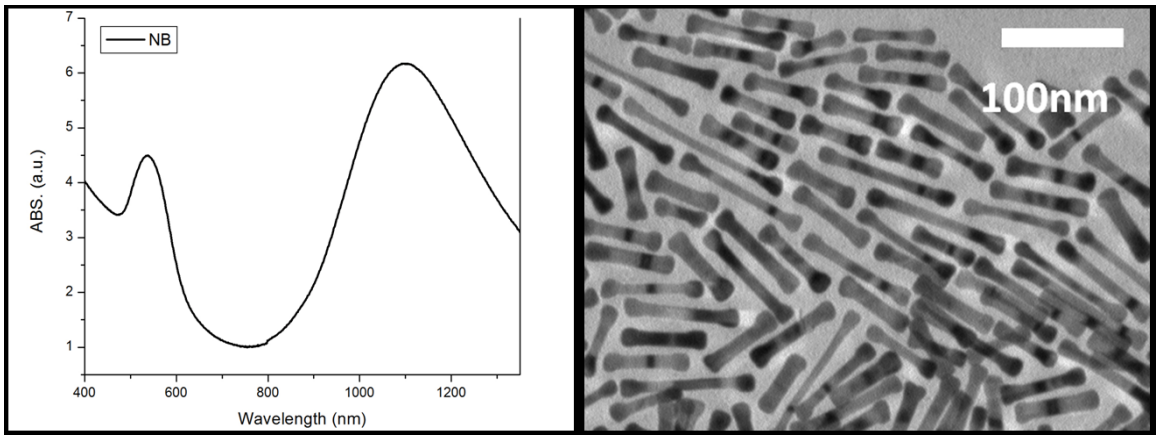

Figure 2-3: Extinction plot and TEM of the synthesized NBs

2.1.3. Gold nanospheres

Gold nanospheres of different diameters are synthesized using a single surfactant seed-mediated growth method[3], using CTAB as the surfactant in order to obtain similar surface properties to the NRs. In order to synthesize them, first 3.5±0.7nm gold seeds were prepared by adding 0.6mL of ice-cold, freshly prepared 0.1M $NaBH_4$ solution to a 20ml solution containing 0.25mM trisodium citrate and 0.25mM $HAuCl_4$, while the solution was stirring. After the addition of the $NaBH_4$, the solution turns pink/orange immediately, indicating the particles formation. This seed solution is used within 2-5 hours after its formation.

Next, a solution containing 80mM CTAB and 2.5mM $HAuCl_4$ (growth solution) was prepared. The different NS synthesis will be obtained by adding different volumes of

growth solution and seed solution, as indicated in table 2-1. For example, in order to synthesize 9.44nm NS, 0.5ml of 0.1M freshly prepared AA are added to 9ml of the growth solution while the solution is stirring. Stirring continues until the solution turns clear. Next, 10ml of the seed solution are added, and stirring continues for 10min.

Diameter	Growth solution (ml)	0.1M AA (ml)	Seed (ml)
6.71±1.48nm	7.5	0.5	25
9.44±1.26nm	9	0.5	10
12.4±2.35nm	9	0.5	3

Table 2-1: Parameters for the synthesis of NS of different sizes

Dynamic light scattering (DLS) and TEM imaging were used to measure the diameter of the NS (Fig. 2-4).

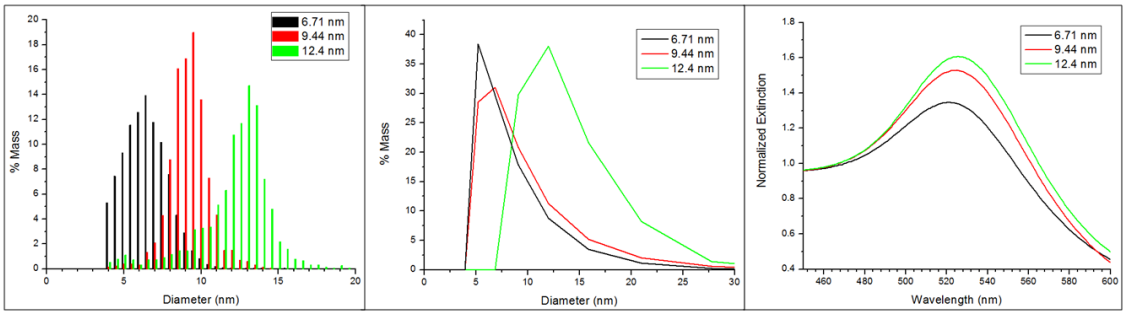

Figure 2-4: TEM Histogram (left), DLS (middle) and extinction (right) of the synthesized NS

In figure 2-5, one can see three different TEM images for each of the syntheses. From left to right, the NS are: 6.71nm, 9.44nm and 12.4nm. The scale bar is 100nm. NS are well-separated, spherical, and monodisperse, indicating high-quality samples.

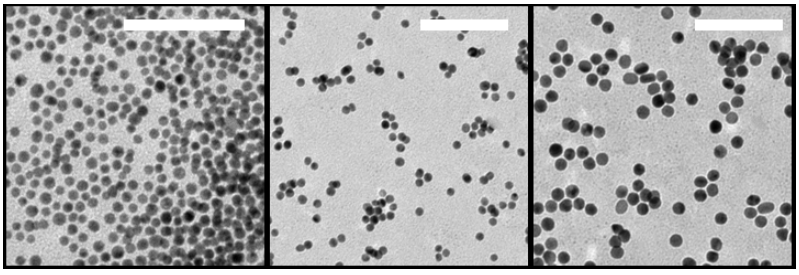

Figure 2-5: TEM images of the NS

The synthesis of metal nanoparticles from their salt solutions can be divided into three distinct processes: cation reduction, nucleation, and growth. However, the formation mechanism of NRs in aqueous surfactant media is still not completely clear. Most authors[4-13] agree on the idea CTAB absorbs on the NRs forming a bilayer, with the trimethylammonium headgroups of the first monolayer facing the gold surface[14], Murphy and co-workers[9] proposed that once the seed grows to a critical size, the CTAB headgroup preferentially binds to the crystallographic faces of gold existing along the sides of the rods, as compared to the faces at the tips. Therefore, the growth of gold nanorods would be governed by preferential absorption of CTAB to different crystal faces

during the growth. The different growth rates in different facets are what enable the long shape of NRs.

Some studies show that the length of the hydrocarbon tail of the CTAB molecule in the synthesis of NRs is critical to control the length and the yield of the formed NRs, when longer chain lengths produce longer nanorods in higher yields and shorter chains produce shorter nanorods in lower yields. Therefore, we can think that more stable bilayers promote the formation of longer NR[15]. The role of the CTAB counterion was also considered[6, 7], concluding that only brominated long chain surfactants lead to significant yields of rod shaped particles. These studies study the role of an *in situ* formed complex of CTAB and silver bromide that would be responsible for the anisotropic growth of the NRs.

The role of Ag^+ ions in the growth of NR has, as well, been extensively studied. Most authors agree that the Ag^+ reacts with CTAB and forms silver bromide that absorbe onto preferential NR's facets and thus decreases their growth in these directions [2, 6-8, 10]. Nikoobakht and El-Sayed explained that the Ag–Br pairs decrease the charge density of bromide ions and thus decrease the repulsion of neighboring CTAB headgroups. This repulsion results in CTAB elongation and thus NR formation. Other authors explain that although Ag in the CTAB solution cannot be reduced to bulk silver atoms by ascorbic

acid in acidic pH. Ag can be reduced to Ag^0 onto a metal substrate in the form of a metal monolayer at a potential much less than bulk reduction, known as underpotential deposition (UPD). Therefore, they propose that the silver deposition on the long side of the NRs is faster than on the ends due to UDP effects, and thus the seeds grow into NRs. Thus, by controlling the concentration of silver nitrate in the growth solution it is possible to control the optical properties of the synthesized NRs. In figure 2-6 [10], we can see that by increasing the silver concentration, the longitudinal plasmon band redshifts and its intensity increases-the silver concentration increases from sample 1 to 5-. By observing the size distribution of the particles, we can observe that the aspect ratio of the particles increases as well.

The ability of ascorbic acid (AA) to reduce Au^{3+} halides to metals has been known for decades and has been utilized in both qualitative and quantitative determination of gold[16]. During the synthesis of NRs, the AA would reduce the Au^{3+} to Au^{+}. After the AA reduction, the $NaBH_4$ would reduce the Au^{+} to Au^0, and start the seed formation.

2.2. Loading of DNA on NPs by thiol chemistry

For different types of NPs, slightly different protocols should be used. In this thesis, we will explain the procedures for NRs, and explain, in some cases, the specific differences with other types of NP.

After the synthesis of the NRs, it is necessary to wash the excess reagents and concentrate the sample. In order to do so, the NRs are washed and concentrated by centrifugation (60 min at 7000 relative centrifugal force (RCF) for a 200 mL sample) to reduce their volume. After this wash, the supernatant is discarded and the pellets are resuspended in 1mM CTAB and centrifuged at 4000 RPF for 90 min. After the particles have precipitated during this second wash, the pellets are resuspended in 10mM CTAB and centrifuged, again at 7000 RPF for 90min. Finally, all the pellets can be mixed and the concentrated NRs can be stored in 10mM CTAB.

2.2.1. Ligand exchange of gold nanoparticles

After the synthesis and wash of nanoparticles they are stabilized by a double layer of CTAB, which is problematic for stability, bioconjugation, nonspecific absorption of DNA and cytotoxicity. Therefore, in order to tune the biological properties of the gold nanorods-DNA conjugates, the ligand exchange must reduce nonspecific absorption and enable ligand customization. Desirable ligands are those that can be covalently attached

to the NR via a thiol (SH), and a chain that is biocompatible (PEG) or an endgroup that permits water solubility (COO-). The round trip phase transfer ligand-exchange[17] enables the customization of the ligand and a uniform charge distribution on the NR surface. Because the ligand exchange involves extraction from an aqueous phase to an organic phase, and then back to an aqueous phase, the probability that any CTAB remains on the surface of the NR is minimal, in contrast with other ligand exchange attempts, that are done in a single phase, and therefore, some residual CTAB remains on the surface.

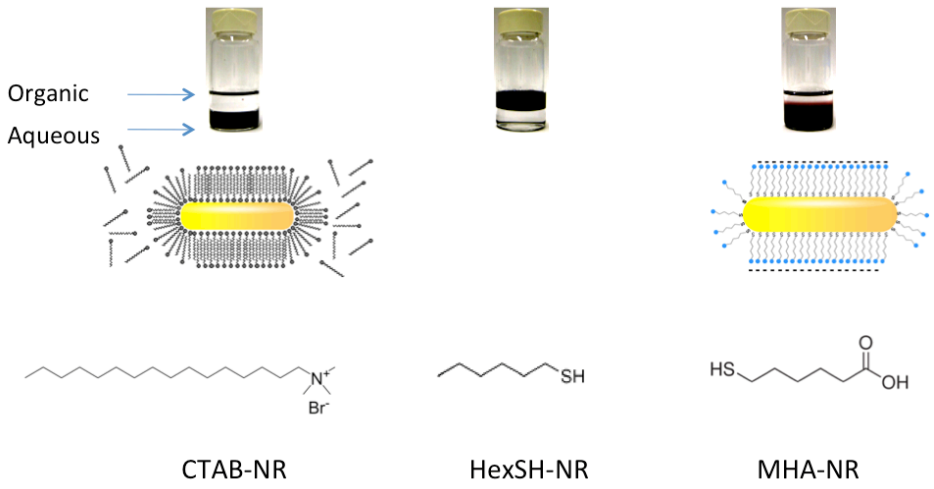

Figure 2-6: Method for NR ligand exchange[17]. Adapted with permission from Wijaya A, Schaffer SB, Pallares IG, Hamad-Schifferli K. Selective Release of Multiple DNA Oligonucleotides from Gold Nanorods. ACS Nano 2008;3:80. Copyright 2008 American Chemical Society.

Figure 2-6 shows a schematic representation of ligand exchange on gold nanorods. First, the concentrated NR stabilized with CTAB in water are put in contact with either dodecanethiol (DDT) or 1-hexanethiol (HexSH). In order to extract the NRs into the organic ligand, it is necessary the addition of acetone and swirling the solution for a few seconds. After 30 min, the aqueous phase becomes clear, which indicates that no NRs remain soluble in water. To remove the excess DDT or Hex-SH, the NRs are diluted in toluene and collected by centrifugation.

Next, organic-to aqueous phase transfer is performed. The collected NRs are resuspended in 9 mL of 0.01 M MCA (three different mercaptocarboxilic acids have been used: mercaptohexanoic acid (MHA), mercaptoundecanoic acid (MUDA) and mercaptohexadecanoic acid (MHDA)) in toluene at 95 °C and vigorously stirred until visible aggregation is observed (within 15 min), and then the MCA coated NRs (MCA-NR) are allowed to settle and cool to room temperature. The precipitation of NR indicates that they are successfully coated by MCA, thus insoluble in toluene. The NR are washed with toluene to remove the excess MCA and with isopropanol to deprotonate the carboxylic acid. The aggregates spontaneously re-disperse in 0.5x tris-borate-EDTA buffer (TBE) and are no longer soluble in toluene. Finally, these MCA-NRs are washed and resuspended in 10mM Phosphate Buffer.

It is necessary to take into account the length of the ligand of the particles during the ligand exchange, as it is important for the solubility of each ligand in toluene, and it will be an important factor in the DNA conjugation of the NPs.

Gel electrophoresis of the NPs shows a successful ligand exchange of the particles. Figure 2-7 shows gel electrophoresis results of the NR in CTAB (lane 1), the NRs-MUDA (lane 2) and NR-MHDA (lane 3). As previously explained, the CTAB forms a bilayer on the NRs surface, but as it is not covalently bound to it, and due to the pH of the TBE solution, it can come off the particles, causing them to aggregate [18]. On the other hand, MUDA and MHDA are bound to the NRs by a thiol bond. Therefore, the particles are still stable while they run in the gel. It is not surprising either that the MUDA particles run faster in the gel than the MHDA particles because, even if they have a similar charge on their surface, the size of MHDA is bigger than MUDA, thus the overall size of the particles is bigger for the MHDA particles than for the MUDA particles.

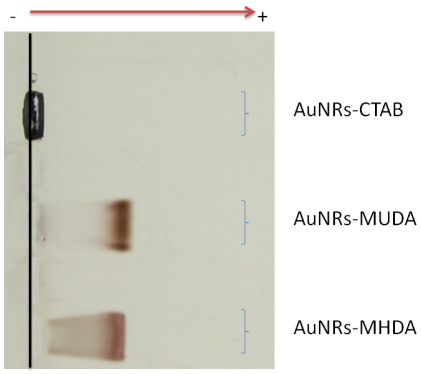

Figure 2-7: Gel electrophoresis of the NRs-CTAB; NRs-MUDA and NRs-MHDA

A PEG binding can be performed after the round trip ligand exchange. In order to do so, the MUDA conjugated NPs are conjugated overnight with 1mM PEG of three different molecular weights (MW=356; MW=1000 and MW=5000). We are able to successfully demonstrate the conjugation by gel electrophoresis. In figure 2-8, we can observe the NRs coated with MUDA on the first lane. On the 2nd to 4th lanes, we can see the NRs coated with PEG_{365}. PEG_{365} is smaller in size than MUDA, but also has a lower charge. Therefore, it is not surprising that even if the overall charge of the particles is lower, due to their smaller size, they end up running faster than the MUDA particles. On the 5th to 7th lanes, we can see the PEG_{1000} coated NRs; as their size is bigger than the NRs coated with PEG_{365}, they do not run as far in the gel. Finally, in lanes 8th to 10th we can see the PEG_{5000} NRs run in the negative direction, indicating an overall positive charge of the particles.

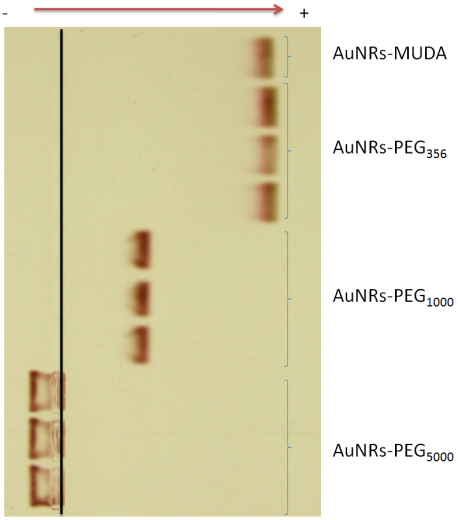

Figure 2-8: Gel electrophoresis of PEG-NRs

2.2.2. Salt stability of the gold nanoparticles

After coating the particles with MCA, and before the DNA conjugation it is important to test the salt stability in order to further check that the binding was complete. Also, we can see that the particles can hold a critical salt concentration over which they aggregate. This threshold concentration can be measured by absorbance of the particles, and it can also be approximated by observing their change of color and precipitation at high salt concentrations. In the case of the MHA-NRs, it is important not to add more salt than the critical salt concentration, as the particles will irreversibly aggregate. One can observe that after the DNA conjugation, the particles are stable at higher NaCl concentrations, due to an increase of the charge on their surface.

2.2.3. DNA conjugation of gold nanoparticles

In order to use the gold nanorods to control blood clotting, they will need to be conjugated with ssDNA. These sequences were purchased from Integrated DNA Technologies (IDT) with a thiol group in one of their ends, in order to enable the S-Au bond form on the gold surface. Because after the ligand exchange the gold nanoparticles have a negative charge on their surface and the DNA is also negatively charged, it will be necessary to add salt, to screen the charges and obtain a high coverage of DNA on the particles' surface.

After the ligand exchange, the MHA-NR can be further conjugated with DNA *via* thiol conjugation through a charge screening method[19, 20]. The thiolated DNA oligonucleotides (SH-DNA), are fluorescently labeled at the 3' ends with either 6-carboxyfluorescein (FAM) or tetramethylrhodamine (TMR) and purchased from Integrated DNA Technologies. The sequences used are 5'-SH-TTTTT TTTTT TTTTT GGTTG GTGTG GTTGG-TMR-3' (SH-T_{15}-TBA); 5'-SH-GGTTG GTGTG GTTGG-TMR-3' (SH-TBA), 5'-SH-TTTTT TTTTT TTTTT CCAAC CACAC CAACC-FAM-3' (SH-T_{15}Anti), 5'-SH-CCAAC CACAC CAACC-FAM-3' (SH-Anti).

In order to conjugate the MHA-NR with SH-DNA, first the SH-DNA has to be reduced by tris[2 -carboxyethyl]phosphine (TCEP) with TCEP/DNA ratio of 100:1. Then, 6nM

NR are incubated with the reduced SH-DNA, in 10 mM phosphate buffer with 0.3% SDS concentration. SH-DNA to NR ratios are 1000 SH-DNA/NR in order to get a high coverage on the NRs and 200 SH-DNA/NR to obtain a low coverage on the NR's surface. After 3 h of incubation, charge screening is performed until the critical salt concentration, which depends on the NR synthesis and Ligand Exchange. The charge screening consists in adding a volume of salting buffer (typically 0.6M NaCl in 0.3%SDS) every 30 min during an hour (a total of three additions) followed by 10s sonication. After this step, the samples are incubated at room temperature for 36 hours, during which time the samples are sonicated every 12 hours.

The DNA conjugation on the NR can be confirmed by observing the mobility of the DNA-NR with respect to the MHA-NR in gel electrophoresis with 0.5% agarose gels in 0.5x TBE (Fig 2-9). Glycerol is used to load the samples and ensure that they stay in the wells prior to travelling in the gel matrix. Moreover, we are able to quantify the amount of SH-DNA per particle by chemically displacing[21, 22] the conjugated SH-DNA with 1mM mercaptohexanol (MCH). After overnight incubation, the free DNA is separated from the NR by centrifugation and quantified *via* fluorescence spectroscopy of the fluorophore labels. We measured 135 T_{15}-TBA/NR on the high coverage conjugation, 62 T_{15}-TBA/NR on the low coverage conjugation.

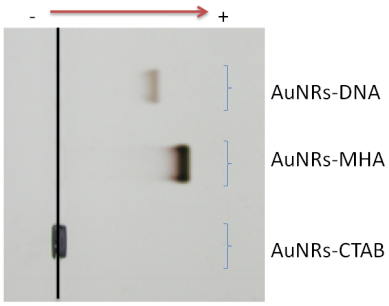

Figure 2-9: NR-CTAB; NR-MHA and NR-DNA

The loading of oligonucleotides on gold nanoparticles depends on (1) the salt induced aging procedures used to decrease electrostatic interactions between neighboring oligonucleotides and between oligonucleotides and the NRs, (2) the size and shape of the particles, (3) the ligand on their surface and (4) the oligonucleotide sequence. Moreover, other parameters such as the sonication of the particles play an important role during the DNA conjugation

The amount of oligonucleotides attached to the surface of the particles increases with the NaCl concentration in solution. NaCl is used to screen the charges between neighboring oligonucleotides and between the DNA and the surface of the particles, thus enabling the Au-S bond and a high coverage of DNA on the surface of the particles. The charge screening has to be performed carefully, as the addition of NaCl over the critical NaCl concentration causes NRs to aggregate. In order to calculate the critical NaCl

concentration at which MHA-NR can be exposed without aggregation, an aliquot of the NR is added different concentrations of NaCl, until the particles aggregate. One can see the nanoparticles turn blue, or measure the change by absorbance. The critical NaCl concentration is the highest concentration at which the particles do not aggregate. This critical NaCl concentration depends on the ligand on the particle's surface –a longer ligand will give more protection to the particles against aggregation- and on the size and shape of the particles.

Another key parameter when loading DNA on the surface of gold nanorods is their size and shape[23]. The available surface for the S-Au bond to form will differ with the NRs measures.

By calculating the footprint of an oligonucleotide on a gold nanoparticle, Mirkin group have mathematically calculated the maximum amount of DNA that can be conjugated on a NR surface by using the following formula:

$$\frac{DNA}{NR} = \frac{2\pi r^2}{17.55} + \frac{2\pi r}{2\sqrt{\frac{3.3618\ln(r)+0.1616}{\pi}}} * \frac{l}{4.72} \qquad \text{(Eq. 2.1)}$$

When we apply this formula on the NRs synthesized in Chapter 3 –where TEM imaging showed an average length of 34.7 ±5.3nm and an average width of 9.6 ±1.2nm, the

maximum loading of oligonucleotides per particle would be 115±25 DNA/NR. Which is very close to the previously measured 135 DNA/NR.

Another key parameter that is very important when conjugating DNA on the surface of NRs is their ligand. We have observed that MHDA and MUDA enable lower coverage on the particles than MHA. A reason for that is that the MHA is much shorter than the MHDA and the MUDA.

Moreover, the sequence of DNA used for the conjugation will also be a key factor when conjugating DNA on the particle's surface. We can compare the coverage of DNA between 5'-SH-TTTTT TTTTT TTTTT GGTTG GTGTG GTTGG-TMR-3' (SH-T_{15}-TBA) and 5'-SH-GGTTG GTGTG GTTGG-TMR-3' (SH-TBA). And we observe an average 135 DNA/NR on the case of T_{15}-TBA and an average of 320 DNA/NR for the SH-TBA. It is noticeable that the coverage on the second sequence is much higher that the monolayer coverage explained above. The explanation for that is that this DNA sequence has a secondary structure (G-Quadruplex, figure 2-10) that can lead to the formation of intermolecular G-Quadruplexes. Thus, by using the sequence SH-DNA not all the DNA is specifically attached on the particles' surface by a S-Au bond.

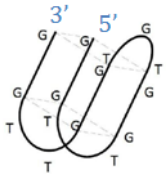

Figure 2-10: Secondary structure of the thrombin binding aptamer (TBA)

Another case where the importance of the sequence has been tested is when trying the conjugation of the following oligonucleotides: 5'-SH-TTTTT TTTTT TTTTT CCAAC CACAC CAACC-FAM-3' and 5'-FAM-CCAAC CACAC CAACC TTTTT TTTTT TTTTT-SH-3'. The spacer between the thiol and the first base is a C_6 for the first sequence and a C_3 for the second sequence, and the coverage is 105 DNA/NR and 0 DNA/NR respectively. Therefore, when the DNA sequence has a longer spacer between the thiol and the first base, there will be more loading on the particles.

2.2.4. Surface modifications on the DNA-conjugated NRs

After the DNA conjugation of the NRs, it is possible to perform surface modification in order to tune the properties of the gold nanoparticles.

2.2.4.1. HSA block

Human Serum Albumin (HSA) is a very common protein in blood. It is commonly used in a myriad of applications to block surfaces, such as in NP stabilization or microfluidic

channels. Because it tends to attach on surfaces, we can use it to block the surface of the NR. We add a 0.3% HSA in solution, in order to ensure that the surface of the particles is blocked.

2.2.4.2. PEG backfill

The DNA-NR can be further exchanged with thiolated PEG (mPEG), that would increase their stability and biocompatibility[24-28]. Other studies on bulk and nanoparticle surfaces have found that PEG is an ideal molecule for reducing surface fouling and non-specific adsorption. In our case, we have been able to successfully backfill with mPEG of two different molecular weights (5000 and 1000). The PEG-backfill was achieved by incubating the T_{15}-TBA-NR solution with mPEG. The DNA:PEG ratio was 1:2 for the low PEG-backfill and 1:5 for the High PEG backfill. We confirmed the PEG-backfill by observing the mobility change of the PEG-DNA-NR in respect to the DNA-NR in gel electrophoresis with 0.3% agarose gels in 0.5x TBE (Fig. 2-11).

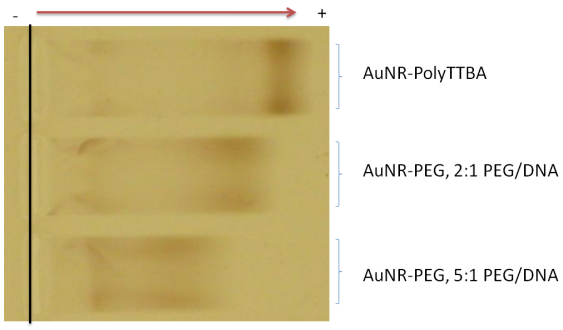

Figure 2-11: Gel of PEG-backfilled NRs

In figure 11, one can see in the first lane, the original DNA conjugated NRs. On the second and third lanes there are DNA-NRs that have been PEG-backfilled. On the second lane, there is double the amount of PEG than the amount of DNA, and in the third lane, the concentration of PEG added to the sample is 5 times higher than the original concentration of DNA attached.

2.3. HS Corona conjugation on NP surfaces

Loading of ssDNA on gold nanoparticles can also be achieved by taking advantage of protein coronas, which weakly and dynamically bind to the NPs. Such protein coronas enable for enhanced loading on the NPs[18], and may also reduce toxicity of the NPs, as serum proteins are already present in blood. Some proteins have a stronger binding to the NPs than others, and interestingly, HSA is not one of the strong binders to NPs[29]. Different binding strategies for the formation of the coronas were followed (See Chapter 5). In a typical experiment, synthesized NPs were spun down after the synthesis, and the NP pellet was resuspended in MilliQ water. After, particles were spun at 12000rcf, and resuspended in 5mM CTAB, for storage. In order to prepare the NP-coronas, particles were spun down for 15 min at 12000rcf, and the pellet was resuspended in a mixture of 1uM DNA, 5%HS, 5mMPB, followed by incubation at 37^{o}C overnight. The following day, particles were sonicated and centrifuged at 7000rcf for 15min, and washed three times in PB, prior to use.

Carbon nanotube solubilization and characterization

For some of the experiments, we produced protein coronas on carbon nanotubes (CNT). CNTs were purchased from Sigma-Aldrich and were dispersed with CTAB. Highly well-dispersed CNT-CTAB were obtained after dissolving the CNT in CTAB 5 mM (2

mg/mL), sonication (2 h) and centrifugation (16200 xg, 1 h) to isolate from the bundles. A set of dispersions (from 2.5 μg/mL to 40 μg/mL) was prepared by diluting the original dispersion (CNT-CNT 2 mg/mL) with CTAB 5 mM. These dispersions were ultrasonicated for 30 min before UV-Vis analysis. The absorptions at 500 nm were used to determine the concentration of the final well-dispersed CNT. Knowing that the purchased CNT were 5 μm length, 15 nm diameter and 2.1 g/mL density average, the concentration obtained was converted to nM.

CNT-CTAB conjugates were washed with MilliQ by using centrifuge filters (Amicon Ultra-0.5 mL, Merck Millipore). Coronas were prepared on the CNT by following the same protocol as for the NPs.

2.4. Laser Irradiation of NR

Laser irradiations were performed using pulsed femtosecond light. For the 800nm irradiation, the 532nm output of a Q-switched Nd:YLF laser (Empower, Spectra-Physics) was used to pump a Ti:Sapphire regenerative amplifier (Spitfire, Spectra-Physics), which amplifies the 82MHz output of a Ti:Sapphire oscillator, producing 50-475μJ light centered at 800nm, with a duration of 100fs, a repetition rate of 1kHz, and a spot size of 6mm. The 1100nm irradiation was achieved with a two-stage BBO/$KNbO_3$ optical parametric amplifier (Femtolasers: 30fs, 1kHz, 800nm), producing 2-6-13.6μJ pulses, with a duration of 45fs, and a repetition rate of 1kHz, centered at 1100nm, with a spot size of 1mm. In a typical experiment, 100μl of the NR-NB mixture were irradiated in a 3x3mm quartz cuvette for 20min. After irradiation, samples were spun at 14000rcf for 15min, and the supernatants were collected to quantify the DNA released and for blood clotting tests. NR melting was confirmed by observing a decrease in their absorbance spectra.

2.5. Blood clotting tests

Plasma equivalent thrombin time was measured using a Hemochron Signature Elite (ITC). It is a standard test to measure the activity of anticoagulants. In order to measure blood clotting time, disposable cuvettes are loaded into the Hemochron and clotting time is measured by counting the time that it takes for blood to coagulate, with the use of an optical sensor. Both thrombin clotting time (TCT) and activated thromboplastin clotting time (aPTT) were measured. In a typical TCT experiment, 14.4µl of the sample were mixed with 1.8µl of 100nM thrombin and 1.8µl of 1.37M NaCl, and incubated at 37^{o}C for 10min. After mixing with 27µl of citrated whole blood, samples were loaded into aPTT Citrate cuvettes to measure the blood clotting time.

Plasma equivalent aPTT clotting time was typically measured by mixing 16.2 µl of the sample with 1.8µl of 1.37M NaCl, followed by incubation at 37^{o}C for 10min. After mixing with 27µl of citrated whole blood, samples were loaded into aPTT Citrate cuvettes to measure the blood clotting time. Blood was purchased form Research Blood Components (RBC), and used within 10 days.

2.7. Bibliography

[1] Jana NR. Gram-scale synthesis of soluble, near-monodisperse gold nanorods and other anisotropic nanoparticles. Small 2005;1:875.

[2] Gou L, Murphy CJ. Fine-Tuning the Shape of Gold Nanorods. Chemistry of Materials 2005:3668

[3] Jana NR, Gearheart L, Murphy CJ. Seeding growth for size control of 5-40 nm diameter gold nanoparticles. Langmuir 2001;17:6782.

[4] Becker R, Liedberg B, Kall PO. CTAB promoted synthesis of Au nanorods - Temperature effects and stability considerations. Journal of Colloid and Interface Science 2010;343:25.

[5] Fu Y, Du Y, Yang P, Li J, Jiang L. Shape-controlled synthesis of highly monodisperse and small size gold nanoparticles. Science in China Series B-Chemistry 2007;50:494.

[6] Garg N, Scholl C, Mohanty A, Jin RC. The Role of Bromide Ions in Seeding Growth of Au Nanorods. Langmuir 2010;26:10271.

[7] Hubert F, Testard F, Spalla O. Cetyltrimethylammonium bromide silver bromide complex as the capping agent of gold nanorods. Langmuir 2008;24:9219.

[8] Jiang XC, Pileni MP. Gold nanorods: Influence of various parameters as seeds, solvent, surfactant on shape control. Colloids and Surfaces a-Physicochemical and Engineering Aspects 2007;295:228.

[9] Johnson CJ, Dujardin E, Davis SA, Murphy CJ, Mann S. Growth and form of gold nanorods prepared by seed-mediated, surfactant-directed synthesis. Journal of Materials Chemistry 2002;12:1765.

[10] Nikoocakht B, El-Sayed MA. Preparation and Growth Mechanism of Gold Nanorods (NRs) Using Seed-Mediated Growth Method. Chemistry of Materials 2003;15:1957

[11] Rayavarapu RG, Ungureanu C, Krystek P, van Leeuwen TG, Manohar S. Iodide Impurities in Hexadecyltrimethyl ammonium Bromide (CTAB) Products: Lot-Lot Variations and Influence on Gold Nanorod Synthesis. Langmuir 2010;26:5050.

[12] Smith DK, Korgel BA. The importance of the CTAB surfactant on the colloidal seed-mediated synthesis of gold nanorods. Langmuir 2008;24:644.

[13] Wu HY, Huang WL, Huang MH. Direct high-yield synthesis of high aspect ratio gold nanorods. Crystal Growth & Design 2007;7:831.

[14] Nikoobakht B, El-Sayed MA. Preparation and growth mechanism of gold nanorods (NRs) using seed-mediated growth method. Chemistry of Materials 2003;15:1957.

[15] Gao JX, Bender CM, Murphy CJ. Dependence of the gold nanorod aspect ratio on the nature of the directing surfactant in aqueous solution. Langmuir 2003;19:9065.

[16] Miranda OR, Dollahon NR, Ahmadi TS. Critical concentrations and role of ascorbic acid (vitamin C) in the crystallization of gold nanorods within hexadecyltrimethyl ammonium bromide (CTAB)/tetraoctyl ammonium bromide (TOAB) micelles. Crystal Growth & Design 2006;6:2747.

[17] Wijaya A, Hamad-Schifferli K. Ligand customization and DNA functionalization of gold nanorods via round-trip phase transfer ligand exchange. Langmuir 2008;24:9966.

[18] Kah JCY, Chen J, Zubieta A, Hamad-Schifferli K. Exploiting the protein corona around gold nanorods for loading and triggered release. ACS Nano 2012:Just Accepted.

[19] Hurst SJ, Lytton-Jean AKR, Mirkin CA. Maximizing DNA loading on a range of gold nanoparticle sizes. Analytical Chemistry 2006;78:8313.

[20] Zu Y, Gao Z. Facile and controllable loading of single-stranded DNA on gold nanoparticles. Anal Chem 2009;81:8523.

[21] Park S, Brown KA, Hamad-Schifferli K. Changes in oligonucleotide conformation on nanoparticle surfaces by modification with mercaptohexanol. Nano Letters 2004;4:1925.

[22] Demers LM, Mirkin CA, Mucic RC, Reynolds RA, Letsinger RL, Elghanian R, Viswanadham G. A fluorescence-based method for determining the surface coverage and hybridization efficiency of thiol-capped oligonucleotides bound to gold thin films and nanoparticles. Analytical Chemistry 2000;72:5535.

[23] Kira A, Kim H, Yasuda K. Contribution of Nanoscale Curvature to Number Density of Immobilized DNA on Gold Nanoparticles. Langmuir 2009;25:1285.

[24] Stakenborg T, Peeters S, Reekmans G, Laureyn W, Jans H, Borghs G, Imberechts H. Increasing the stability of DNA-functionalized gold nanoparticles using mercaptoalkanes. Journal of Nanoparticle Research 2008;10:143.

[25] Park S, Hamad-Schifferli K. Evaluation of hydrodynamic size and zeta-potential of surface-modified an nanoparticle-DNA conjugates via Ferguson analysis. Journal of Physical Chemistry C 2008;112:7611.

[26] Maus L, Spatz JP, Fiammengo R. Quantification and Reactivity of Functional Groups in the Ligand Shell of PEGylated Gold Nanoparticles via a Fluorescence-Based Assay. Langmuir 2009;25:7910.

[27] Lipka J, Semmler-Behnke M, Sperling RA, Wenk A, Takenaka S, Schleh C, Kissel T, Parak WJ, Kreyline WG. Biodistribution of PEG-modified gold nanoparticles following intratracheal instillation and intravenous injection. Biomaterials 2010;31:6574.

[28] Liu YL, Shipton MK, Ryan J, Kaufman ED, Franzen S, Feldheim DL. Synthesis, stability, and cellular internalization of gold nanoparticles containing mixed peptide-poly(ethylene glycol) monolayers. Analytical Chemistry 2007;79:2221.

[29] Cedervall T, Lynch I, Foy M, Berggård T, Donnelly SÄ, Cagney G, Linse S, Dawson KA. Detailed Identification of Plasma Proteins Adsorbed on Copolymer Nanoparticles. Angewandte Chemie International Edition 2007;46:5754.

3. Characterization of the covalently bound aptamer-NP conjugates

In order to use gold nanoparticles to control blood clotting is important to first understand the interactions that thrombin has with the TBA that is bound to NPs, and the interaction of TBA bound to particles with the complementary ssDNA (anti). In this chapter we are going to introduce thermodynamic and kinetic approaches to quantify the interactions of covalently bound biomolecules to gold nanoparticles with biomolecules in solution.

3.1. Introduction

The behavior of biomolecules that are bound to a surface is difficult to predict and control. "Wiring" biomolecules onto surfaces in a way that does not hinder the expected or designed behavior is incredibly challenging. DNA and proteins have a strong tendency to denature on surfaces due to the numerous non-covalent interactions between the biomolecule and the surface and the coating molecules, and denaturation is influenced by the surface material, curvature, charge, coating chemistry and crystallinity[1-5]. Due to the size of nanomaterials, the surface dominates their behavior. In addition, surfaces are not bare and inert, but can have charges or are coated with ligands, and these can also

influence denaturation. Finally, adsorption of other species to make a "corona" can obscure the desired behavior and function[6]. The interactions responsible for non-specific adsorption and denaturation are weak, non-covalent bonds between the side chains of the biomolecules and the nanoparticle surface atoms and/or coating ligands and are fluxional and numerous. This is a problem even for spherical gold nanoparticles (NPs), which are considered to be the most biocompatible nanoscale system due to their highly versatile surface chemistry and control in particle quality[7]. Many have shown that the interface of NPs with biomolecules significantly affect the structure and function of the attached biomolecule, sometimes even resulting in unexpectedly improved situations[8, 9]. What is now being established is that biomolecular surface functionality and nanomechanics are strongly intertwined. Transformations of biomolecules conjugated to planar or curved surfaces come with nanoscale rearrangements of the molecules themselves due to intermolecular forces[10]. Such interactions can cumulate and result in deviations from bulk solution behavior, introduce effects inherent to interfacial confinement such as radical changes in binding affinity, kinetics and yield [2, 3, 8, 11], or result in cooperative microscale mechanical work[8, 12, 13]. These issues affect not only nanobiomachines but also any sensing application, where molecules must be immobilized on a surface[6, 14].

3.2. Thermodynamic study of the binding of the aptamer-thrombin on the surface of a NP[1]

Biomolecular machines have inspired engineers for their ability to perform mechanical work or motion in a way that is rapid, specific error tolerant, and efficiencies that far surpasses artificial systems. Many have sought to exploit DNA-protein binding for use as biomolecular nanomachines. In particular, the TBA-thrombin interaction has been highly attractive due to its high specificity and reversibility[15, 16], enabling creation of machines that cycle through thrombin binding and displacement by addition of DNA strands. Also, DNA aptamers are simple, easy to handle, and can be made synthetically with chemical modifications.

However, for DNA machines to be eventually useful, they must be interfaced to an inorganic surface in order to harness the cumulative molecular-level changes and generate macroscopic motion. Typically this involves linking the biomolecules to nanoparticles

[1] Adapted with permission from de Puig H, Federici S, Baxamusa SH, Bergese P, Hamad-Schifferli K. Quantifying the Nanomachinery of the Nanoparticle-Biomolecule Interface. Small 2011;7. Copyright 2011 WILEY-VCH Verlag GmbH & Co. KGaA, Weinheim.

(NPs)[17-19], so that the biomolecules can be signalled to induce assembly and disassembly of the nanomaterials[17, 20, 21]. On larger scales, the conformational changes of the molecules can induce motion collectively to deflect a cantilever resulting in microscale motion[8, 12, 13, 22]. Control and understanding of these unique nano-to-microscale bridges would disclose unprecedented applications.

Unfortunately, systematic investigation of interface biomolecular nanomachinery has been lacking. In particular, most probes have not been quantitative, but instead phenomenological, probing only whether or not biomolecules adsorb, and have been explored primarily for biosensing[22]. Few studies on planar surfaces exist [8, 13, 23], but to the best of our knowledge, not much has been done for NPs.

Indeed, empirical observations are not sufficient to enable prediction of the behavior of biomolecules under these surface effects. For example, it is known that TBA binding to thrombin is influenced by the properties of the surface it is on as well as its molecular neighbors, which can give rise to intermolecular repulsions that hinder its ability to fold, or the ability of thrombin to get close enough to TBA to bind properly. However, these effects have been described only qualitatively, as there are no direct probes. A parameter describing these interface interactions would not only yield a deeper understanding of surface effects but also enable prediction of molecular behavior. Furthermore, it would

allow comparison between systems, which would be beneficial especially for surface chemistry modification strategies, which can drastically affect biomolecular behavior and are notorious for being difficult to control. Most investigations to date have not been quantitative, but instead phenomenological, probing only whether or not biomolecules adsorb. Unfortunately, these empirical observations cannot capture quantitative information, and therefore are insufficient. Thus, a diagram mapping the TBA binding regimes as a function of the relevant surface properties would greatly enhance the ability to construct interfaces to biomolecular motors. Therefore, the biological-inorganic interface is a critical and open challenge for taking biomolecular machines to a higher level. A few such studies on planar surfaces exist[8, 13, 23] but to the best of our knowledge, quantitative studies for NPs are few,[24] despite the fact that the surface dominates on the nanoscale.

Here we develop a new thermodynamic treatment for quantifying surface effects and apply it to study TBA nanomachinery on gold nanorods (NRs) when it interacts with thrombin. This thermodynamic treatment allows for quantitative description of the interface effects. We systematically probe how the interaction is influenced by TBA coverage, sequence, NR surface chemistry, and blocking proteins. We show that the term describing surface work is a relevant parameter for quantifying how the TBA is perturbed by interface effects, which is completely missed by phenomenological tests. This

treatment sets a promising framework to describe directed self-assembly of nanoparticles[17, 25], and could be useful to advance the state-of-the-art in organizing nanoscale 'building blocks' into supramolecular assemblies and materials, which to date definitively lag behind the advances in the synthesis and characterization of NPs and multifunctional macromolecules[26].

3.2.1. Analysis methods

The binding energetics of the NPs was analysed by using the Langmuir isotherm and the Van't Hoff equation, and the background of those equations is introduced in this chapter. In order to use the equations with colloids they were modified. Modifications on the equation will be introduced in the corresponding chapters.

3.2.1.1. Langmuir isotherm

In 1916, Irwin Langmuir introduced the Langmuir isotherm to describe the sorption of gases when in contact with planar surfaces[30]. The theory behind this theoretical analysis has been adapted for many conditions. In our case, we will derivate the equation for an aqueous system. This model assumes that one reaction is involved in the sorption process, and the distribution of the compounds between the two phases is controlled by an equilibrium constant. Other assumptions are that the adsorption reaction involves a

single reaction with a constant energy of adsorption; and that adsorption does not affect the availability (or the energy of adsorption) of the site next to the adsorbate.

If we consider the following equilibrium reaction:

$$S + A \rightarrow SA$$

Where S represents the solid surface (in our case the colloid with n surface sites) with nothing on it, A is the compound in the liquid phase (the adsorbate molecule), and SA is the solid phase with the compound A on it. Each A will occupy one surface site. [A] = equilibrium concentration of the compound A in the liquid or gaseous phase, and define the equilibrium constant k for the above reaction:

$$K = \frac{[SA]}{[S][A]} \qquad \text{(Eq. 3.1)}$$

If we define the total theoretical number of adsorbed A molecules, as n:

$$n = [SA] + [S] \qquad \text{(Eq. 3.2)}$$

If we combine the two previous equations:

$$n = [SA] + \frac{[SA]}{K[A]} \qquad \text{(Eq. 3.3)}$$

We can solve the equation for [SA] and let Θ = [SA]. This results in the Langmuir equation:

$$[SA] = \Theta = \frac{nK[A]}{1 + K[A]} \qquad \text{(Eq. 3.4)}$$

If K is known, one can predict the amount of the A compound adsorbed (Θ) for any concentration of A compound. The Langmuir equation is often rewritten as:

$$q_e = \frac{Qb[A]}{1 + b[A]} \qquad \text{(Eq. 3.5)}$$

Where q_e is the coverage of the adsorbate molecule on the particles, n is replaced by Q, the maximum number of A molecules that can theoretically be absorbed on the surface, and b is designated as the binding efficiency term. One can perform numerical fits of adsorption data in order to obtain values for Q and b to allow interpretation of the absorption behavior.

3.2.1.2. Van't Hoff equation

The Van't Hoff equation will be derived here for ideal solutions. It describes the temperature dependence of equilibrium, which is useful to know the enthalpy of the reaction. If we picture a two state equilibrium:

$$A \rightarrow B$$

Where by increasing the temperature, the NR aggregates disassemble, and we can see again the free NR. Then, at constant temperature and pressure, we can see that the condition for equilibrium is $\mu_A = \mu_B$. The equilibrium constant is:

$$K = \frac{[B]}{[A]} \qquad \text{(Eq. 3.6)}$$

The chemical potential of the component A diluted in an ideal solution is of the form:

$$\mu_A = \mu_A^0 + RTln[A] \qquad \text{(Eq. 3.7)}$$

Then, because the equilibrium condition states that:

$$\mu_A^0 + RTln[A] = \mu_B^0 + RTln[B] \qquad \text{(Eq. 3.8)}$$

Rearranging terms, and using the equilibrium constant:

$$ln\left(\frac{[B]}{[A]}\right) = \frac{\mu_A^0 - \mu_B^0}{RT} = \frac{-\Delta\mu}{RT} \qquad \text{(Eq. 3.9)}$$

Knowing that $\Delta\mu = \Delta\mathrm{H} - \mathrm{T}\Delta\mathrm{S}$

By taking into account that both the enthalpy and the entropy are temperature-independent:

$$\frac{\partial lnK}{\partial T} = -\frac{\partial}{\partial T}\left(\frac{\Delta\mu}{RT}\right) = -\frac{\partial}{\partial T}\left(\frac{\Delta H - T\Delta S}{RT}\right) = \frac{\Delta H}{RT^2} \qquad \text{(Eq. 3.10)}$$

Alternatively, we can derivate to 1/T to obtain the Van't Hoff equation:

$$\frac{\partial lnK}{\partial(1/T)} = -\frac{\Delta H}{R} \qquad \text{(Eq. 3.11)}$$

When, as stated above, the enthalpy is independent of temperature, one may integrate Van't Hoff equation in order to obtain:

$$ln\frac{K(T_2)}{K(T_1)} = -\frac{\Delta H}{R}\left(\frac{1}{T_2} - \frac{1}{T_1}\right) \qquad \text{(Eq. 3.12)}$$

Then, we can write this equation about the equilibrium constant calculated at room temperature, therefore, using a known factor as the binding constant:

$$K(T) = -K_{T_1} exp\left[\frac{\Delta H}{R}\left(\frac{1}{T_2} - \frac{1}{T_1}\right)\right] \qquad \text{(Eq. 3.13)}$$

We are going to use this approach to calculate the enthalpy of the NR-TBA binding in solution.

3.2.2. Theoretical

The interaction of thrombin with TBA on NRs results in NR self-assembly, as sketched in Figure 1. Because thrombin can bind specifically to TBA at both exosite I (green) and exosite II (purple), binding results in the aggregation of TBA decorated NRs (NR-TBA).

From a thermodynamic perspective this can be represented as the equilibrium between a free and an aggregated state, identified by state I and IV, respectively.

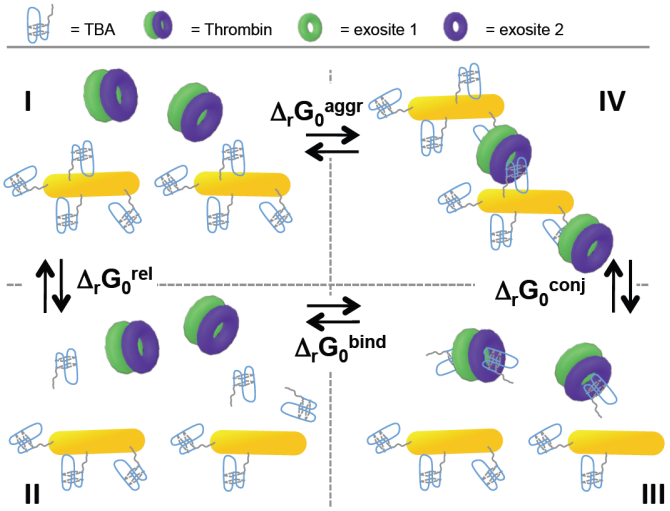

Figure 3-1: Thermodynamic cycle describing the assembly of NR-TBA in the presence of thrombin. Adapted with permission from de Puig H, Federici S, Baxamusa SH, Bergese P, Hamad-Schifferli K. Quantifying the Nanomachinery of the Nanoparticle-Biomolecule Interface. Small 2011;7. Copyright 2011 WILEY-VCH Verlag GmbH & Co. KGaA, Weinheim.

In order to describe this equilibrium system, we introduce the concept of unit block of aggregation, defined as an arbitrary fundamental complex from which the entire aggregate may be constructed by purely translational additions. For a three-dimensional NR-TBA-thrombin aggregate, several thrombin are bound to each NR-TBA. Thus, it is convenient to identify a NR-TBA bound to n thrombins as a unit block. Consequently, the equilibrium between state I and state IV can be described as the binding equilibrium of n thrombin molecules to a single NR-TBA, where the NR-TBA plays the role of a

receptor displaying n binding sites with invariant identical affinities (e.g. a n-valent uniform receptor[27]). Within this scheme, state IV represents the particular case of the smallest aggregate with $n = 1$ (Fig. 3-1).

Therefore, aggregation can be described in terms of the binding efficiency for one TBA, q[27] :

$$\theta = \frac{\Theta}{n} = \frac{K^{\sigma}[th]}{1 + K^{\sigma}[th]} \qquad \text{(Eq.3.14)}$$

where Θ is the binding efficiency of the NR-TBA receptor as a whole, K^{σ} is the equilibrium association constant of the TBA-thrombin binding confined at the NR surface and $[Th]$ is the equilibrium concentration of thrombin in solution.

TBA-thrombin binding is confined on the NR surface, so the overall Gibbs free energy of the reaction is comprised of both a chemical and a surface contribution. The chemical contribution is related to TBA-thrombin binding, whereas the surface contribution describes the work spent in accommodating the thrombin on the surface and for the concomitant nanoscale rearrangement of the bound and adjacent TBA molecules[8, 12]. The overall surface effect on aggregation can be understood if we construct a thermodynamic cycle that goes from the free state (state I) to the aggregated state (state IV) that is broken down into three hypothetical steps(Fig. 3-1). The first step describes

the release of TBA from the NR to the (bulk) solution (from I to II), the second step the TBA-thrombin recognition in solution (II to III), and the third the conjugation of the TBA-thrombin complexes to the NR (III to IV).

Each step is characterized by a standard molar Gibbs free energy: $\Delta_r G_0^{rel}$, $\Delta_r G_0^{bind}$ and $\Delta_r G_0^{conj}$, respectively. It follows that the standard molar Gibbs free energy of aggregation, $\Delta_r G_0^{agg}$, is given by

$$\Delta_r G_0^{agg} = \Delta_r G_0^{rel} + \Delta_r G_0^{bind} + \Delta_r G_0^{conj} \quad \text{(Eq.3.15)}$$

The surface work, W_σ, can be defined by gathering the non-recognition contributions, or $W_\sigma = \Delta_r G_0^{rel} + \Delta_r G_0^{conj}$. Thus $\Delta_r G_0^{agg}$ can be written as

$$\Delta_r G_0^{agg} = W_\sigma + \Delta_r G_0^{bind} \quad \text{(Eq.3.16)}$$

Equation (3.16) elucidates the energy of NR aggregation directed by molecular recognition confined on their surface. It is distinct from the energy of molecular recognition free in solution, and can be nonzero, as it is usually assumed. The difference lies in the surface work component, W_σ. W_σ can be either positive or negative, and therefore obscure or promote spontaneous aggregation. For example, a positive W_σ that exceeds $\Delta_r G_0^{bind}$ fully inhibits aggregation ($\Delta_r G_0^{agg} > 0$). The free energy of aggregation equals that of binding ($\Delta_r G_0^{agg} \cong \Delta_r G_0^{bind}$) only if $W_\sigma \cong 0$, which occurs when the release and conjugation energies are similar or very small. These two cases can be described as

"mild" surface conditions, possibly resulting from weak or negligible lateral interactions between the surface-confined species.

From the molecular machine standpoint, W^{σ} is cooperatively triggered by molecule-surface and molecule-molecule lateral interactions, such as hydration and thermal fluctuation forces, originating from nanoscale molecular motions fuelled by the interplay of surface molecular recognition, electrolyte surface density variation and "squeezing" between the NP surfaces[8, 28] .

Equation (3.16) can be used to evaluate W^{σ} from dose-response data for the binding variables θ and $[Th]$. If we express $\Delta_r G_0^{agg}$ as $-RT\ln K^{\sigma}$ and $\Delta_r G_0^{bind}$ as $-RT\ln K^{b}$, where K^{b} is the equilibrium constant of TBA-thrombin in solution, we can rearrange Equation (3.16) as

$$\frac{1}{K^{\sigma}} = \frac{1}{K^{b}}\exp\left(\frac{W^{\sigma}}{RT}\right) = K_d^{b}\exp\left(\frac{W^{\sigma}}{RT}\right) \qquad \text{(Eq.3.17)}$$

where K_d^{b} is the TBA-thrombin dissociation constant in solution. By substituting Equation (3.17) into Equation (3.14) we obtain an expression that can quantify W^{σ} for different TBA coverage of NRs, TBA sequence, NR surface chemistry, and blocking proteins:

$$\theta = \frac{1}{\frac{K_d^b}{[th]}\exp\left(\frac{W^\sigma}{RT}\right)+1} \quad \text{(Eq.3.18)}$$

Equation (3.18) can be seen as a Langmuir equation that specifically describes self-assembly of NPs directed by molecular interactions. It is related to the Stern equation (proposed in 1924 for describing electrolyte adsorption at a charged surface) and the modified Langmuir by Fowler and Guggenheim (implemented in 1952 to take into account lateral interactions in adsorption of gases on solids)[29]. Here we ascribe a physical meaning to the modification via the thermodynamic cycle, i.e. by describing the energy of aggregation as a sum of surface and molecular recognition contributions. Note that when $W^\sigma = 0$, Equation 3.18 reduces to the Langmuir isotherm, which does not account for intermolecular interactions.

3.2.3. Results and discussion

3.2.3.1. Synthesis and characterization of TBA decorated NRs

We deployed this thermodynamic framework on NR-TBA with different surface treatments (Figure 3-2a). NRs were monodisperse in size, as confirmed by TEM (Figure 3-2b), with a length of 35 ± 5 nm and width of 10 ± 1 nm (aspect ratio = 3.6 ± 0.7). The TBA surface density on the NRs was varied systematically with the meaning of covering peculiar conditions. TBAs with a long spacer or not were used, namely TBA linked to a

sequence of 15 thymines terminated with a SH moiety (SH-T_{15}-TBA) and straight SH-modified TBA (SH-TBA). TBA surface density was varied between low and high, $(5.6 \pm 1.1) \cdot 10^{12}$ TBA/cm^2 *vs.* $(12.3 \pm 2.5) \cdot x10^{12}$ TBA/cm^2. The NR surface chemistries were also varied. NR-TBAs were "backfilled" with ligands of thiolated polyethylene glycol (PEG), which are used extensively as a surface coating ligand for NPs to prevent fouling and non-specific adsorption[30, 31]. In addition, we probed the effect of "blocking" the surface with human serum albumin (HSA, 0.3%), protein which is widely used to prevent aggregation and non-specific adsorption for both NP and planar surfaces (For details on protocols, see Chapter 2: Materials and Methods).

Gel electrophoresis was used to probe the effect of the different surface conditions on the NRs (Figure 3-2c). Lane 1: NRs conjugated to T_{15}-TBA with high coverage exposed to HSA, Lane 2: NRs conjugated to TBA, Lane 3: NRs conjugated to T_{15}-TBA with high coverage, Lane 4: NRs conjugated to T_{15}-TBA with low coverage, Lane 5: MHA coated NRs before conjugation to DNA. Lane 6: NRs conjugated to T_{15}-TBA with high coverage, Lane 7: NRs conjugated to T_{15}-TBA with high coverage and exposed to mPEG (MW 5000) at 5:1 mPEG:TBA, Lane 8: NRs conjugated to T_{15}-TBA with high coverage, Lane 9: NRs conjugated to T_{15}-TBA with high coverage and exposed to mPEG (MW 5000) at 0.5:1 mPEG:TBA.

Conjugation of the NRs to the SH-T_{15}-TBA and to SH-TBA was confirmed by a shift to lower mobility. Increasing the DNA:NR incubation ratio resulted in a higher mobility shift, confirming the higher coverage of the DNA on the NR surface, which was further confirmed by chemical displacement methods used to quantify the DNA on the NR surface (see Chapter 2: Materials and Methods)[32, 33]. Incubation of the NR-TBA (SH-T_{15}-TBA, high coverage) with thiolated mPEG (MW = 5000) resulted in further shifts to lower mobility, indicating that some of the neutral mPEG was put onto the surface of the NR-TBA. Finally, incubating the NR-TBA with HSA resulted in a shift to lower mobility. This is due to an increase in NR-TBA size upon adsorption of the HSA and confirms successful HSA blocking.

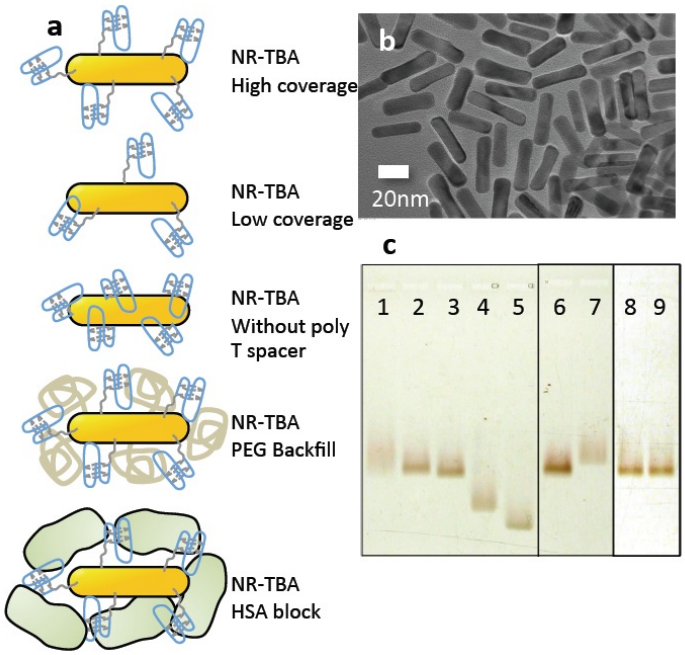

Figure 3-2: Samples probed. Adapted with permission from de Puig H, Federici S, Baxamusa SH, Bergese P, Hamad-Schifferli K. Quantifying the Nanomachinery of the Nanoparticle-Biomolecule Interface. Small 2011;7. Copyright 2011 WILEY-VCH Verlag GmbH & Co. KGaA, Weinheim.

3.2.3.2. Probing thrombin directed self-assembly

One of the most popular TBA is a single-stranded DNA 15mer 5'-GGTTGGTGTGGTTGG-3' [34]. It folds into a chair structure stabilized by two G-quartets (Fig. 3-1)[35] .When in this conformation, TBA binds strongly to thrombin at either exosite I or exosite II in a highly specific manner. Binding occurs in a way that is not only strong, with a binding constant K_D that ranges from 1-100's of nM. Because thrombin can bind to two TBAs[35], NR-TBA will self-assemble upon binding to thrombin (Fig. 3-1). This results in a red shift and broadening of the surface plasmon

resonance (SPR) peak. Figure 3-3 shows the absorption spectrum of NR functionalized with SH-T_{15}-TBA incubated with 121 nM concentration of thrombin as a function of time. The longitudinal SPR red shifts and broadens with time, suggesting aggregation.

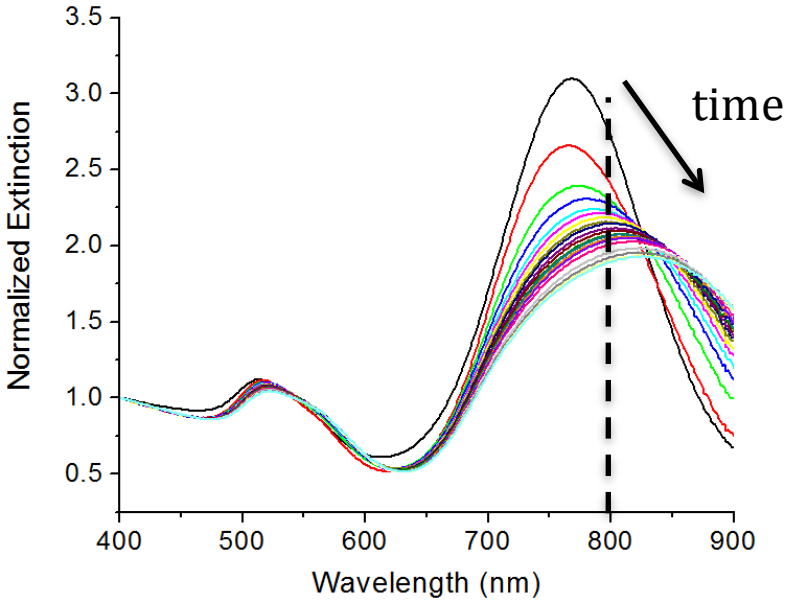

Figure 3-3: Change in absorption spectra of NR-T_{15}-TBA high coverage as a function of time upon incubation with 121 nM of thrombin (arrow indicates increasing time). Adapted with permission from de Puig H, Federici S, Baxamusa SH, Bergese P, Hamad-Schifferli K. Quantifying the Nanomachinery of the Nanoparticle-Biomolecule Interface. Small 2011;7. Copyright 2011 WILEY-VCH Verlag GmbH & Co. KGaA, Weinheim.

To quantify aggregation, the ratio of extinctions at 400nm and 800nm (A_{400}/A_{800}) is plotted, which increases as a function of time in the presence of thrombin (Figure 3-4). A_{400}/A_{800} time courses are collected for several thrombin concentrations (0-121 nM, Fig. 3-4).

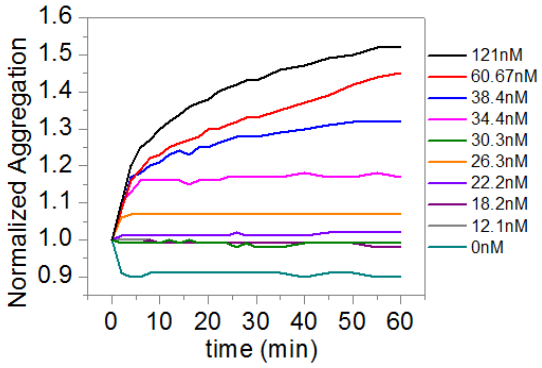

Figure 3-4: A400/A800 as a function of time for NR-T_{15}-TBA high coverage for different thrombin concentrations. Adapted with permission from de Puig H, Federici S, Baxamusa SH, Bergese P, Hamad-Schifferli K. Quantifying the Nanomachinery of the Nanoparticle-Biomolecule Interface. Small 2011;7. Copyright 2011 WILEY-VCH Verlag GmbH & Co. KGaA, Weinheim.

The A_{400}/A_{800} endpoint at t = 1 hr is used to define when equilibrium is attained, and is plotted as a function of thrombin concentration (Fig. 3-5) to construct an aggregation dose-response curve, or isotherms. The aggregation isotherm exhibits Langmuir-like behavior, where after a threshold it increases with increasing thrombin concentration, eventually saturating.

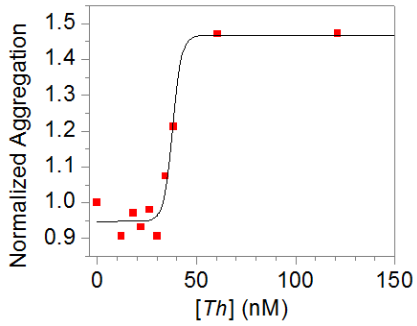

Figure 3-5: Aggregation isotherm for NR-T_{15}-TBA high coverage. Adapted with permission from de Puig H, Federici S, Baxamusa SH, Bergese P, Hamad-Schifferli K. Quantifying the Nanomachinery of the

In order to prove that the self-assembly is due to the specific interaction between thrombin and the TBA on the NR, we performed a competitive inhibition. Already formed NR-TBA-thrombin aggregates were incubated with a DNA strand complementary to the TBA. Because TBA must maintain a G-quartet structure to bind to thrombin, binding to a complement will not permit it to self-fold and bind to thrombin. Upon addition of 10 μl of 1 mM of the complement to the 38.4nM thrombin-aggregated sample (Fig. 3-6), A_{400}/A_{800} decreases and returns to its original value, indicating that the aggregate was disrupted and thus confirming that self-assembly is due to the specific TBA-thrombin recognition.

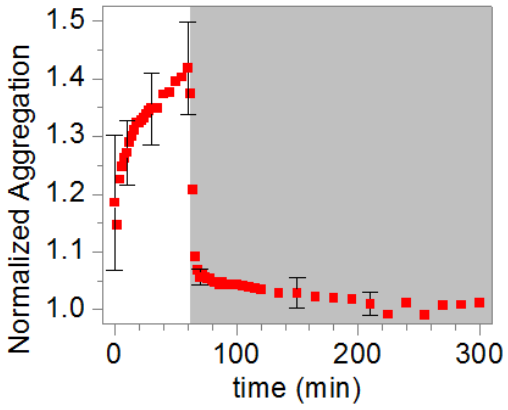

Figure 3-6: A400/A800 as a function of time upon incubation with thrombin (t = 0 min) and complementary DNA sequence (gray area, 60 min). Adapted with permission from de Puig H, Federici S, Baxamusa SH, Bergese P, Hamad-Schifferli K. Quantifying the Nanomachinery of the Nanoparticle-Biomolecule Interface. Small 2011;7. Copyright 2011 WILEY-VCH Verlag GmbH & Co. KGaA, Weinheim.

In addition, disruption (melting) of the aggregate by heat was also probed. Already formed aggregates with a thrombin concentration of 121 nM were exposed to a heating-cooling cycle and monitored by tracking A_{400}/A_{800} (Fig. 3-7). As the temperature increased, A_{400}/A_{800} decreased with a sigmoidal drop centered at ~42 °C, suggesting that the aggregate was disrupted by denaturation of the TBA or the thrombin. Decreasing the temperature from 75 °C down to 25 °C did not result in a change in A_{400}/A_{800}, suggesting that the aggregate could not form again. This could be due to the fact that the thrombin was irreversibly denatured [36].

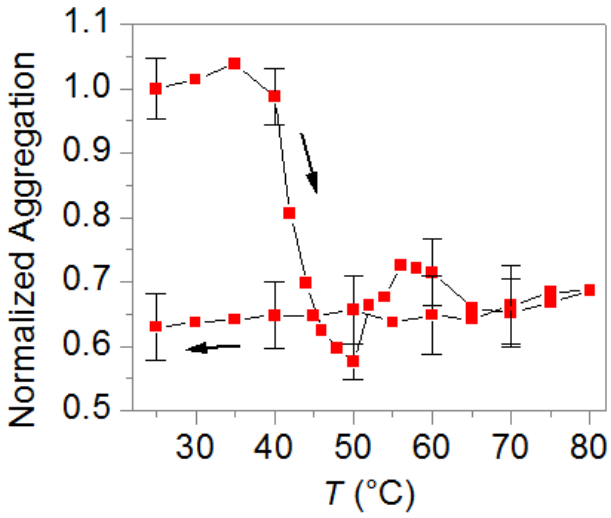

Figure 3-7: A400/A800 of already formed NR-T_{15}-TBA -thrombin aggregates as a function of changing the temperature from 25ºC to 80ºC and back down to 25ºC (arrows indicate direction). Adapted with permission from de Puig H, Federici S, Baxamusa SH, Bergese P, Hamad-Schifferli K. Quantifying the Nanomachinery of the Nanoparticle-Biomolecule Interface. Small 2011;7. Copyright 2011 WILEY-VCH Verlag GmbH & Co. KGaA, Weinheim.

These experiments further confirm that the aggregation is due to the specific interaction of thrombin with the TBA on the NR surface.

3.2.3.3. Nanomachinery of TBA on NRs

Aggregation isotherms were analyzed using the modified Langmuir equation (Eq. 3.18). assuming that A_{400}/A_{800} was a measure of the number of aggregated NR-TBA[37], and thus of the TBA-thrombin surface binding efficiency θ. Data points from three experimental replicates were fitted by a best-fit procedure to obtain θ and W_s, with the associated errors evaluated.

The first step to exploit Equation (3.18) to fit the experimental curves consists in expressing the binding efficiency, θ, in terms of the signal intensity, I. Since θ and I are proportional, we can set $\theta = I \cdot \beta^{1}$, in which β is the proportional constant. We obtain

$$I = \frac{\beta}{\frac{K_d^b}{[th]}\exp\left(\frac{W_s}{RT}\right)+1} \qquad \text{(Eq.3.19)}$$

However, this Langmuir equation fails to fit the experimental data and it needs to be further optimized. By using the mathematical principle of translation, we applied a rigid shift of the Equation (3.19) with respect to the x and y axes in order to take into account the onset of aggregation. These shifts were subtracted from the equilibrium concentration and from the signal intensity to give the following equation

$$I - I_T = \frac{\beta}{\frac{K_d^b}{[th]-[th_T]}\exp\left(\frac{W_s}{RT}\right)+1} \quad \text{(Eq.3.20)}$$

In which I_T and Th_T refer to the values of signal intensity and equilibrium concentration at the threshold. K_d^b is the TBA-thrombin dissociation constant in homogeneous solution fixed at 3.3 ± 1.1 $\times 10^{-7}$ M[38]. b and W^s are the free parameters of the fitting.

Data are fitted using Equation (3.20) over three repetitions of the same experiments and the errors on the free parameters are assigned as a result of the fitting algorithm (with 95% confidence bounds).

Finally, we described the NR aggregation process through a single binding of NR confined TBA and thrombin (Equation 3.15). Since aggregation was conducted in excess of thrombin with respect to NR concentration (about 6 nM), we may assume in first approximation that the concentration of thrombin not involved in that binding event (i.e. formally in solution), Th, does not change significantly before and after aggregation ($[Th] \equiv Th$).

Aggregation as a function of thrombin concentration and their fits are all reported (Fig. 3-8a-3-8e). The fits are also compared in Figure 3-8d. High and low coverage NR-TBA display isotherms that differ in two ways (Figure 3-8a, 3-8b, and 3-8f). First, the onset of aggregation (Th_T) for the high coverage sample is at ~30 nM thrombin, while it occurs at

~15 nM thrombin for the low coverage. Also, the rise in the curve is steeper for the high coverage NR-T_{15}-TBA. This indicates that changing TBA surface coverage affects the binding of thrombin to NR-T_{15}-TBA. Treating the high coverage NR-TBA surface with mild PEG conditions also affected the aggregation isotherm, that displays the steepest curve rise and highest Th_T at ~35 nM thrombin (Fig. 3-8c and 3-8f). On the contrary, no isotherm was registered for NR-T_{15}-TBA exposed to stronger PEGylation (Fig 3-8g), showing that aggregation varies with surface modification conditions. NRs coated with TBA lacking T_{15} exhibited no aggregation (Figure 3-8e), suggesting that TBA on the NR was unable to bind thrombin. TBA coverage was $28.6 \pm 5.8 \times 10^{12}$ TBA cm^{-2} as determined by chemical displacement, which exceeds a monolayer and is likely due to formation of intermolecular G-quartets[39] that would disrupt the ability to bind thrombin. Incubation of high coverage NR-T_{15}-TBA with HSA prevented thrombin binding and thus aggregation, as indicated by negligible change in A_{400}/A_{800} (Figure 3-8f). This shows that the HSA was able to block thrombin from the TBA on the NR surface.

Figure 3-8 shows the modified Langmuir aggregation isotherms for a) NR-T_{15}-TBA high coverage, b) NR-T_{15}-TBA low coverage, c) NR-T_{15}-TBA mPEG backfill 0.5:1 mPEG:TBA, d) fits for plots a-c , e) NR-TBA without a poly T spacer (the dashed line

is the average value), f) NR-T_{15}-TBA HSA block (the dashed line is the average value), g) NR- T_{15}-TBA high coverage mPEG backfill 5:1 mPEG:TBA.

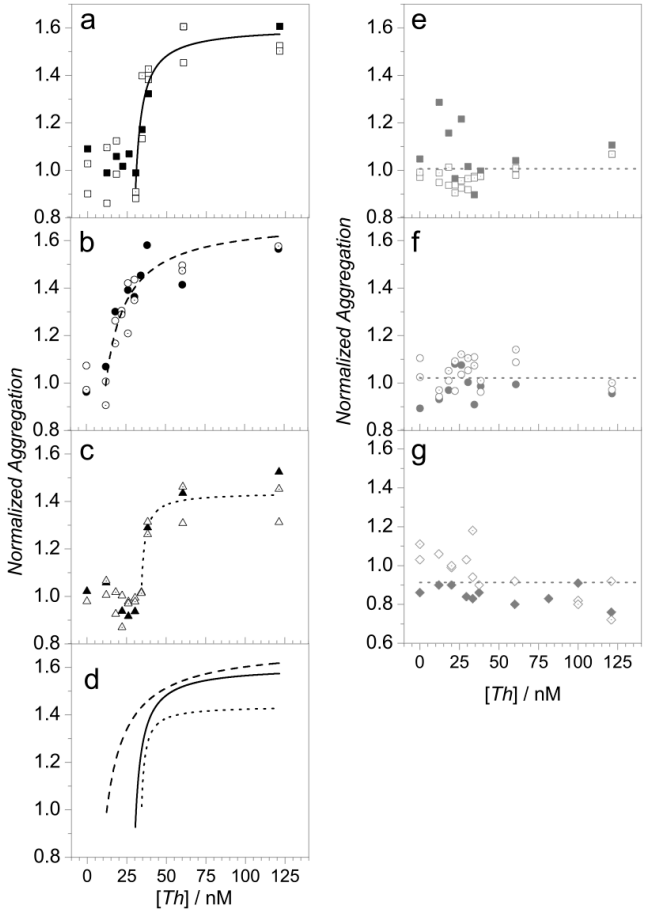

Figure 3-8: Modified Langmuir aggregation isotherms for a) NR-T_{15}-TBA high coverage, b) NR-T_{15}-TBA low coverage, c) NR-T_{15}-TBA mPEG backfill 0.5:1 mPEG:TBA, d) fits for plots a-c , e) NR-TBA without poly T spacer (the dashed line is the average value), f) NR-T_{15}-TBA HSA block (the dashed line is the average value), g) NR- T_{15}-TBA high coverage mPEG backfill 5:1 mPEG:TBA. Reprinted with permission from de Puig H, Federici S, Baxamusa SH, Bergese P, Hamad-Schifferli K. Quantifying the Nanomachinery of the Nanoparticle-Biomolecule Interface. Small 2011;7. Copyright 2011 WILEY-VCH Verlag GmbH & Co. KGaA, Weinheim.

The data analysis can also be used to map how W_σ changes as a function of θ and Th_T for different TBA coverages and surface chemistry (Fig. 3-9). First, the values for the W_σ are all negative and on the order magnitude of -10 kJ/mol, indicating that the surface work significantly contributes with TBA-thrombin binding in promoting aggregation. In particular, since the binding free energy of thrombin-TBA in solution is $\Delta_r G_0^{bind} \sim -37$ kJ/mol[38] , we can calculate by Eq. (3.20) that W_σ nearly comprises 30% of the aggregation energy, $\Delta_r G_0^{agg}$., that results that results ~ -50 kJ mol^{-1}, comes from W_σ. This shows that aggregation is not due solely to TBA-thrombin binding, as it is predominantly assumed.

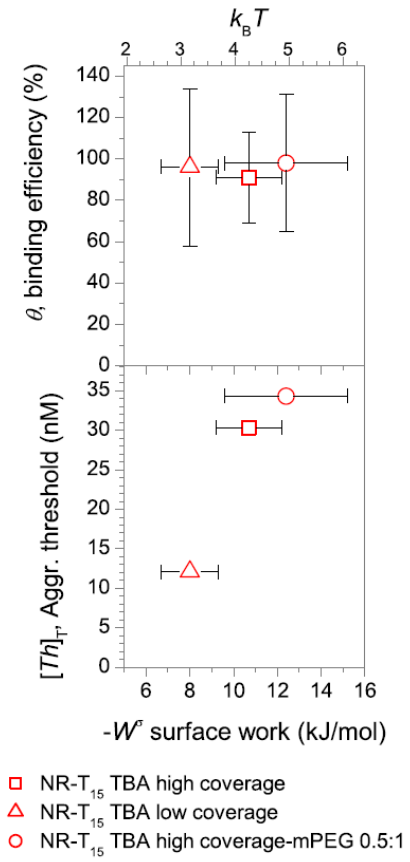

Figure 3-9: a) ϑ vs. -W^σ for NR-T_{15}-TBA high coverage (square), NR-T_{15}-TBA low coverage (triangle), and NR-T_{15}-TBA -PEG backfill 0.5:1 (circle), b) ThT vs. - W^σ for NR-T_{15}-TBA high coverage (square), NR-T_{15}-TBA low coverage (triangle), and NR- T_{15}-TBA -mPEG backfill. Adapted with permission from de Puig H, Federici S, Baxamusa SH, Bergese P, Hamad-Schifferli K. Quantifying the Nanomachinery of the Nanoparticle-Biomolecule Interface. Small 2011;7. Copyright 2011 WILEY-VCH Verlag GmbH & Co. KGaA, Weinheim.

From the same calculation we also learn that the $\Delta_r G_0^{agg}$ value is on the order of 50 kJ/mol, corresponding to about 20 $k_B T$. This confirms that NR-TBA aggregation is long-lived, on the time scale of hours or days[28]. On the other hand, W^σ values in $k_B T$ units are (3.2 ± 0.5) $k_B T$, (4.3 ± 0.6) $k_B T$ and (5.0 ± 1.1) $k_B T$ for low and high coverage NR-TBA

and the PEG backfilled NR-TBA, respectively. These values are high enough to say that the in-plane intermolecular interactions underpinning W° are significantly larger than thermal vibrational energy $k_{\mathrm{B}}T$ (that on the other hand individuates the order of magnitude of the measurement uncertainties). This suggest that the in-plane interaction lifetime is $<$ 1 second[28] and in turn that the timescale of TBA motions is well below the timescale of NR-TBA aggregation.

Obtained θ for NR-TBA high and low coverage and PEG-backfill are identical within the experimental errors and close to 100% (Fig. 3-9). This means that for all samples aggregation was nearly complete. However, W° values differ, where low coverage has the lowest absolute value (-8.0± 1.3) kJ/mol, higher coverage has a higher value (-10.7 ± 1.5) kJ/mol, and the addition of PEG to the surface results in the highest value (-12.4 ± 2.8) kJ/mol. Evidently, increasing the surface density of the TBA on the NR increases its absolute W°. This could be due to the fact that for aggregation to occur, more W° needs to be done to accommodate the thrombin on crowded surface. Furthermore, introduction of small amounts of PEG, which is a cumbersome molecule, increases W°.

This difference in energy is taken from thrombin in solution, which can be shown from values of the threshold thrombin concentration for the different samples, Th_{T} (i.e. the thrombin chemical potential) (Fig. 3-9). Th_{T} required for the onset of aggregation

increases with increasing $|W_\circ|$, showing that samples that require lower $|W_\circ|$ and thus with smaller interface effects do not need as much thrombin to aggregate.

These results show that TBA behavior can vary with varying coverage on the NR or NR surface chemistry, and in a way that does not affect its aggregation efficiency θ. Conversely, this means that simply probing NR aggregation yields incomplete information on biomolecular behavior on the NR surface. Surprisingly, in view of $W_\circ$ data and Equation (3.20) the NR- T_{15}-TBA sample with mild PEGylation has the highest energy of aggregation, $\Delta_r G_0{}^{agg}$, and thus forms the most stable aggregate. Even though the surface treatment does not yield a detectable amount of PEG on the NR by electrophoresis, its $W_\circ$ is distinct from high coverage NR-T_{15}-TBA. This shows that mild surface treatments that are difficult to detect can still result in significant $W_\circ$ changes. This is in striking contrast with the common understanding that PEG backfilling is inert and prevents fouling and non-specific adsorption of other species and highlights the variability and complexity of the interface.

$W_\circ$ can be expressed in units of mN/m in order to compare it to $W_\circ$ of biomolecular transformations confined to planar surfaces and evaluated by microcantilever (MC) beams, including DNA hybridization and other molecular recognition interactions[22] as well as pH and electrolyte driven conformational changes[8, 13, 23]. To the best of our

knowledge, this is the first time analogous studies are reported for NPs. W_o from the MC experiments ranges from 1 to 10's of mN/m, where one study of aptamer-protein interactions reports a W_o = 9.6 mN/M[40]. By dividing the W_o we obtained for low and high coverage NR-TBA for the respective TBA surface coverage (see [8] for a justification of this calculation) we obtain W_o = (-0.74 ± 0.26) mN/m and W_o = (-2.18 ± 0.76) mN/m, respectively, which are consistent with the reported range of values in the literature. This suggests that W_o involved in transformations of NP conjugated biomolecules is comparable to W_o of biomolecules conjugated to planar surfaces. By some more arithmetic, we may note that an average coverage of the NRs of 10^{13} TBA per cm^2 means that 1 TBA molecule occupies about 10 nm^2, that corresponds to a circle of about 3.5 nm diameter. By taking into account that a TBA molecule in the binding chair conformation has an average size of 2.5 nm we conclude that the average distance between two TBAs is 1 nm, which multiplied to W_o gives a force in the order of units of pN. Remarkably, these data are fairly consistent with unfolding forces from single-molecule experiments[41].

We observed that by heating the NR aggregates solution, the NR aggregates disassemble. We can use this data in order to calculate the enthalpy of the TBA-thombin induced assembly of the NRs, by using the Van't Hoff equation[47].

$$K(T) = -K_{T_1} exp\left[\frac{\Delta H}{R}\left(\frac{1}{T_2} - \frac{1}{T_1}\right)\right] \quad \text{(Eq.3.21)}$$

By following the approach from literature[47], we can use a thermodynamic analysis to study the melting curve of thrombin-TBA-NR aggregates. In order to do that, the aggregates were heated and the absorbance of the particles was recorded. In order to analyze the behavior of the particles we worked with a model that could take into account that more than one particle was binding in the aggregates. In the Mirkin/Schatz group[47], they study the assembly of NRs after the addition of DNA strands. In their case, it is a short DNA sequence that serves as a binder between two different nanoparticles, therefore having the same function as the thrombin(th) has in our project.

Assuming that there are many particles in every aggregate, and that each pair may be linked by more than one thrombin, we may divide the disruption of the aggregates in different steps in which:

$$Agr^m \rightleftharpoons Agr^{m-1} + th$$

$$Agr^{m-1} \rightleftharpoons Agr^{m-2} + th$$

$$Agr^2 \rightleftharpoons Agr + th$$

$$Agr \rightleftharpoons NR + th$$

Then, we may as well define the fraction of NRs in an assembled state as:

$$f = \frac{D_0}{D_T} = \frac{D_0}{\sum D_i} = \frac{1}{1 + {}^{1}/_{K}} \quad \text{(Eq.3.22)}$$

Where D_T is the total concentration of aggregate, and D_0 represents the concentration of free nanoparticles after the unbinding process is complete. The overall equilibrium constant K is related to the partial equilibrium constants K_i by:

$$\frac{1}{K} = \frac{th}{K_1}\left(1 + \frac{th}{K_2} + \frac{th^2}{K_2K_3} + \cdots + \frac{th^{n-1}}{K_2K_3K_4 \ldots K_n}\right) \sim \frac{th^n}{K_1K_2K_3 \ldots K_n} \quad \text{(Eq.3.23)}$$

The number n represents the total number of thrombin bound per particle, and by using the Van't Hoff formula for Ki:

$$K_i = [th]\, exp\left[\frac{\Delta H_i}{R}\left(\frac{1}{T} - \frac{1}{T_{m,i}}\right)\right] \quad \text{(Eq.3.24)}$$

Where ΔH_i is the enthalpy of step i, which is temperature independent; and $T_{m,i}$ is the melting temperature at i concentration of thrombin. By substituting equation 3.24 into 3.23 and using 3.22; we obtain a relation for the melting curve:

$$f = \frac{1}{1 + exp\left[\frac{\Delta H_T}{R}\left(\frac{1}{T} - \frac{1}{T_m}\right)\right]} \quad \text{(Eq.3.25)}$$

By fitting this equation to the obtained melting curve:

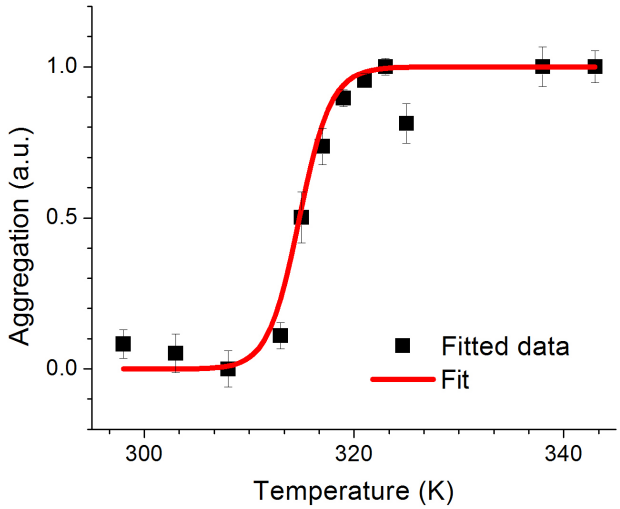

Figure 3-10: Melting profile of the NR-thrombin conjugates and fitted model

By fitting the obtained data from the experiments following the previous approach, we were able to find a ΔH of 547.7 kJ/mol. We can compare this value with other enthalpy results[47] and observe that it is in the order of the values that would be expected for NR conjugates. Specifically, in Jin et al.'s article which studies the binding of nanoparticles by the action of complementary DNA strands, the value of ΔH obtained is 1326 kJ/mol; one must note that in their model, the number of interaction between particles is much higher than in the case of thrombin binding; as DNA is much smaller than thrombin, and therefore there is the possibility for a higher number of interactions, and also one must note that the DNA-DNA interaction is in general-stronger than the thrombin-TBA interaction.

3.2.4. Conclusions

We have introduced a thermodynamic analysis that can quantify the interactions of TBA on NR surfaces with thrombin. The model is completely general and relies on the critical step of separating TBA-thrombin recognition from surface effects due to confinement of the recognition event within NR surfaces. In particular, the model introduces the efficiency of aggregation, θ, and the surface work of aggregation, W_{σ}, this latter containing information about the nanoscale motion of how the molecules must accommodate each other on the surface or binding to its target. In this way, it enables a quantitative understanding of interfacial nanoscale phenomena "fuelled" by thrombin directed aggregation.

Obtained values of W_{σ} are on order magnitude of -10 kJ/mol. They comprise about 30% of the overall aggregation energy and therefore indicate that the surface work significantly participates with TBA-thrombin binding to aggregation (that is, they pose a strong *caveat* on the common assumption that aggregation is exclusively directed by the molecular recognition event). They also suggest that the in-plane molecular forces that trigger W_{σ} are on the order of magnitude of few pN and have a lifetime well below 1 second, albeit the TBA-NR aggregation is stable on the day timescale. W_{σ} can be used to compare experiments between flat surfaces (e.g. microcantilevers) and gold nanoparticles;

and since it can be quantified, it can also be used to compare results between research groups, which would greatly help in understanding the nano-bio interface.

W_o is a function of molecular density on the NR surface and surface chemistry and turned to be crucial in discriminating molecular directed self-assembly processes that looked have similar θ. This would have been missed by phenomenological tests, which probe only whether or not aggregation occurs, and *de facto* giving a qualitative estimation of θ. $W_o$contains also important information on how the NP-immobilized biomolecule function is affected by crowding or the presence of other molecules. Using the model we were able to show that while strong PEG treatments result in the expected behavior of no aggregation, mild PEG treatments can actually result in a larger value of W_o and thus stronger tendency to aggregate. These PEGylations are mild enough that gel electrophoresis cannot detect any difference from non-PEGylated NR-TBA. These results show that PEG treatments do not always yield NRs inert, and also highlight the complexity and variability of the nano-bio interface.

In summary, these results indicate that our approach could help a basic understanding of surface confined biomolecular transformations, as it extends to nanoparticles quantitative information that could previously be determined for only planar surfaces and it is broadly applicable to probe the behavior of any receptor-ligand binding event, as well as the

effect of other parameters, such as surface curvature and surface material composition. W_a can be used to compare experiments between flat surfaces (microcantilevers) and gold nanoparticles; and since it can be quantified, it can also be used to compare results between research groups, which would greatly help in understanding the nano-bio interface.

3.3. Kinetics of biomolecule-induced nanoparticle assembly

The assembly of gold nanoparticles to form larger structures leads to a change in their optical properties[42-44], which can be used in order to detect their target agents. The assembly of nanoparticles to form larger structures has interesting applications in many physics, chemistry and biology processes. The assembly of DNA functionalized nanoparticles to form larger aggregates after the addition of complementary DNA sequences has been studied by different authors[45-47]. This approach is important as well in sensing applications of proteins, where NPs can be conjugated to aptamers and aggregate when the target protein is present in the solution [45, 48, 49]. In such cases, the aptamers binds to the target protein; therefore, if the aptamer is interfaced to an inorganic surface, it can report a signal that represents the aptamer-target interaction. An example of this is the TBA-thrombin recognition.

Although the thrombin-TBA recognition has been studied in solution, a few studies exist on its binding on surfaces, where the interactions between neighbouring DNA sequences and between the surface and the DNA play an important role in protein binding at the interface. The distribution of the DNA on the surfaces can vary with the curvature of the particles [10, 50, 51]. Nanoparticles have charges or can be coated with ligands that affect the interactions between the biomolecules at the interface[1, 4, 7, 9]. Also, the

particles' surface behavior can be modified by the introduction of other species to create a corona around the nanoparticle[7]. All these intermolecular forces on the surfaces can result in transformations of the attached biomolecule's structure.

In order to make nanoparticles useful for biosensing applications, a study on the kinetic of the assembly process is necessary. In this chapter we study the mechanism of gold nanoparticle assembly and observe the importance that surface chemistry plays in it.

As we already introduced in the previous chapter, the interaction of thrombin with TBA on NRs results in NR self-assembly (Fig. 3-11). Binding results in aggregation of TBA decorated NRs, as thrombin is able to bind specifically to TBA at both exosite I (green) and exosite II (purple).

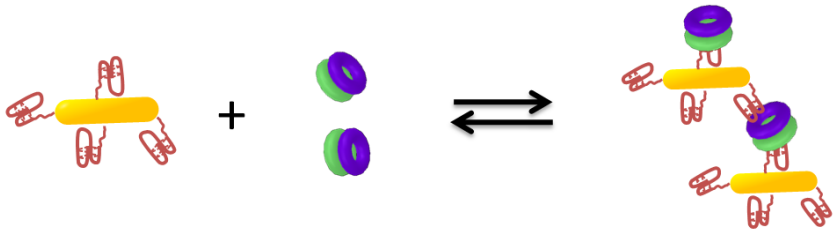

Figure 3-11. Nanorod assembly kinetics scheme

In order to describe and understand the mechanism of the NR aggregation, we can divide the process into two different reactions that are involved during the aggregation. In the first one (Fig. 3-12), we imagine the attachment of thrombin to single NRs in order to

form unit blocks of aggregation, that we can define as an arbitrary fundamental complex from which the entire aggregate may be constructed by purely translational units, we identify a NR-TBA bound to *n* thrombins as a unit block of aggregation. By assuming that the kinetic constants do not change with the number of thrombins attached to the unit block of aggregation we can picture the following reaction:

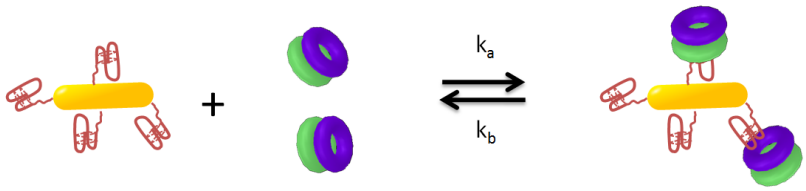

Figure 3-12: Formation of the unit blocks of aggregation scheme

Where k_a and k_b are the kinetic constants that rule the attachment of thrombin to nanorods in order to form unit blocks of aggregation. After the unit blocks of aggregation are formed, we can model their attachment in terms of subsequent unit block additions to form the aggregate, as sketched in figure 3-13, where k_c and k_d are the kinetic constants that rule the aggregation process of the system.

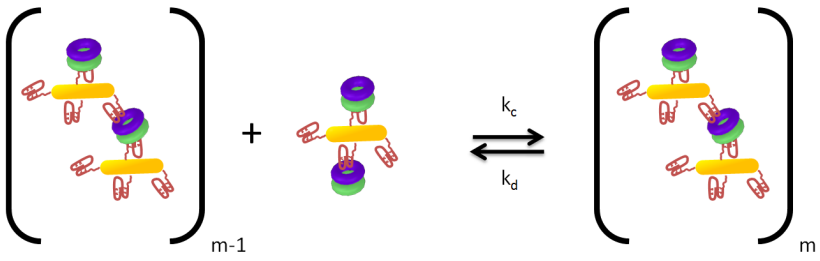

Figure 3-13: Subsequent monomer addition scheme

The first approach we should take into account is that the formation of nanorod-thrombin unit blocks is very fast compared to the formation of the aggregates (Agr); therefore, the rate-determining step would be the formation of the aggregates. We can assume that the concentration of thrombin in solution is high related to the concentration of NRs so we can consider it constant. Also, we may assume that after every NR addition in the aggregate, the kinetics of the system do not change:

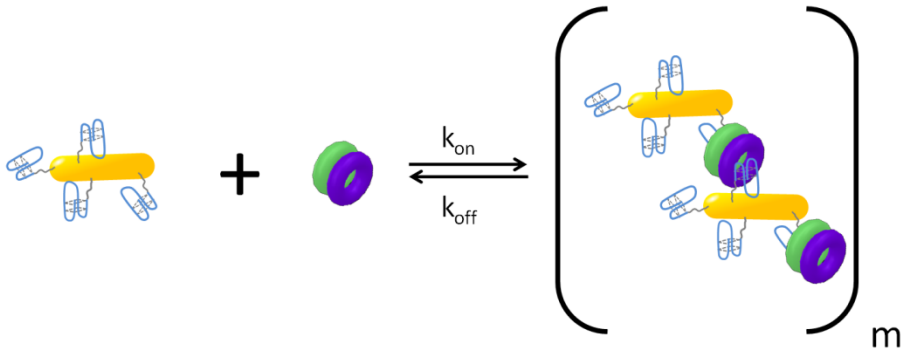

Figure 3-14: Overall kinetic scheme of NR assembly

In figure 3-14, one can observe the scheme studied to solve the assembly of NR aggregates. In this case, k_{on} and k_{off} are the overall kinetic constants that rule the system. As we previously introduced, this constants will mainly depend on the rate of formation of the aggregates; as we consider that the NR-thrombin interaction to form unit blocks of aggregation is fast compared to the assembly of the aggregate. We can develop the following equation to explain the NR assembly using these considerations:

$$\frac{\partial(Agr)_m}{\partial t} = k_{on}[NR][th] - k_{off}[Agr] \quad \text{(Eq.3.26)}$$

Where we picture that the rate of formation of the aggregate (Agr), is a function of the kinetic constants k_{on} and k_{off}. [NR] is the concentration of free NRs, [th] is the concentration of thrombin that we may consider constant, and [Agr] is the concentration of the formed aggregate. Knowing that:

$$[NR]_t = [NR_0] - m[Agr] \quad \text{(Eq.3.27)}$$

Where m is the number of nanorods present in the aggregate.

3.3.1. Theoretical

We may take into consideration that once the aggregates are formed, the concentration of the aggregates determines the absorbance difference, and not the size of the aggregates[52]. Therefore, after the initial binding, the critical size of the aggregates would remain constant, and only their concentration will vary. $[NR_0]$ is the initial concentration of nanorods and $[NR]_t$ is the evolution of the concentration of the nanorods in time. We may solve this equation and find the solution that rules the aggregation of the particles as a function of time:

$$[Agr] = \frac{k'_1 NR_0 \left(1 - e^{-k_x t}\right)}{k_x} \qquad \text{(Eq.3.28)}$$

3.3.2. Results and discussion

The assembly of NR to form aggregates results in a broadening and red-shift of the SPR peak, as can be pictured in figure 3-15, indicating the assembly of the particles.

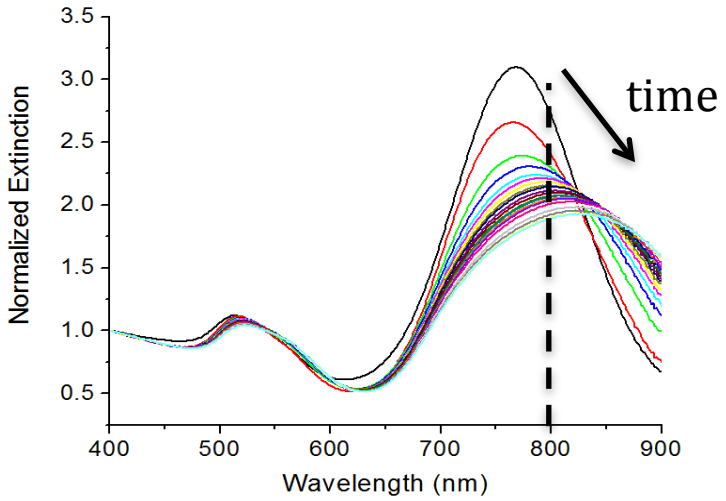

Figure 3-15: Evolution of the extinction of the NRs with time

To quantify the assembly, the ratio of extinctions at 400nm and 800nm (A_{400}/A_{800}) is plotted, which increases as a function of time in the presence of thrombin (Fig. 3-16). A_{400}/A_{800} time courses are collected for several thrombin concentrations.

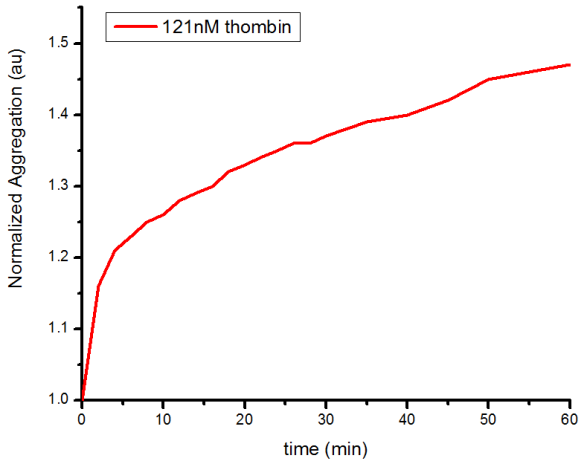

Figure 3-16: Assembly of the NRs at 121nm thrombin

We can fit equation 3.28 in order to find the kinetic constants of aggregation of the particles, as shown in figure 3-16. In order to plot the data points and fit the kinetic aquations, we will normalize our data so that the first point in the curve (time=0), will give a value of 0 formation of aggregates.

3.3.2.1. Different surface chemistries

By changing the surface chemistry of the gold nanoparticles, one can observe a change in the kinetics of the assembly process. Curves were fitted using MatLab. The resulting binding constants for each fit are:

Surface chemistry	**k'_1 (1/min)**	**k_x (1/min)**	**Goodness of the fit (r^2)**
T_{15}-TBA-High Coverage	0.1049	0.4598	0.7923
T_{15}-TBA-Low Coverage	0.2249	1	0.8589
T_{15}-TBA-PEG backfill	0.06768	0.2767	0.9222
TBA	3.13E-9	0.01151	0.7649

Table 3-1: Kinetic binding constants for different surface chemistries

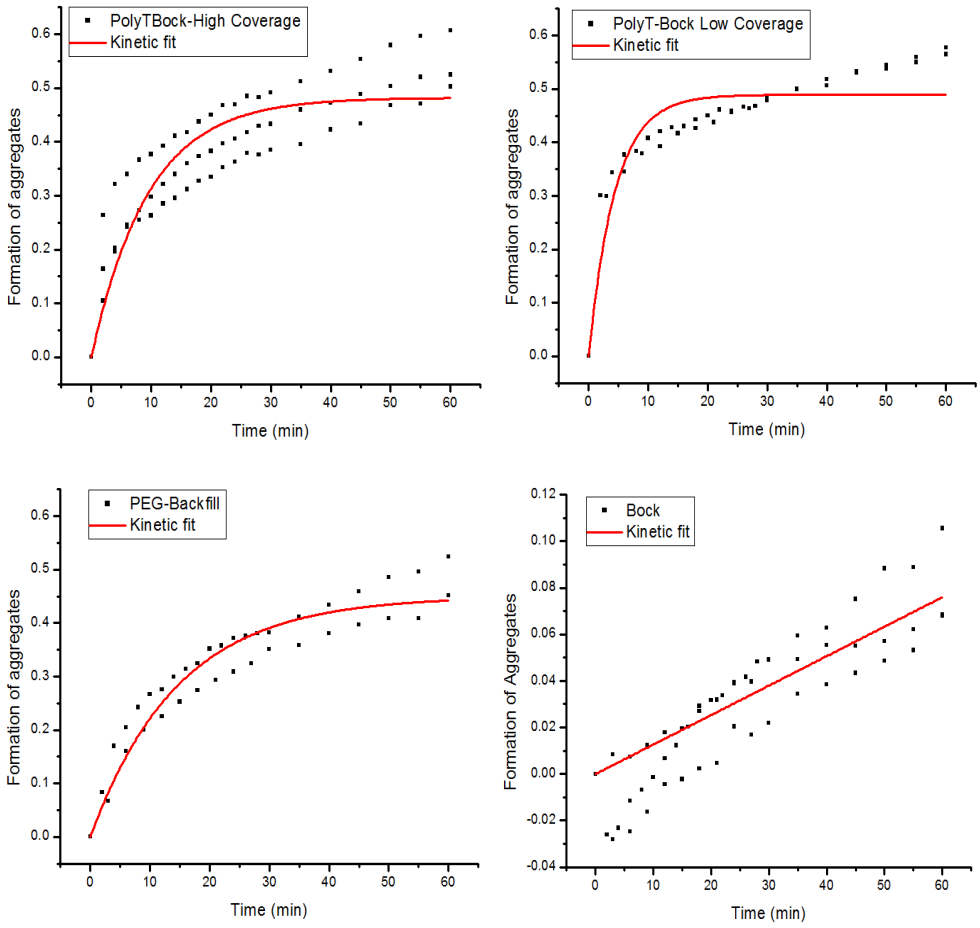

Figure 3-17: Kinetic fits with different surface chemistries

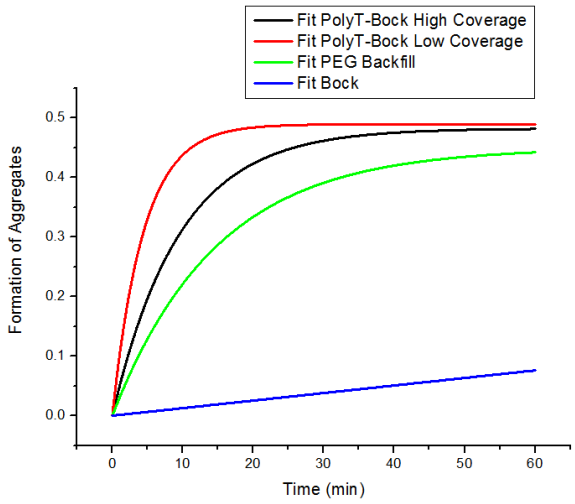

Figure 3-18: Comparison of the fits between different surface chemistries

By comparing the previous plots, one can see that the fastest aggregation occurs with the T_{15}-TBA with low coverage, followed by the T_{15}-TBA with high coverage. PEG backfill does make the aggregation process slower, and finally almost no aggregation can be observed with the TBA without a thymine spacer (Fig. 3-18).

Knowing that $K_d^b = 3.3 \pm 1.1 \times 10^{-7}$ M[38], it is possible to calculate the surface work and equilibrium binding constants of the TBA on the gold nanorod surface, as explained in Chapter 3.2. The ratio between k_{off} and k_{on} will be the equilibrium binding constant describing aggregate formation. Thrombin is in excess in solution, therefore, its concentration is considered constant, and $k'_1 = k_{on} * [th]$, thus it is possible to calculate the

binding kinetic constants of the binding of thrombin with TBA, when TBA is bound to nanoparticles with different surface chemistries.

The binding equilibrium constant to form the aggregates can be calculated from a thermodynamic perspective, as shown in Chapter 3.2. Once the binding constant in equilibrium is known, k_{off} is approximated using equation 3.30.

$$K^{\sigma} = K_b^d \exp\left(\frac{W^{\sigma}}{RT}\right) \quad \text{(Eq.3.29)}$$

$$K^{\sigma} = \frac{k_{off}}{k_{on}} \quad \text{(Eq.3.30)}$$

Surface chemistry	**k_{on} (1/s.M)**	**k_{off} (1/s)**	**K_d[b] (M)**	**K^{σ} (M)**	**W (kJ/mol)[2]**
T_{15}-TBA-High Coverage	1.44 x10^4	6.34x10^{-5}	3.3x10^{-7}	4.39x10^{-9}	-10.7
T_{15}-TBA-Low Coverage	3.10 x10^4	4.04x10^{-4}	3.3x10^{-7}	1.30x10^{-8}	-8.0
T_{15}-TBA-PEG backfill	9.32 x10^3	2.06 x10^{-5}	3.3x10^{-7}	2.21x10^{-9}	-12.4

Table 3-2: Assembly kinetic constants of different surface chemistries

[2] Surface work as calculated in Chapter 3.2 of this thesis.

The values of k_{on} obtained for the formation of complexes of typical heparin-binding blood proteins with their aptamers are of the order of 10^7. For instance, NX-213 binds to VEGF with a k_{on} of $1.0x10^7$ when both the protein and the aptamer are free in solution[53]. The slower values obtained in our experiments show that the surface plays a role, preventing the formation of the complex. Also, the different results enable understanding of the molecular structural reorganization required to form the assemblies, that is lower in the case of low coverage of T_{15}-TBA on the surface; giving a value for the k_{on} of $3.1x10^4$, and increases for both the high coverage ($1.44x10^4$) and for the PEG backfill ($9.32x10^3$). Therefore, the most crowded surface (PEG backfill) requires a major reorganization of the molecules to enable the binding of the thrombin; and in the less crowded surface (Low Coverage T_{15}-TBA) thrombin can bind more easily, as bound TBA is not sterically hindered. During the dissociation process, the results show the slowest dissociation values for the low coverage T_{15}-TBA particles, with a k_{off} of $4.04x10^{-4}$, followed by the PEG backfilled particles, that show a k_{off} of $2.06x10^{-5}$. Finally, the fastest dissociation is for the High coverage T_{15}-TBA particles, with a k_{off} of $6.34x10^{-6}$. We can compare the previous values with the k_{off} for a typical heparin-binding protein, such as VEGF unbinding from its aptamer, NX-213 is of the order of $1.4x10^{-3}$[53]. We can show that the dissociation on the surface of a NR is much faster than the one that would be obtained with the molecules in solution.

3.3.2.2. Different concentrations of biomolecule added

We have observed that the binding kinetics of nanorods depends on the concentration of thrombin added to the system. We can also fit equation (3.28) to different concentrations of thrombin added in the solution, in order to compare the binding constants. The kinetic constants obtained from fitting equation 3.28 to the T_{15}-TBA with High Coverage aggregation data are:

[thrombin]	**k'_1**	**k_x**	**Goodness of the fit (r^2)**
121nM	0.1049	0.4597	0.7923
61nM	0.05348	0.2595	0.8945
38nM	0.1427	0.443	0.8299
26nM	0.9532	0.597	0.9832

Table 3-3: Kinetic binding constants for High Coverage NR-T_{15}-TBA

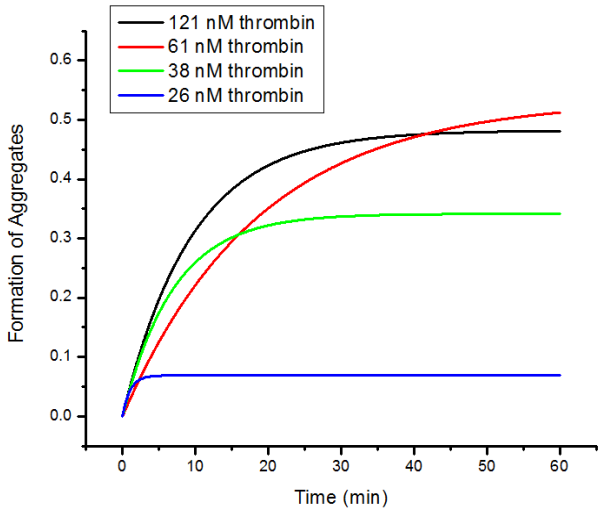

Figure 3-19: T_{15}-TBA high coverage kinetics at different thrombin concentrations

[thrombin]	**k_{on} (1/s.M)**	**k_{off} (1/s)**	**K^{σ} (M)**	**W (kJ/mol)**
121nM	1.44×10^{4}	6.34×10^{-5}	4.39×10^{-9}	-10.7
61nM	1.46×10^{4}	6.41×10^{-5}	4.39×10^{-9}	-10.7
38nM	6.26×10^{4}	2.74×10^{-4}	4.39×10^{-9}	-10.7
26nM	6.11×10^{5}	2.68×10^{-3}	4.39×10^{-9}	-10.7

Table 3-4: Calculated kinetic binding constants for high coverage T_{15}-TBA

We can observe that the association process is faster with lower concentrations of thrombin in solution, and the dissociation process is has a higher rate with higher concentrations of thrombin added in solution.

In the case of Low Coverage T_{15}-TBA NRs, the fit of equation 3.28 gives the following results:

[thrombin]	**k'_1**	**k_x**	**Goodness of the fit (r^2)**
121nM	0.2243	0.9977	0.8589
61nM	0.2526	1.006	0.8516
30nM	0.2328	0.6531	0.8483

Table 3-5: Kinetic binding constants for Low coverage NR-T_{15}-TBA

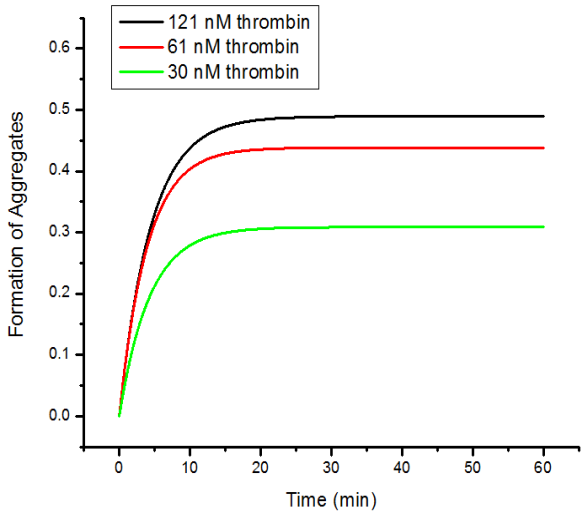

Figure 3-20: T_{15}-TBA low coverage kinetics at different thrombin concentrations

[thrombin]	k_{on} (1/s.M)	k_{off} (1/s)	K^{σ} (M)	W (kJ/mol)
121nM	3.09 x10^{4}	4.03x10^{-4}	1.30x10^{-8}	-8.0
61nM	6.90 x10^{4}	9.00x10^{-4}	1.30x10^{-8}	-8.0
30nM	1.29 x10^{5}	1.69 x10^{-3}	1.30x10^{-8}	-8.0

Table 3-6: Calculated binding constants for T_{15}-TBA with Low coverage

The aggregation kinetics for the PEG-backfilled samples yields the following results:

[thrombin]	k'_1	k_x	Goodness of the fit (r^2)
121nM	0.06772	0.2728	0.9222
61nM	0.1102	0.3714	0.7998
38nM	0.2081	0.5287	0.9331

Table 3-7: Kinetic binding constants for PEG backfilled NR-T_{15}-TBA

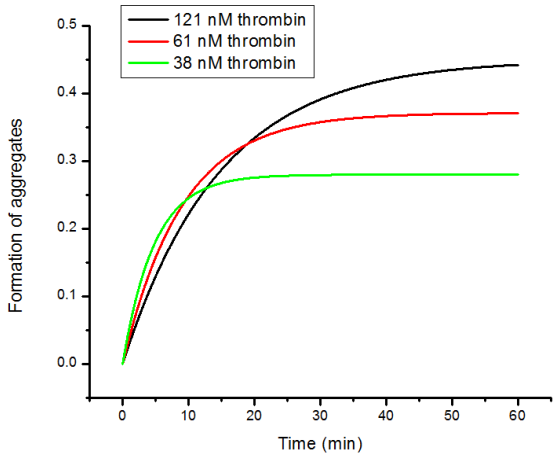

Figure 3-21: PEG Backfill kinetics at differetn thrombin concentrations

[thrombin]	**k_{on} (1/s.M)**	**k_{off} (1/s)**	**K^{σ} (M)**	**W (kJ/mol)**
121nM	9.33×10^{3}	2.06×10^{-5}	2.21×10^{-9}	-12.4
61nM	3.01×10^{4}	6.65×10^{-5}	2.21×10^{-9}	-12.4
38nM	9.13×10^{4}	2.01×10^{-4}	2.21×10^{-9}	-12.4

Table 3-8: Calculated kinetic binding constants for PEG-backfilled NR-T_{15}-TBA

3.3.4. Conclusions

We have been able to find a kinetic model to explain the mechanism of the biomolecule induced assembly of nanoparticles, by assuming that the system kinetics do not change after every subsequent NR addition to form the aggregate. We have as well assumed that the rate-determining step during the assembly is not the thrombin-TBA recognition, but the assembly of thrombin molecules to different NRs.

The kinetic model has been probed as a function of thrombin concentration and different surface chemistries of NR, in order to observe mechanism differences between the samples. We have seen that the kinetics can be tuned by changing the surface chemistry of the particles.

By using the binding constants calculated in the previous chapter of this thesis, we can calculate the constants of formation and dissociation of the aggregates. The assembly

process is slower than if the molecules were not bound to NRs, and the disassembly shows values of similar orders of magnitude to the binding in solution. Surface chemistry plays an important role in the kinetics of NRs assembly, and we have shown that as the surface becomes more crowded with molecules, the binding process is slower due to the molecular reorganization required.

Also, different concentrations of thrombin added show that the size of the aggregates depends on the available thrombin in solution. Also, the rate constants for different concentrations of thrombin added have been calculated. The results indicate that the interactions of thrombin with TBA when it is bound to a surface are slower than the rates that would be obtained with thrombin and TBA both free in solution. This demonstrates that surface effects can significantly impact biomolecular interactions. We have observed a 1000 fold difference in the association process, and a 10-1000 fold difference during the dissociation.

3.4. Reversible nanomachinery at the nanoparticle-biomolecule interface

With the combination of biology and nanotechnology it is possible to develop devices smaller and more efficient than the ones currently available. Such nanodevices can be used to manipulate atoms and molecules at the cellular level, with huge sensitivity and selectivity. Gold nanoparticles conjugated with biomolecules can be used for sensing applications to detect proteins in contact with their surface[40, 48, 54, 55]. Also, nanodevices that cycle though states of assembly have been explored for a number of applications, such as drug delivery[55-57].

In particular, the thrombin-TBA interaction has been studied in solution and it is highly specific and reversible, and may be viewed as a nanomachine that cycles though assembly states after the addition of thrombin and DNA strands. Interfacing this nanomachine to a gold nanoparticle surface enables for quantification of the interactions at the nanoscale[58]. Thrombin binding aptamer can bind to thrombin at either exosite I or II, the interaction of thrombin to TBA-conjugated NRs results in NR self-assembly[59] that can be reversed after the addition of the complementary DNA sequence (AntiTBA) of the TBA (Fig. 3-22).

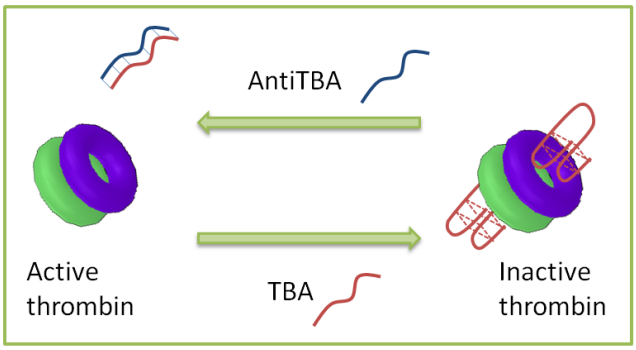

Figure 3.22: Thrombin-TBA nanomachine

In this reversible nanomachine, TBA binds and releases thrombin after the addition of the AntiTBA. However, when interfacing biological nanomachines to nanoparticles, it is necessary to understand a number of interactions that can be produced in the surface of the particles.

3.4.1. Theoretical

From a thermodynamic perspective, the competitive binding of DNA and thrombin on a gold nanorod surface conjugated with TBA can be pictured as a disassembly process, in which the addition of the complementary DNA sequence of the TBA competes with the thrombin to bind to TBA. This can be represented as an equilibrium between an aggregated and a disaggregated state, which is states 1 and 5 from figure 3.23.

Therefore, disaggregation can be described in terms of the binding efficiency for one TBA, θ[113]:

$$\theta = \frac{K^{\sigma}[anti]}{1 + K^{\sigma}[anti]} = \frac{1}{1 + \frac{1}{[anti]K^{\sigma}}} \qquad \text{(Eq.3.31)}$$

Where Θ is the binding efficiency of the NR-TBA receptor as a whole, K^{σ} is the equilibrium association constant of the TBA-antidote-thrombin competitive binding confined at the NR surface and $[anti]$ is the equilibrium concentration of antidote in solution.

TBA-thrombin and TBA-Antidote binding is confined on the NR surface, so the overall Gibbs free energy of the reaction is comprised of both a chemical and a surface contribution. The chemical contribution is related to TBA-thrombin and TBA-antidote binding, whereas the surface contribution describes the work spent in accommodating the thrombin and the DNA on the surface and for the concomitant nanoscale rearrangement of the bound and adjacent TBA molecules[8, 12]. The overall surface effect on aggregation can be understood if we construct a thermodynamic cycle that goes from the free state (state 1) to the aggregated state (state 5) that is broken down into four hypothetical steps (Fig. 3.23). The first step describes the release of TBA bound to thrombin from the NR to the (bulk) solution (from 1 to 2), the second step the TBA-thrombin recognition in solution (2 to 3), the third the DNA-DNA interaction (3-4), and finally the conjugation of the TBA-Antidote complexes to the NR (4-5).

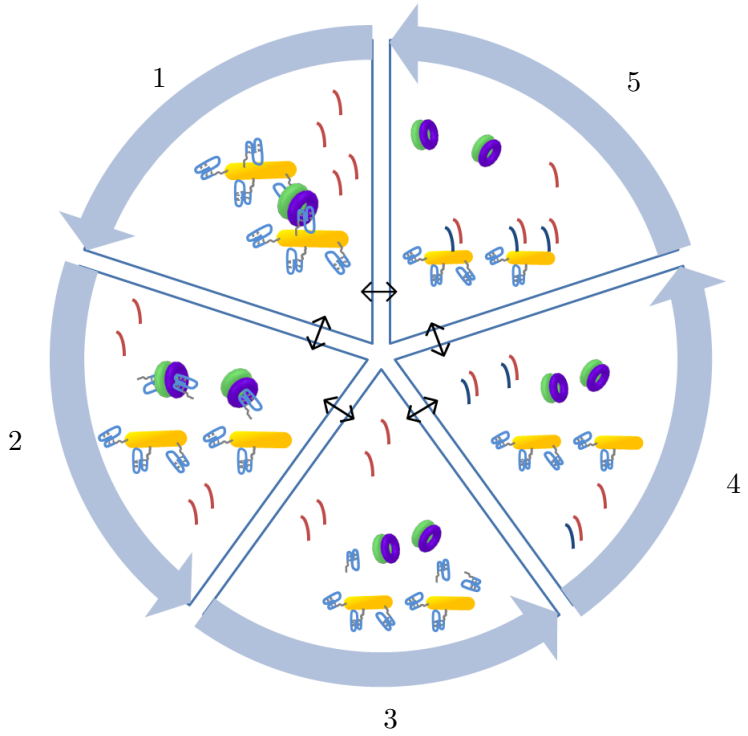

Figure 3.23: Thermodynamic cycle of NRs disassembly

$$\Delta G_{dis} = \Delta G_{rel} + \Delta G_{hybr} + \Delta G_{thTBA} + \Delta G_{bind} \quad \text{(Eq.3.32)}$$

Where the Gibbs free energy of the release and binding are the surface work contributions,

$$\Delta G_{dis} = W_s + \Delta G_{hybr} + \Delta G_{thTBA} \quad \text{(Eq.3.33)}$$

Therefore, knowing that:

$$\Delta G_{dis} = -RT\ln\left(K^{\sigma}\right) \qquad \text{(Eq.3.34)}$$
$$\Delta G_{hybr} = -RT\ln\left(K_{hybr}\right)$$
$$\Delta G_{thTBA} = -RT\ln\left(K_{b}\right)$$

We can substitute these equations in eq. 6-33:

$$\frac{1}{K^{\sigma}} = \frac{K_b^d}{K_{hybr}}\exp\left(\frac{W_s}{RT}\right) \qquad \text{(Eq.3.35)}$$

We may substitute Eq 6.35 in Eq. 6.31, and obtain the modified Langmuir equation that can be used to fit our data and obtain the surface contributions on the DNA induced disassembly of NR aggregates:

$$\theta = \frac{1}{\frac{K_b^d}{[anti]K_{hybr}}\exp\left(\frac{W_s}{RT}\right)+1} \qquad \text{(Eq.3.36)}$$

3.4.2. Results and discussion

By optical absorbance it is possible to observe the assembly of gold nanorods conjugated with TBA after the addition of thrombin, and the disassembly after the addition of Anti-TBA.

After the addition of thrombin, one can observe that the aggregation of the particles increases (until minute 60), indicating the assembly of the particles. At minute 60, the

antiTBA was added in the solution, and one can see that the value of aggregation returns to 1, indicating that the assembly of the particles was reversed.

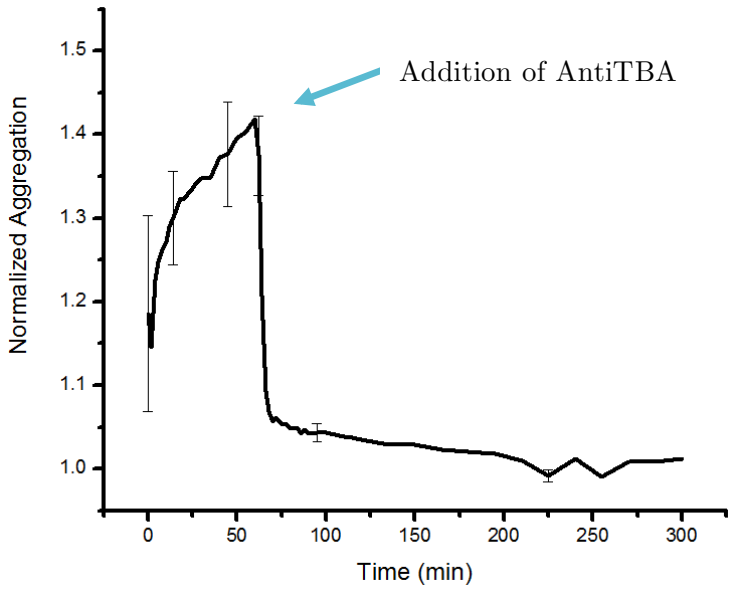

Figure 3-24: Reverisble assembly of NRs after the addition of thrombin and anti-TBA

It is possible to add different amounts of AntiTBA to the solution and observe that as the concentration of AntiTBA decreases, the rate of disassembly is slower.

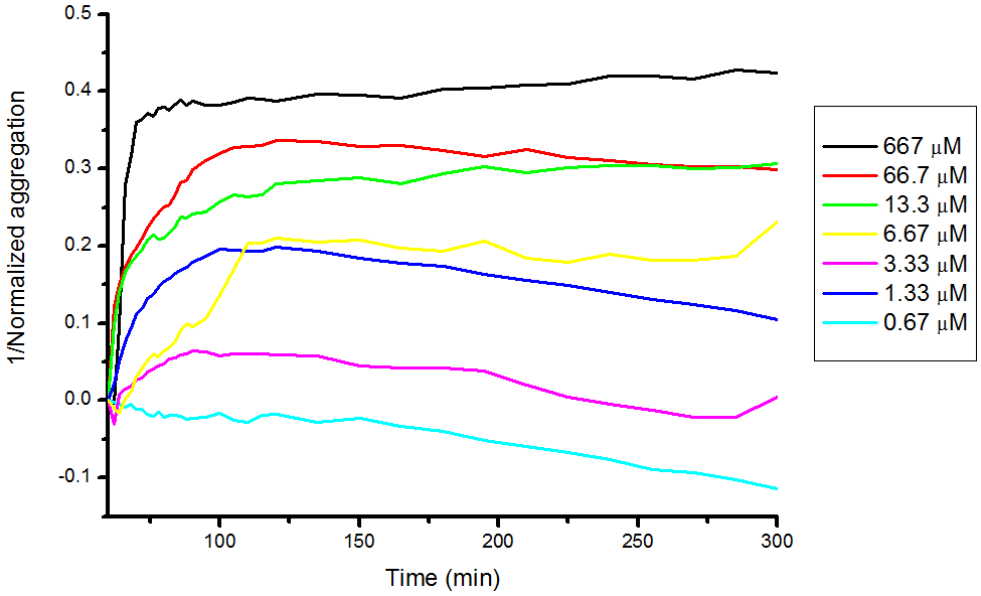

Figure 3-25: Disassembly of NRs after antidote addition

3.4.3. Conclusions

We have seen that the assembly of NR after thrombin addition can be reversed with the addition of the AntiTBA. Different concentrations of AntiTBA have been added to the particles. As this is a work in progress, more data needs to be obtained in order to have concluding results for the disassembly of NRs after the addition of the TBA's complementary DNA sequence. Future work includes a thermodynamic and kinetic study of the TBA-thrombin-TBAAnti nanomachines.

3.5. Quantifying DNA hybridization at the nanoparticle interface

"DNA not only directs the synthesis of proteins and the development of the cell, but it is also the substance that is copied to enable a similar development of the progeny of that cell"[3][60]. The introduction of DNA in cells as new material is a promising tool to treat difficult diseases; however, it is necessary to carry the DNA to the cells so that every cell suffering from a non-functional group can be cured. Currently, the use of gold nanoparticles for gene therapy vectors has received much attention. Therefore, it is necessary to understand the interaction that the DNA has with the particles. Some studies have already been able to elucidate the interaction of DNA with nanoparticle surfaces [10, 45, 47, 61, 62].

Also, the ssDNA-ssDNA interaction is highly attractive for nanomachines due to its high specificity and reversibility. Therefore it is not surprising that since the development of nanotechnology, many researchers have started investigating the applications of DNA at the interface.

Although the DNA hybridization has been widely studied in solution, a few studies exist on the hybridization of DNA on surfaces, where the interactions between neighbouring

[3] Kornberg's Nobel Lecture, in 2006

DNA sequences and between the surface and the DNA play an important role in the DNA hybridization at the interface[3]. Due to the size of nanomaterials, the surface dominates their behavior. The distribution of the DNA on the surfaces can vary with the curvature of the particles [10, 50, 51]. Also, DNA can stick on the NR surface, preventing it from hybridizing to its target. Nanoparticles have charges or can be coated with ligands that affect the interactions between the biomolecules at the interface. Some work on the conformation of DNA on gold nanosphere surfaces has already been done in Hamad-Schifferli's group[33, 61].

Here, we develop a thermodynamic treatment to quantify the surface effects on the DNA hybridization. This thermodynamic treatment allows for quantitative description of the interface effects. We probe how the interaction is influenced by the nanoparticle's curvature and surface chemistry and the DNA coverage and spacer length.

3.5.1. Theoretical

The hybridization of fluorescently tagged DNA on the NRs' surface results in fluorescense resonance energy transfer (FRET) from one of the fluorophore tags (FAM) to the other (TMR), as sketched in figure 3.26.This can be represented as the equilibrium between a free and an bound state.

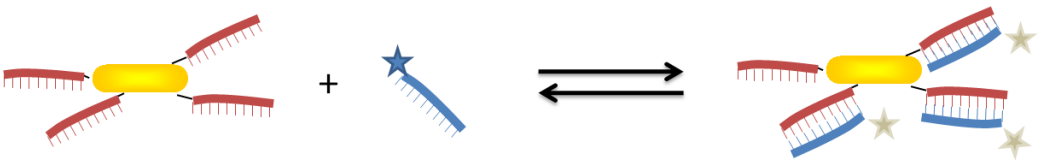

Figure 3-26: DNA hybridization on the NRs surface

Where the red DNA sequence would be tagged with TMR (not shown in the drawing for simplicity), and the blue DNA sequence would be tagged with FAM. One can observe that the fluorescence signal will decrease when the complementary DNA sequence is bound to the NPs, due to proximity of the two fluorophore tags. We can subtract the signal at 80ºC (complementary DNA sequence is free in solution) from the signal at 25ºC (complementary sequence of DNA is bound to the particles) and obtain a plot that shows the unbound DNA as a function of antidote concentration added. Instead of measuring the DNA fluorescence increase at 80ºC, it would be possible to measure the fluorescence in the presence of MHA-NR, where no hybridization could occur. It is necessary to compare with NRs in solution as NRs can absorb FAM's emission.

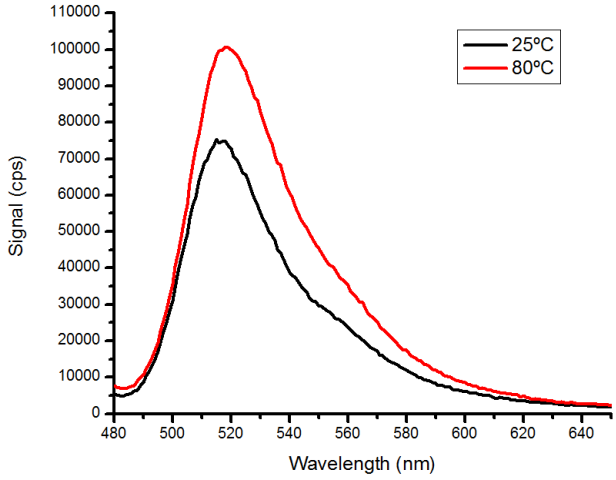

Figure 3-27: FRET curve at 25ºC and 80ºC

One can fit the Langmuir isotherm introduced in Chapter 3.2.1.1: Langmuir Isotherm, in order to find the binding constants of the DNA on the surface of the particles.

$$q_e = \frac{Qb[A]}{1 + b[A]} \qquad \text{(Eq.3.37)}$$

Where q_e is the coverage of the adsorbate molecule on the particles, Q is the maximum number of A molecules that can theoretically be absorbed on the surface, and b is designated as the binding efficiency term. One can perform numerical fits of adsorption data in order to obtain values for Q and b to allow interpretation of the absorption behavior.

Also, the melting temperature of the DNA can be measured by slowly heating the NR sample with DNA hybridized, and measuring the inflection point of the sigmoidal curve fitted to the data points.

3.5.2. Results and discussion

We can observe that by using different surface chemistries on the particles, the hybridization thermodynamics will be different. We will measure the fluorescence at 25^{o}C, when the DNA is hybridized on the surface of the particles, and compare it to the fluorescence at 80^{o}C, when all the DNA is free in solution.

$$DNA_{bound} = DNA_{total} - DNA_{free}$$

We know that the fluorescence of our fluorophore tags is low compared to the change in fluorescence increase after the DNA us unbound.

For different surface chemistries, we can observe different constants in the Langmuir fitting of the curves. This enables us to compare among experiments. Note that the following results are preliminary data, and only give an idea of the hybridization with different surface chemistries and sizes of the particles.

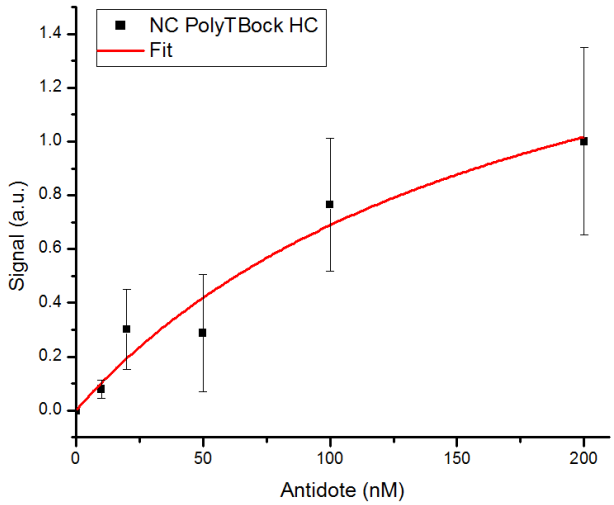

Figure 3-28: DNA hybridization on high coverage NCs

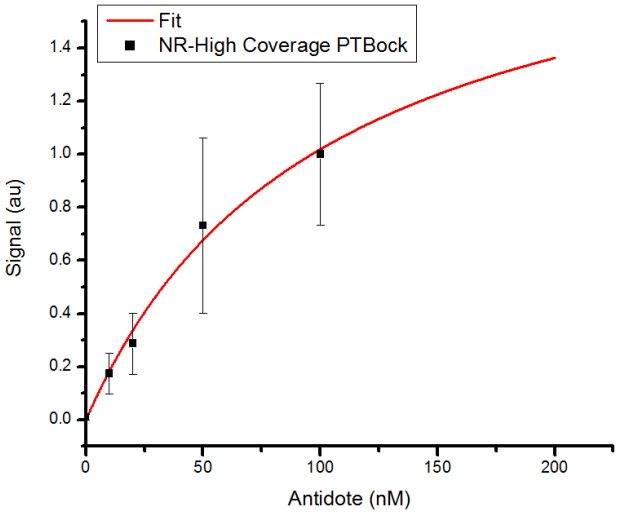

Figure 3-29: DNA hybridization on high coverage NRs

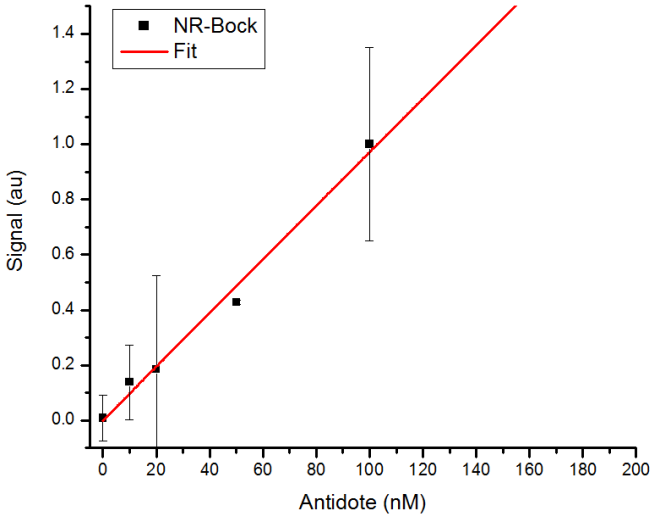

Figure 3-30: DNA hybridization on TBA NRs

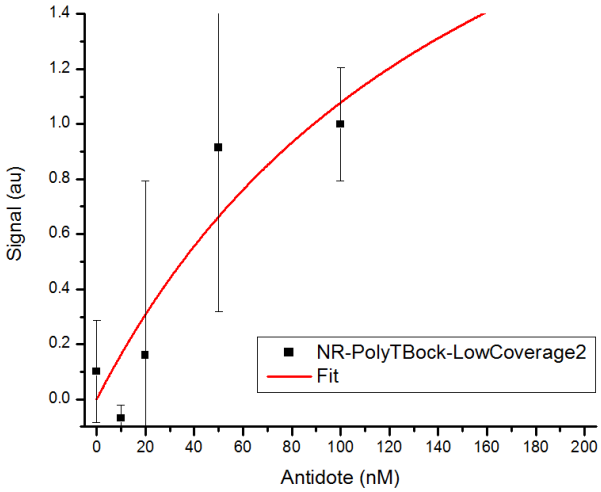

Figure 3-31: DNA hybridization on mid-Coverage NRs

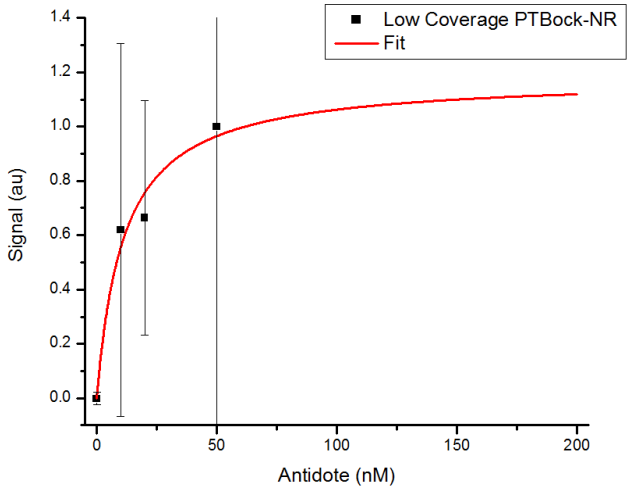

Figure 3-32: DNA hybridization on Low-coverage NRs

Sample	**Q**	**b (1/nM)**	**DNA attached DNA/NP**
High Coverage NCs	1.941	5.499×10^{-3}	137
High Coverage NRs	2.058	9.807×10^{-3}	173
Mid-Coverage NRs	2.872	6.006×10^{-3}	122
Low-Coverage NRs	1.182	8.889×10^{-2}	35
TBA-NR	2.595×10^{2}	3.76×10^{-5}	265

Table 3-9: Compared values of DNA hybridization on different surfaces

We can observe that the binding efficiency of the complementary DNA sequence in long capsules is higher than in the shorter NRs, while Q (theoretical maximum amount of DNA that can be absorbed) remains constant. The particles conjugated with DNA

without a T_{15} spacer show a higher theoretical amount of DNA absorbed, which could be due to a higher coverage on the surface as compared to the particles conjugated with the DNA sequence with High Coverage. The three NRs samples with increasing coverage of DNA show a higher binding efficiency as the coverage of the attached DNA increases, and a lower Q as the coverage decreases.

We can also measure the melting temperature of the DNA on the surface of the particles (Fig. 3-33). The melting temperature of the DNA on the surface of the particles is 39ºC, which is lower than the melting temperature that the free 15mer would have in solution (which has been calculated to be 49ºC). A possible explanation might be that the increase in the melting temperature is due the DNA not being able to completely hybridize due to the proximity of the surface.

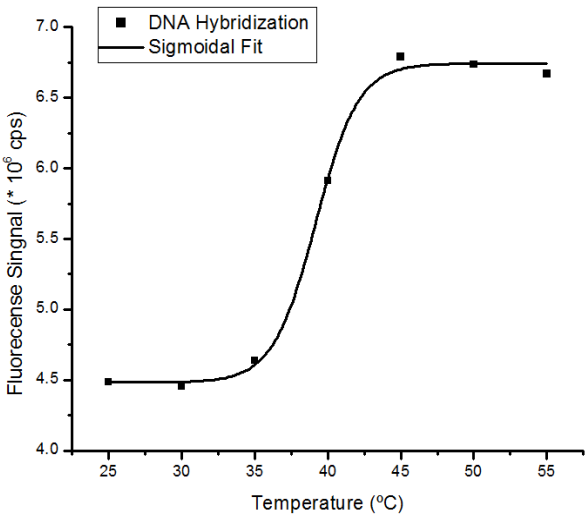

Figure 3-33: Sigmoidal fit for the DNA hybridization (r^2=0.998)

3.5.3. Conclusions

We have been able to find the surface binding efficiency of DNA on the surface of gold nanorods, for different surface chemistries of the NRs. and the compare the surface effects of the DNA hybridization, as well as being able to see the melting temperature of the DNA when hybridized on the surface of a particle. This is work in progress; therefore, some experiments need to be performed in order to find reliable results for the hybridization of DNA on surfaces.

So far, we have observed that the surface chemistry, as well as the size of the nanomaterials plays an important role in the hybridization of the DNA on them. Note that the results are not concluding, and more experiments need to be performed. However, it seems that the binding efficiency increases with lower coverage on the particles, and it is lower with longer particles. This could be explained as in the longer particles there is a higher area of flat surface that would hinder the DNA from hybridizing. We have also observed a very high Q (theoretical maximum amount of the complementary sequence that can be absorbed) for the particles without a T_{15} spacer that could be explained by the higher coverage of DNA on these samples.

Further experiments include comparing the DNA hybridization with spherical particles, in order to be able to observe the radius of curvature dependence on hybridization, and a

new method to obtain more accurate fluorescence readings. Also, the hybridization of DNA on particles with a PEG backfill and a HSA block should be performed.

3.6. Conclusions

In this work, we have discussed the effects that biological nanomachines have in the interface with NRs surfaces. We have both studied the hybridization of DNA on surfaces, and the assembly of NRs induced by the presence of a binding biomolecule –in our case thrombin-. We have studied the thermodynamics of the assembly and disassembly of NRs.

We have introduced a model to explain the thermodynamics of NRs assembly in the presence of thrombin. This model is completely general and enables for the calculation of the surface work that is produced on the NRs surface during the assembly process. By using this approach, we have been able to study the interfacial effects on NRs with different surface chemistries. Also, the kinetics of the binding process has been introduced. We have used a simplified model to explain the kinetics of NRs assembly, and we have described the basics to formulate a more accurate method to explain the assembly mechanism. Also, a model to explain the NRs disassembly after the addition of TBA's complementary sequence has been introduced.

DNA hybridization in the interface has been introduced. We have been able to describe it by using Langmuir's approach of surface absorption. We calculated the binding efficiency of complementary DNA on the surface of NRs with different surface chemistries, and,

although more experimentation needs to be done to obtain more concluding results, we have observed a clear difference in the binding efficiency depending on the surface properties of the particles.

All of these results help to quantitatively describe the physical properties of the interface of biomolecules with nanomaterials, which can aid applications in which nanomaterials are used for biological applications.

3.7. Bibliography

[1] Aubin-Tam ME, Hamad-Schifferli K. Structure and function of nanoparticle-protein conjugates. Biomedical Materials 2008;3:17.

[2] Gong P, Levicky R. DNA surface hybridization regimes. Proceedings of the National Academy of Sciences of the United States of America 2008;105:5301.

[3] Oliviero G, Federici S, Colombi P, Bergese P. On the difference of equilibrium constants of DNA hybridization in bulk solution and at the solid-solution interface. Journal of Molecular Recognition 2011;24:182.

[4] Aubin-Tam ME, Hamad-Schifferli K. Gold nanoparticle cytochrome c complexes: The effect of nanoparticle ligand charge on protein structure. Langmuir 2005;21:12080.

[5] Aubin-Tam ME, Hwang W, Hamad-Schifferli K. Site-directed nanoparticle labeling of cytochrome c. Proceedings of the National Academy of Sciences of the United States of America 2009;106:4095.

[6] Nel AE, Madler L, Velegol D, Xia T, Hoek EMV, Somasundaran P, Klaessig F, Castranova V, Thompson M. Understanding biophysicochemical interactions at the nano-bio interface. Nature Materials 2009;8:543.

[7] Park S, Hamad-Schifferli K. Nanoscale interfaces to biology. Current Opinion in Chemical Biology 2010;14:616.

[8] Federici S, Oliviero G, Hamad-Schifferli K, Bergese P. Protein thin film machines. Nanoscale 2010;2:2570.

[9] Park S, Hamad-Schifferli K. Enhancement of In Vitro Translation by Gold Nanoparticle-DNA Conjugates. Acs Nano 2010;4:2555.

[10] Cederquist KB, Keating CD. Curvature Effects in DNA:Au Nanoparticle Conjugates. Acs Nano 2009;3:256.

[11] Piletska EV, Piletsky SA. Size Matters: Influence of the Size of Nanoparticles on Their Interactions with Ligands Immobilized on the Solid Surface. Langmuir 2010;26:3783.

[12] Bergese P, Oliviero G, Alessandri I, Depero LE. Thermodynamics of mechanical transduction of surface confined receptor/ligand reactions. Journal of Colloid and Interface Science 2007;316:1017.

[13] Shu WM, Liu DS, Watari M, Riener CK, Strunz T, Welland ME, Balasubramanian S, McKendry RA. DNA molecular motor driven micromechanical cantilever arrays. Journal of the American Chemical Society 2005;127:17054.

[14] Cedervall T, Lynch I, Lindman S, Berggård T, Thulin E, Nilsson H, Dawson KA, Linse S. Understanding the nanoparticle-protein corona using methods to quantify exchange rates and affinities of proteins for nanoparticles. Proceedings of the National Academy of Sciences of the United States of America 2007;104:2050.

[15] Beyer S, Simmel FC. A modular DNA signal translator for the controlled release of a protein by an aptamer. Nucleic Acids Research 2006;34:1581.

[16] Dittmer WU, Reuter A, Simmel FC. A DNA-based machine that can cyclically bind and release thrombin. Angewandte Chemie-International Edition 2004;43:3550.

[17] Grzelczak M, Vermant J, Furst EM, Liz-Marzan LM. Directed Self-Assembly of Nanoparticles. Acs Nano 2010;4:3591.

[18] Feldkamp U, Niemeyer CM. Rational design of DNA nanoarchitectures. Angewandte Chemie-International Edition 2006;45:1856.

[19] Niemeyer CM. Nanoparticles, proteins, and nucleic acids: Biotechnology meets materials science. Angewandte Chemie-International Edition 2001;40:4128.

[20] Yigit MV, Mazumdar D, Lu Y. MRI detection of thrombin with aptamer functionalized superparamagnetic iron oxide nanoparticles. Bioconjugate Chemistry 2008;19:412.

[21] Shenhar R, Rotello VM. Nanoparticles: Scaffolds and building blocks. Accounts of Chemical Research 2003;36:549.

[22] Fritz J. Cantilever biosensors. Analyst 2008;133:855.

[23] Valiaev A, Abu-Lail NI, Lim DW, Chilkoti A, Zauscher S. Microcantilever sensing and actuation with end-grafted stimulus-responsive elastin-like polypeptides. Langmuir 2007;23:339.

[24] Connolly S, Cobbe S, Fitzmaurice D. Effects of ligand-receptor geometry and stoichiometry on protein-induced aggregation of biotin-modified colloidal gold. Journal of Physical Chemistry B 2001;105:2222.

[25] Bishop KJM, Wilmer CE, Soh S, Grzybowski BA. Nanoscale Forces and Their Uses in Self-Assembly. Small 2009;5:1600.

[26] Min YJ, Akbulut M, Kristiansen K, Golan Y, Israelachvili J. The role of interparticle and external forces in nanoparticle assembly. Nature Materials 2008;7:527.

[27] Klotz IM. Ligand-receptor energetics : a guide for the perplexed. New York: John Wiley & Sons, 1997.

[28] Leckband D, Israelachvili J. Intermolecular forces in biology. Quarterly Reviews of Biophysics 2001;34:105.

[29] Adamson AW, Gast AP. Physical chemistry of surfaces. New York: Wiley, 1997.

[30] Lees EE, Gunzburg MJ, Nguyen TL, Howlett GJ, Rothacker J, Nice EC, Clayton AHA, Mulvaney P. Experimental determination of quantum dot size distributions, ligand packing densities, and bioconjugation using analytical ultracentrifugation. Nano Letters 2008;8:2883.

[31] Aubin-Tam ME, Zhou H, Hamad-Schifferli K. Structure of cytochrome c at the interface with magnetic CoFe2O4 nanoparticles. Soft Matter 2008;4:554.

[32] Demers LM, Mirkin CA, Mucic RC, Reynolds RA, Letsinger RL, Elghanian R, Viswanadham G. A fluorescence-based method for determining the surface coverage and hybridization efficiency of thiol-capped oligonucleotides bound to gold thin films and nanoparticles. Analytical Chemistry 2000;72:5535.

[33] Park S, Brown KA, Hamad-Schifferli K. Changes in oligonucleotide conformation on nanoparticle surfaces by modification with mercaptohexanol. Nano Letters 2004;4:1925.

[34] Bock LC, Griffin LC, Latham JA, Vermaas EH, Toole JJ. Selection of single-stranded DNA molecules that bind and inhibit human thrombin. 1992;355:564.

[35] Padmanabhan K, Padmanabhan KP, Ferrara JD, Sadler JE, Tulinsky A. The structure of alpha-thrombin inhibited by a 15-mer single-stranded-DNA aptamer. Journal of Biological Chemistry 1993;268:17651.

[36] Leborgne S, Graber M. Amidase activity and thermal-stability of human thrombin. Applied Biochemistry and Biotechnology 1994;48:125.

[37] Lazarides AA, Schatz GC. DNA-linked metal nanosphere materials: Structural basis for the optical properties. Journal of Physical Chemistry B 2000;104:460.

[38] Pagano B, Martino L, Randazzo A, Giancola C. Stability and binding properties of a modified thrombin binding aptamer. Biophysical Journal 2008;94:562.

[39] Cheng AJ, VanDyke MW. Oligodeoxyribonucleotide length and sequence effects on intramolecular and intermolecular G-quartet formation. Gene 1997;197:253.

[40] Savran CA, Knudsen SM, Ellington AD, Manalis SR. Micromechanical detection of proteins using aptamer-based receptor molecules. Analytical Chemistry 2004;76:3194.

[41] Bustamante C, Chemla YR, Forde NR, Izhaky D. Mechanical processes in biochemistry. Annual Review of Biochemistry 2004;73:705.

[42] Wang LH, Song SP, Pan D, Li D, Fan CH. Gold nanoparticle-based sensing strategies for biomolecular detection. Pure and Applied Chemistry 2010;82:81.

[43] Zhong ZY, Male KB, Luong JHT. More recent progress in the preparation of Au nanostructures, properties, and applications. Analytical Letters 2003;36:3097.

[44] Liu SQ, Tang ZY. Nanoparticle assemblies for biological and chemical sensing. Journal of Materials Chemistry 2010;20:24.

[45] Xia F, Zuo XL, Yang RQ, Xiao Y, Kang D, Vallee-Belisle A, Gong X, Yuen JD, Hsu BBY, Heeger AJ, Plaxco KW. Colorimetric detection of DNA, small molecules, proteins, and ions using unmodified gold nanoparticles and conjugated polyelectrolytes. Proceedings of the National Academy of Sciences of the United States of America 2010;107:10837.

[46] McKenzie F, Faulds K, Graham D. Sequence-specific DNA detection using high-affinity LNA-functionalized gold nanoparticles. Small 2007;3:1866.

[47] Jin RC, Wu GS, Li Z, Mirkin CA, Schatz GC. What controls the melting properties of DNA-linked gold nanoparticle assemblies? Journal of the American Chemical Society 2003;125:1643.

[48] Wang WJ, Chen CL, Qian MX, Zhao XS. Aptamer biosensor for protein detection using gold nanoparticles. Analytical Biochemistry 2008;373:213.

[49] Pagba CV, Lane SM, Cho HS, Wachsmann-Hogiu S. Direct detection of aptamer-thrombin binding via surface-enhanced Raman spectroscopy. Journal of Biomedical Optics 2010;15:8.

[50] Kira A, Kim H, Yasuda K. Contribution of Nanoscale Curvature to Number Density of Immobilized DNA on Gold Nanoparticles. Langmuir 2009;25:1285.

[51] Hill HD, Millstone JE, Banholzer MJ, Mirkin CA. The Role Radius of Curvature Plays in Thiolated Oligonucleotide Loading on Gold Nanoparticles. Acs Nano 2009;3:418.

[52] Lim IIS, Maye MM, Luo J, Zhong CJ. Kinetic and thermodynamic assessments of the mediator-template assembly of nanoparticles. Journal of Physical Chemistry B 2005;109:2578.

[53] Green LS, Jellinek D, Bell C, Beebe LA, Feistner BD, Gill SC, Jucker FM, Janjic N. Nuclease-resistant nucleic acid ligands to vascular permeability factor/vascular endothelial growth factor. Chemistry & Biology 1995;2:683.

[54] Pavlov V, Xiao Y, Shlyahovsky B, Willner I. Aptamer-functionalized Au nanoparticles for the amplified optical detection of thrombin. Journal of the American Chemical Society 2004;126:11768.

[55] Liao HW, Nehl CL, Hafner JH. Biomedical applications of plasmon resonant metal nanoparticles. Nanomedicine 2006;1:201.

[56] De M, Ghosh PS, Rotello VM. Applications of Nanoparticles in Biology. Advanced Materials 2008;20:4225.

[57] Shawgo RS, Grayson ACR, Li YW, Cima MJ. BioMEMS for drug delivery. Current Opinion in Solid State & Materials Science 2002;6:329.

[58] de Puig H, Federici S, Baxamusa SH, Bergese P, Hamad-Schifferli K. Quantifying the Nanomachinery of the Nanoparticle-Biomolecule Interface. Small 2011;7.

[59] Zhen SJ, Huang CZ, Wang J, Li YF. End-to-End Assembly of Gold Nanorods on the Basis of Aptamer-Protein Recognition. Journal of Physical Chemistry C 2009;113:21543.

[60] Roger D. Kornberg - Nobel Lecture.

[61] Brown KA, Park S, Hamad-Schifferli K. Nucleotide-surface interactions in DNA-modified Au-nanoparticle conjugates: Sequence effects on reactivity and hybridization. Journal of Physical Chemistry C 2008;112:7517.

[62] Geerts N, Eiser E. DNA-functionalized colloids: Physical properties and applications. Soft Matter 2010;6:4647.

4. Release of covalently bound aptamers from NPs

4.1. Introduction

Phototermal therapy can be used for applications in which the control over the release of a biomolecule has to be controlled locally and externally[1, 2]. Selective release of multiple covalently bound species (ssDNA) has been demonstrated previously[3]. It has been shown that the release of a biomolecule can be accomplished by an external signal, such as laser irradiation[4-6]. Laser irradiation of NRs at their SPR leads to increased temperatures on the surface of the particles that can lead to melting, if the pulses of the laser are short enough[7], whereas continuous laser heating only leads to temperature increase on the surface of the particles without inducing melting[8]. By irradiating NRs at their SPR through fs laser irradiations, it is possible to release the thiolated DNA bound on the surface of the NRs. As it was explained in the introduction of this thesis, when the NRs are irradiated by a fs light at their SPR there is an increase of the surface temperature of the particles[9] that leads to a change in their shape[10], and also in the breakage of the gold-thiol bonds on the NPs[11].

We will use this approach in order to release of covalently bound thrombin binding aptamer (TBA). By exploring the conjugation and release of the thiolated TBA by fs

laser irradiation, it is possible to understand the degradation and activity loss of the TBA after it has been released from the NPs. One can expect a decrease in activity of the TBA, due to the high surface temperature that the NPs reach during the irradiation, which can be as high as 1000K[7, 9, 10, 12-14]. We are able to measure the activity of the TBA as a decrease of the expected effect in blood clotting time. We can also observe that the concentration of NRs necessary to achieve a high release of thiolated TBA is high, therefore, new ssDNA loading methods need to be studied.

Both NRs and NBs absorb light in the infrared region of light (Fig. 4-1), where tissue absorption is minimal. Also, because the SPRs of NRs and NBs do not interact, it is possible to excite them selectively when NRs and NBs are mixed. SPR of NRs is at 800nm, so they can be excited with a laser at 800nm; and the NBs can be excited by irradiation with a laser at 1100nm.

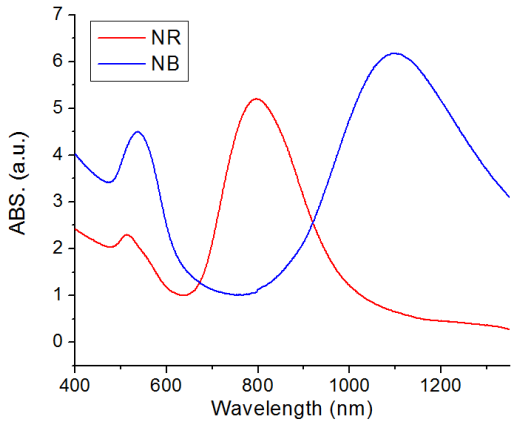

Figure 4-1. Absorbance spectra of NRs (red) and NBs (blue).

By irradiating the NRs and NBs, we melt them, which can be observed by absorbance as a decrease in the SPR peak of the particles. Melting the NPs releases the DNA that is bound to the surface of the NPs. In order to quantify the released DNA, we will use fluorescently tagged DNA and measure its concentration by fluorescence spectroscopy. Therefore, if we start from a mixture of NRs and NBs, it is possible to irradiate the mixture at 800nm with a laser, melt the NRs only and release the DNA bound to the NRs (Fig. 4-2, red DNA). By irradiating at 1100nm, we can melt the NBs only and release DNA from the NBs (Fig. 4-2, blue DNA).

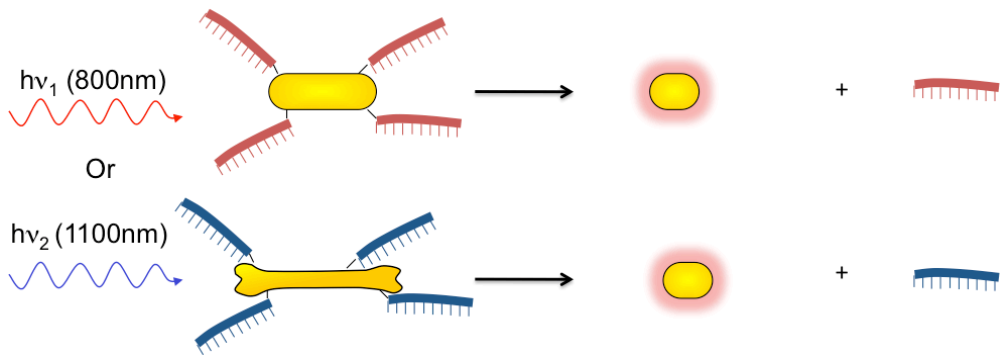

Figure 4-2. Scheme of the selective release of thiolated ssDNA

4.2. Melting the NR-CTAB and NB-CTAB

We first tested if it was possible to melt the NR-CTAB and NBs CTAB, and that it was possible to achieve a selective excitation of NRs and NBs with fs laser irradiations. The NRs could be selectively excited with a laser centered at 800nm (Fig. 4.3-blue line), because it coincides with a maximum of their SPR, and also with minimum in the absorption of the NBs. NBs could be selectively excited with a laser centered at 1100nm(Fig. 4.3-red line), as it coincides with a maximum of the SPR of the NBs and with a minimum in the absorption of the NRs.

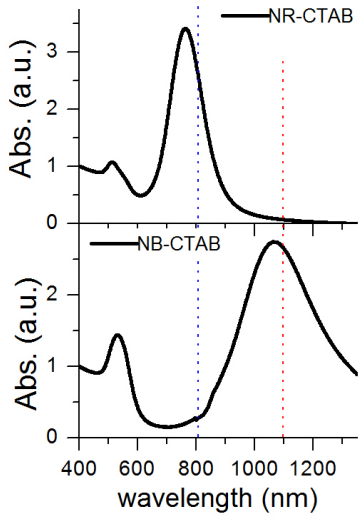

Figure 4-3. CTAB-NRs and CTAB-NBs

4.2.1. Melting NRs and NBs at their SPR

Next we tested the melting of the NRs at 800nm. Laser irradiation at 800nm of the CTAB-NRs (Fig. 4-4, black) for 15min induced a shape transformation of the NRs to spheres[10], which could be confirmed by a decrease of their absorption at 800nm, that could be observed the absorbance spectroscopy(Fig. 4-4, red). The NR concentration was 1nM.

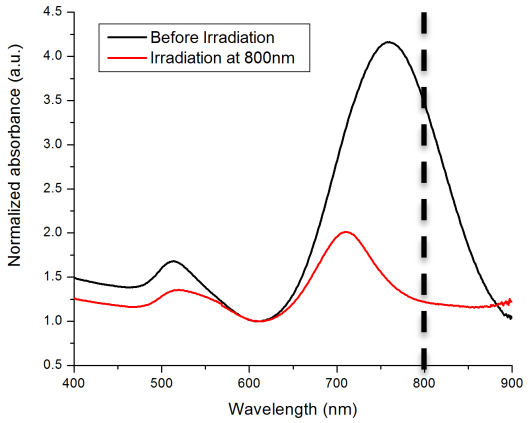

Figure 4-4. Melting CTAB-NRs at 800nm

Similarly, NBs (Fig. 4-5, black) were irradiated at 1100nm with a fs laser. Again, because the NRs had a SPR maximum at 1100nm, it was possible to melt them with the laser irradiation, as could be seen by a decrease of their SPR at 1100nm (Fig. 4-5, red). The NB concentration was 0.35nM.

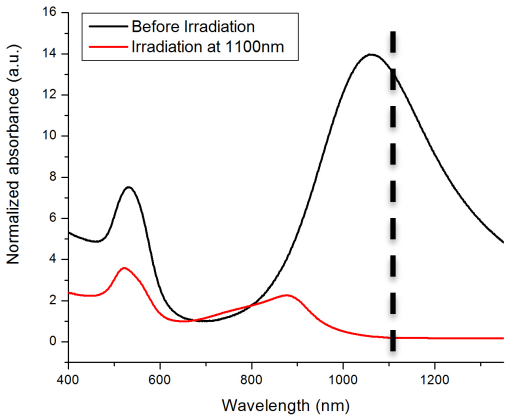

Figure 4-5. Melting CTAB-NBs at 1100nm

4.2.2. Control experiments with single NRs and NBs

We then tested that the NRs would not melt at 1100nm. In order to do that, CTAB-NRs (Fig. 4-6, black line) were irradiated at 1100nm, and the absorbance spectra of the NRs, was measured. We could observe that minimal melting of the NRs did happen (Figure 4-6, red), as the outcoming light from the laser had a linewidth of 400 nm. Nevertheless, melting was minimal, as the maximum SPR of the NRs was still visible, and only a small decrease in absorbance could be observed.

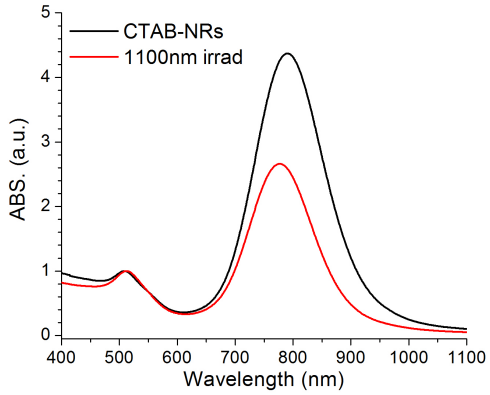

Figure 4-6. Minimal melting of the CTAB-NRs at 1100nm

We performed a similar experiment with NBs-CTAB (Fig. 4-7, black) and irradiated them at 800nm. We could not observe melting of the NBs after the irradiation (Fig. 4-7, red), indicating that the 800nm laser beam was extremely monodisperse.

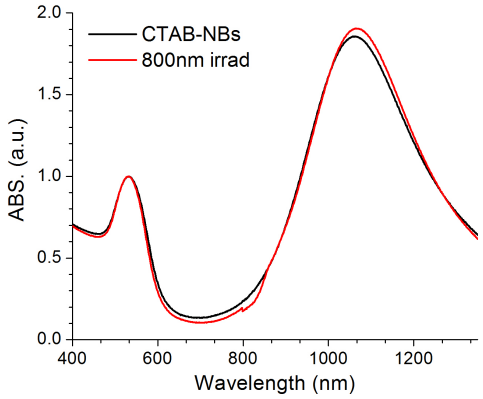

Figure 4-7. No melting of the CTAB-NBs at 800nm

Because the 800nm laser is more selective than the 1100nm laser, we decided to use the 800nm laser to release the TBA, and the 1100nm laser to release the antidote. Therefore, TBA will be bound to the NRs and anti to the NBs.

4.2.3. Selective melting of a mixture of NRs and NBs

Once we observed that selective melting of NRs and NBs by fs laser irradiations was possible, we confirmed that melting of the NRs and NBs could be selectively achieved from a mixture of NR-NBs. We introduced a mixture of NBs-NRs and irradiated them both at 800nm and at 1100nm.

First, we prepared a mixture of CTAB-NBs and CTAB-NRs (Figure 4-8, black, before irradiation) and irradiated it at 800nm for 15min and observed the decrease of the 800nm peak, the SPR of the NRs, indicating that only the NRs melted after laser irradiation at 800nm, and showing that the NBs did not melt after the irradiation (Figure 4-8, red, after irradiation).

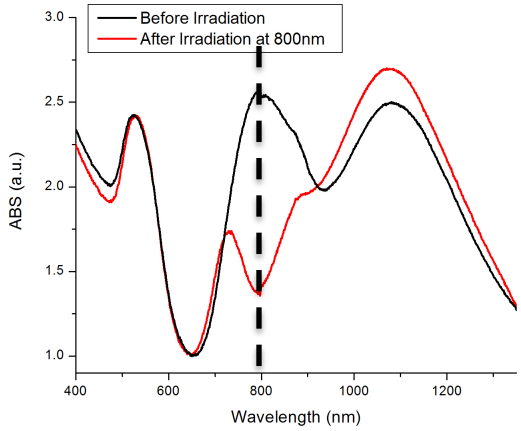

Figure 4-8. Selective melting of CTAB-NR-NB at 800nm

We then tested a mixture of NRs-CTAB and NB-CTAB (Figure 4-9, black, before irradiation) and irradiated it at 1100nm. We observed a decrease of the SPR of the NBs, showing that the NBs melted after the 1100nm irradiation, and the 800nm peak stayed, showing that the NRs did not melt after the irradiation (Figure 4-9, red).

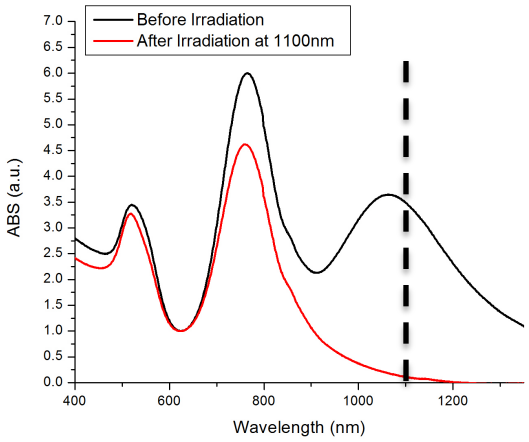

Figure 4-9. Selective melting of CTAB-NR-NB at 1100nm

Therefore, we have been able to observe melting of the CTAB-NRs and CTAB-NBs. We have seen that melting is selective and occurs only when we irradiate the NRs or NBs at their SPR. We have as well observed that selective melting is possible in a mixture of NRs and NBs.

4.3. Release of thiolated ssDNA from NRs

4.3.1. Increasing the loading of thiolated TBA with intramolecular G-quadruplexes

As we observed previously, the 800nm laser is more selective than the 1100nm laser, so we decided to link the TBA to the NRs, and the antidote to the NBs. First, we tested if higher loadings of TBA on the NRs could be achieved by taking advantage of the fact that TBA can form intermolecular G-quadruplexes. By preparing covalent DNA conjugation with increasing concentrations of the TBA with and without the T_{15} spacer, we observed that TBA without the T_{15} spacer (Fig. 4-10, red) could form intermolecular G-quadruplexes that resulted in an increased loading of TBA on the nanoparticles. On the other hand, TBA that included the T_{15} spacer (Fig. 4-10, black) did not allow for the formation of the intermolecular G-quadruplexes and resulted in a lower binding to the particles, approaching a monolayer coverage -92 ssDNA/NR [15]-.

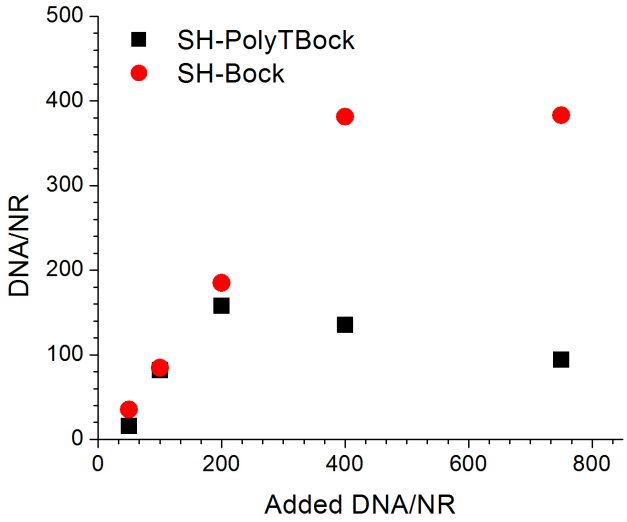

Figure 4-10. Loading of thiolated TBA with and without PolyT spacer

Because the antidote does not have a sequence that could enhance its loading by intramolecular binding, it was not necessary to test if enhanced loading could be achieved. Therefore, we conjugated 5'-SH-GGTTGGTGTGGTTGG-3' (SH-TBA) and 5'-SH-T_{15}-CCAACCACACCAACC-3' (SH-anti) to MHA-NRs and MHA-NBs respectively.

4.3.2. Aptamers and antidotes effect in blood clotting

First, we tested that the thiolated TBA and the thiolated antidote could be used to control blood clotting (Fig. 4-11). In order to do so, we added increasing amounts of

thiolated TBA [0-2500nM], and measured t_{clot}. Blood with no TBA added was normalized as t_{clot} =1.0. We observed that as the thiolated TBA concentration increased blood clotting time increased as well, showing that the thiolated TBA could bind to thrombin (Fig. 4-11, left). We also added increasing amounts of thiolated antidote to a 500nM solution of thiolated TBA, measured t_{clot} and observed that as the SH-anti/SH-TBA ratio increased, blood clotting time could be restored, showing that the thiolated antidote would form duplexes with the thiolated TBA and therefore inhibiting the binding of TBA to thrombin (Fig. 4-11, right).

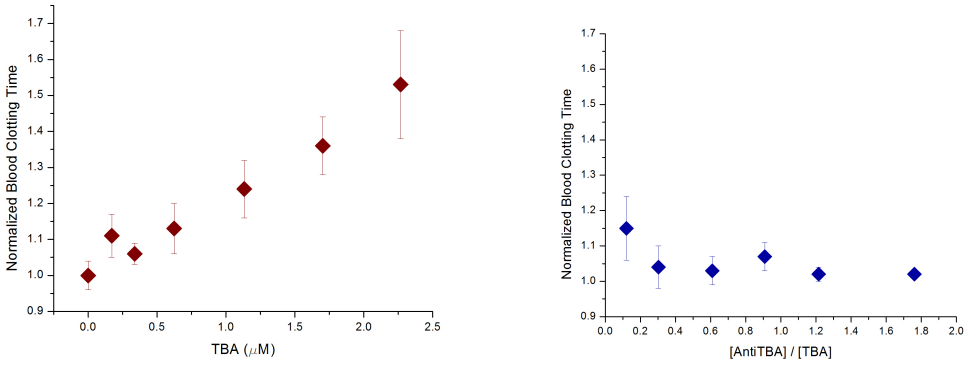

Figure 4-11. Effect of TBA in blood and effect of antidote on TBA

4.3.3. Melting and release of TBA from NRs

We then tested the release of TBA from NRs by fs irradiation of the NR SPR (Fig. 4-12). We observed NR melting, as evidenced by the decrease in the NR SPR peak, which increased with increasing laser irradiation time.

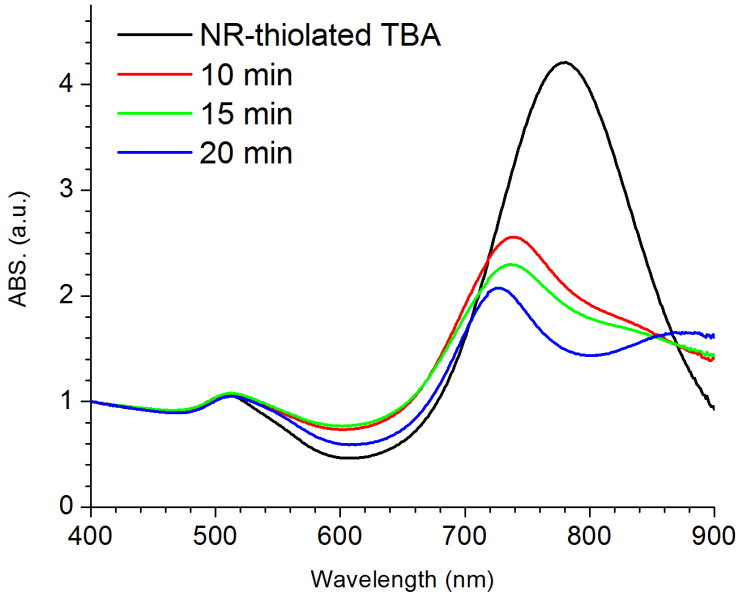

Figure 4-12. ABS spectra of 5nM TBA-NRs at increasing irradiation times

Next, we measured the concentration of TBA that was released at increasing irradiation times (Fig. 4-13). We could see that as the NRs were melted (as could be seen by a decrease of their SPR), the release of TBA increased until reaching a plateau at 20 min irradiation, suggesting that longer irradiation times were not necessary in order to obtain

an enhanced release of TBA. Obviously, irradiation times depended on the concentration of nanoparticles from where the release should be done. Higher concentrations of NRs required irradiation for longer times than lower concentrations of NRs.

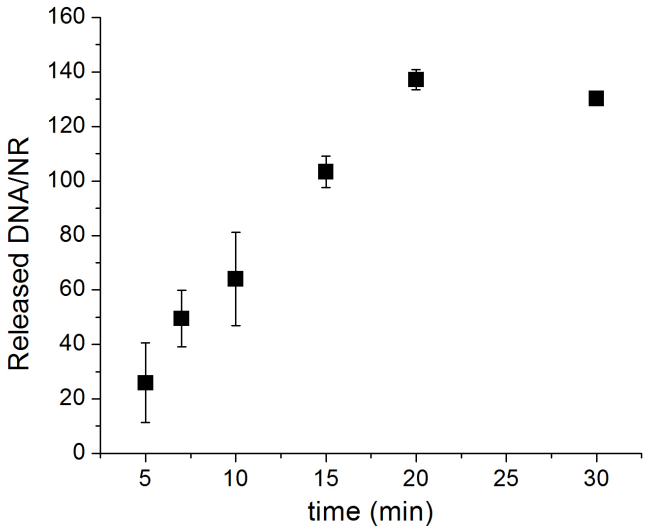

Figure 4-13. TBA release as a function of irradiation time

We then tested the effect of released TBA through from the gold nanorods. In order to do that, we covalently conjugated thiolated TBA to NRs, and irradiated a 11.22nM solution blocked with HSA (see Chapter 2: Materials and Methods). As observed in the absorbance spectra (Fig. 4-14), after the 30 min under the 800nm irradiation, the NRs melted.

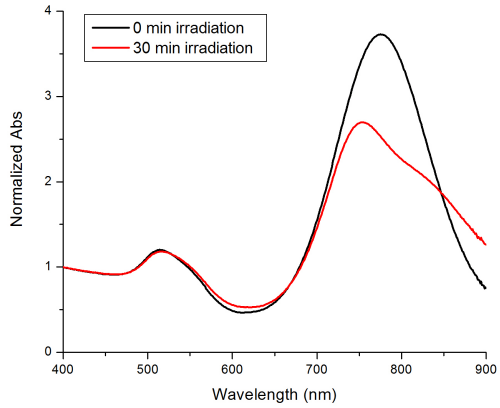

Figure 4-14. ABS spectra of TBA-NRs irradiated for 30 min

After irradiation the supernatant was collected, and the fluorescence of the supernatant was measured. We could release 1460nM TBA from the 11.22nM NR-SH-TBA solution coated with HSA, which corresponds to 130.4 TBA released per NR. (Fig. 4-15)

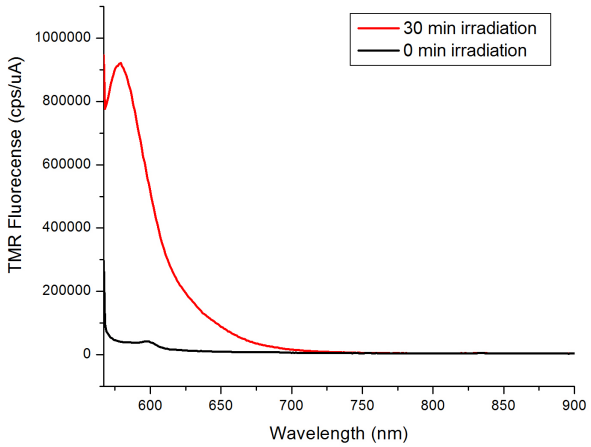

Figure 4-15. TBA release as a function of irradiation time

In order to test the functionality of the TBA after the laser irradiation, we introduced the released DNA in blood and tested the blood clotting time, and compared to undamaged SH-TBA. We indeed observed that there was a loss of functionality on the TBA, and that the TBA had a 64% activity, as compared to the theoretical value of the clotting time. Released TBA from NRs yielded an increase in clotting time of 1.18, which was equivalent to 959nM undamaged TBA (Fig. 4.16).

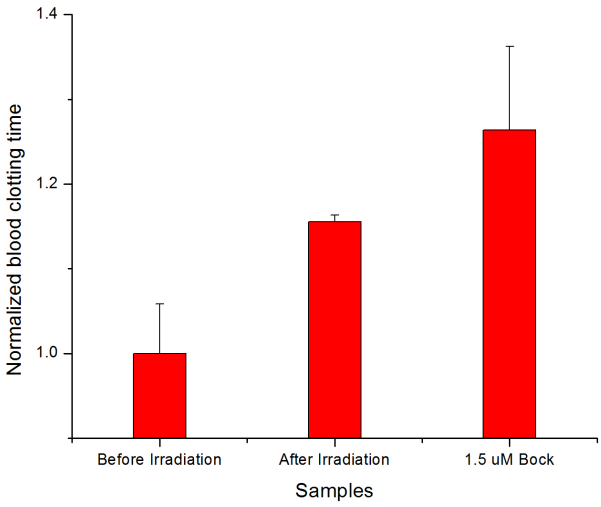

Figure 4-16. Functionality of the released TBA

4.3.4. Effect of NPs in blood clotting time

We also tested the effect of the presence of NPs directly in blood. 12nM NRs with different surface chemistries were introduced to blood, and clotting time was monitored.

We could observe that the presence of NPs increased normal blood clotting time (Fig. 4-17, dashed line). NRs without DNA payloads (NR-MHA) increased clotting time by 23%, while NRs that were coated with thiolated T_{15}-TBA, caused an increase in tclot of 27%, and thiolated TBA caused an increase of 30% in tclot. We can observe that the increase in clotting time due to the presence of TBA was only a 5-7%. If particles were blocked with HSA before the addition into blood, the increases in clotting time resulted 13% and 17% for thiolated T_{15}-TBA and thiolated TBA respectively (Fig. 4-17).

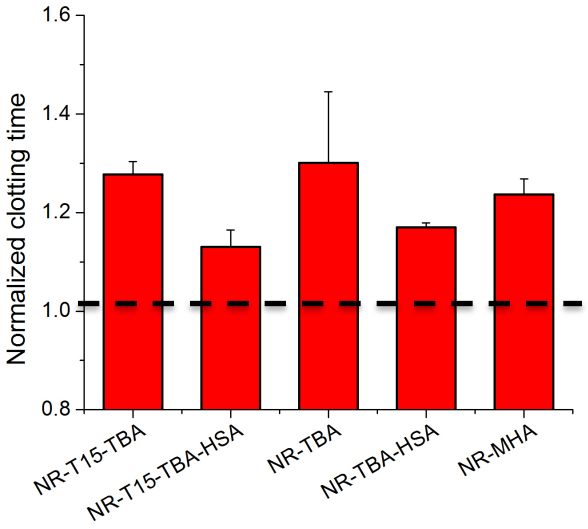

Figure 4-17. Effect of thiolated TBA-NRs in blood

4.4. Release of dsDNA from NRs

It has been observed that by continuous laser irradiation (CW laser), it is possible to heat the NRs without melting them[6, 16], but still release species on the surface that are not covalently linked. We decided to test the dehybridization of dsDNA on the surface of NRs though heating the NRs by CW laser irradiation. Dehybridization of DNA on NP surfaces has been previously studied[17]. Also, in Chapter 3.4, on the hybridization of the DNA on the NPs, we measured the melting temperatures of the DNA bound on the surface of NPs. We see that by CW laser irradiation, the surface temperature of the NRs will need to reach at least 39^{o}C for the dehybridization to occur (Chapter 3, Fig. 3-33).

We hybridized TBA (Fig. 4-18, red ssDNA) with thiolated T_{15}-antidote (Fig. 4-18, bue ssDNA), and bound the dsDNA to the NRs by thiol conjugation. By heating the NRs with a CW laser centered at 800nm, we were able to dehybridize the TBA from the NRs- thiolated T_{15}-antidote (Fig. 4-18). Loading on the NRs was lower than monolayer coverage of ssDNA, due to the larger size of dsDNA[15].

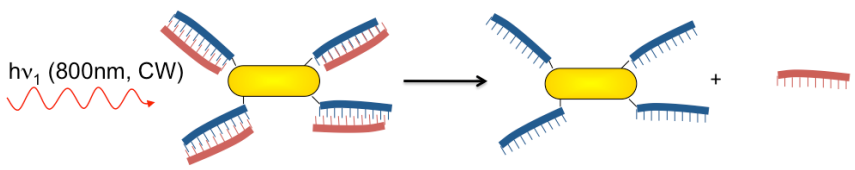

Figure 4-18. Scheme of CW irradiation

We irradiated a 0.8nM solution of the NRs with a CW laser, and measured the release after 1min and 5min irradiation. We confirmed that the NRs did not melt by observing that their absorbance spectra was the same before and after irradiation (Fig. 4-19).

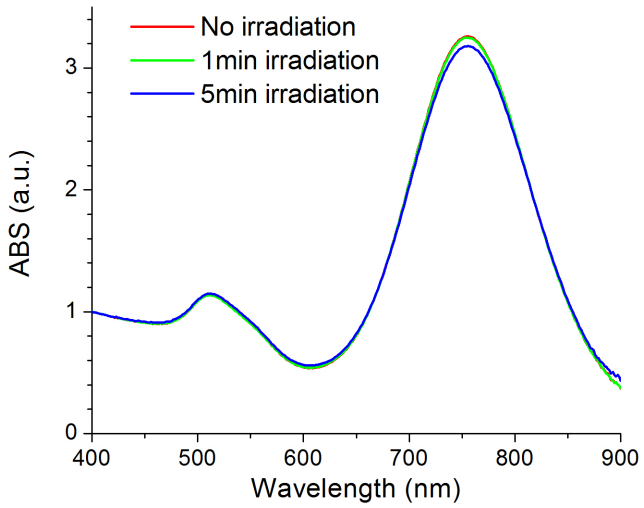

Figure 4-19. Absorbance of CW irradiated NRs

We could measure 12nM thiolated T_{15}-antidote and 63.4nM TBA released from the NRs after 1 min irradiation, reaching 22% and 40% payload release, respectively; and 10nM thiolated T_{15}-antidote and 60nM TBA after 5 min irradiation, showing that irradiation times longer than 1 min were not necessary to achieve release. The percentage of DNA released was approximately double for the TBA than the thiolated T_{15}-antidote, indicating that TBA was preferentially released (Fig. 4-20). Thus, at these laser powers

and irradiation times, dehybridization of the DNA was favored over breakage of the thiol bond.

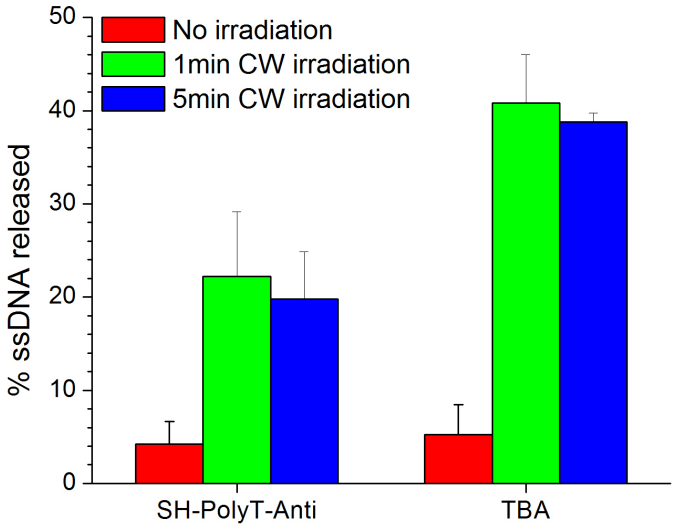

Figure 4-20. Released TBA and thiolated T_{15}-antidote after 800nm CW laser irradiation

Although CW laser irradiation can be used to release species on the NRs, the selectivity of the release is not as good as for ssDNA conjugated NRs excited by the fs laser.

4.5. Conclusions

It is possible to selectively melt NRs and NBs, both separately and in mixtures. We observed a small melting of the NRs after the 1100nm irradiation due to the linewidth of the output of the 1100nm laser. Therefore, we decided to bind the TBA to the gold nanorods, to obtain a very specific on switch to control blood clotting, and bind the antidote on the NBs, that will be excited with the 1100nm laser. We can increase the loading of TBA on gold nanorods, by taking advantage of the intramolecular G-quadruplex structure of TBA. Nevertheless, we have observed that the concentration of NPs in order to release the amount of TBA necessary to control blood clotting is very high, and this leads to several disadvantages. First, a 12nM solution of NRs is very dark and viscous. It absorbs light very strongly, and does not enable for a high yield of release of the bound TBA. Second, we were able to observe that the functionality of the TBA after the laser irradiation was only 64%. In order to overcome these two limitations, we decided to further enhance the amount of TBA bound on the particles, and consequently enable the use of nanoparticles at a lower concentration. We decided to use protein coronas to enhance the loading on the NRs and NBs.

4.6. Bibliography

[1] Alper JD, Crespo M, Hamad-Schifferli K. Release mechanism of octadecyl rhodamine B chloride from Au nanorods by ultrafast laser pulses. Journal of Physical Chemistry C 2009;115:5967.

[2] Huang XH, Jain PK, El-Sayed IH, El-Sayed MA. Plasmonic photothermal therapy (PPTT) using gold nanoparticles. Lasers in Medical Science 2008;23:217.

[3] Wijaya A, Schaffer SB, Pallares IG, Hamad-Schifferli K. Selective Release of Multiple DNA Oligonucleotides from Gold Nanorods. ACS Nano 2008;3:80.

[4] Braun GB, Pallaoro A, Wu GH, Missirlis D, Zasadzinski JA, Tirrell M, Reich NO. Laser-Activated Gene Silencing via Gold Nanoshell-siRNA Conjugates. Acs Nano 2009;3:2007.

[5] Pissuwan D, Valenzuela SM, Cortie MB. Therapeutic possibilities of plasmonically heated gold nanoparticles. Trends in Biotechnology 2006;24:62.

[6] Chen CC, Lin YP, Wang CW, Tzeng HC, Wu CH, Chen YC, Chen CP, Chen LC, Wu YC. DNA-gold nanorod conjugates for remote control of localized gene expression by near infrared irradiation. Journal of the American Chemical Society 2006;128:3709.

[7] Link S, Burda C, Mohamed MB, Nikoobakht B, El-Sayed MA. Laser photothermal melting and fragmentation of gold nanorods: Energy and laser pulse-width dependence. Journal of Physical Chemistry A 1999;103:1165.

[8] Huschka R, Barhoumi A, Liu Q, Roth JA, Ji L, Halas NJ. Gene Silencing by Gold Nanoshell-Mediated Delivery and Laser-Triggered Release of Antisense Oligonucleotide and siRNA. Acs Nano 2012;6:7681.

[9] Alpert J, Hamad-Schifferli K. Effect of Ligands on Thermal Dissipation from Gold Nanorods. Langmuir 2010;26:3786.

[10] Link S, Burda C, Nikoobakht B, El-Sayed MA. Laser-induced shape changes of colloidal gold nanorods using femtosecond and nanosecond laser pulses. Journal of Physical Chemistry B 2000;104:6152.

[11] Jain PK, Qian W, El-Sayed MA. Ultrafast cooling of photoexcited electrons in gold nanoparticle-thiolated DNA conjugates involves the dissociation of the gold-thiol bond. Journal of the American Chemical Society 2006;128:2426.

[12] Huang WY, Qian W, El-Sayed MA, Ding Y, Wang ZL. Effect of the lattice crystallinity on the electron-phonon relaxation rates in gold nanoparticles. Journal of Physical Chemistry C 2007;111:10751.

[13] Link S, Burda C, Nikoobakht B, El-Sayed MA. How long does it take to melt a gold nanorod? A femtosecond pump-probe absorption spectroscopic study. Chemical Physics Letters 1999;315:12.

[14] Link S, El-Sayed MA. Spectroscopic determination of the melting energy of a gold nanorod. Journal of Chemical Physics 2001;114:2362.

[15] Hill HD, Millstone JE, Banholzer MJ, Mirkin CA. The Role Radius of Curvature Plays in Thiolated Oligonucleotide Loading on Gold Nanoparticles. Acs Nano 2009;3:418.

[16] Huang YF, Sefah K, Bamrungsap S, Chang HT, Tan W. Selective Photothermal Therapy for Mixed Cancer Cells Using Aptamer-Conjugated Nanorods. Langmuir 2008;24:11860.

[17] Jin RC, Wu GS, Li Z, Mirkin CA, Schatz GC. What controls the melting properties of DNA-linked gold nanoparticle assemblies? Journal of the American Chemical Society 2003;125:1643.

5. Increasing loading capacity: NR coronas

5.1. Introduction

When NPs are introduced to biological fluids such as media, serum, and blood, coronas made of proteins and other small biomolecules form on the NP surfaces. Since the protein corona is the last layer on the NP surface, it gives the particles a biological identity[1, 2], as it is the layer that will ultimately interact with the biological system. The protein corona is multi-layered, and formed by non-covalent interactions, with a gradient of binding energies [3]. The properties and composition of the protein corona change with time[4], therefore, it is difficult to characterize and predict[5]. The protein corona masks the surface of the NPs, and therefore can prevent the interaction of antibodies, ligands or aptamers attached to the NPs[6, 7]. Many have tried to modify the surfaces of the NPs, to give them non-fouling properties, however, so far the corona formation is inevitable.

Important advances in understanding corona composition and behavior have been made[5, 8]. While the particles have varied in different studies, the key finding is that certain classes of proteins bind strongly to the NPs making up the “hard corona,” while others have a weaker interaction with the surface, forming the “soft corona”[3, 9]. Serum

albumin does not form the bulk of the corona surrounding a NP in serum despite being the most abundant species. Because the corona completely masks the surface of the gold nanoparticles, there is no need for CTAB exchange, as the corona covers it[10]. These advances in understanding protein corona enable us to manipulate its properties and optimize it for a particular biological application.

Because protein coronas are large and multi-layered, they have a high capacity for loading payloads that interact with the proteins in the corona[10]. In the case of gold NRs, the protein corona can have a capacity 6x higher than would be accomplished by covalent binding. Thus, NR-coronas are unique carriers with enhanced physical and biological properties for improving delivery. However, different modes of payload release are desired depending on the delivery application; in this study we aim to have no release of the payloads until there is an excitation by a laser source. However, in some applications it is interesting to achieve a specific passive release profile of the payload. In this chapter, we will map the passive release rates of ssDNA from protein coronas, as well as understanding and minimizing leakage until the laser irradiation triggers the release of the ssDNA.

5.2. Characterization methods for NR-coronas

We formed and loaded coronas around three types of NPs: CTAB coated gold NRs, NBs and CNTs, using serum proteins. The payload was a 20 base long DNA oligo tagged with a fluorophore (sequence 5' CAG CGT GCG CCA TCC TTC CC -TMR), as it does not have a secondary structure, as compared to TBA. Coronas were formed around the NRs using a previously published approach [10]. In summary, we achieved loading of ssDNA on the NR-coronas by incubating the payload either with the NPs and serum proteins simultaneously (combined assembly) or after the NP-coronas were formed (sequential assembly) (Fig. 5-1).

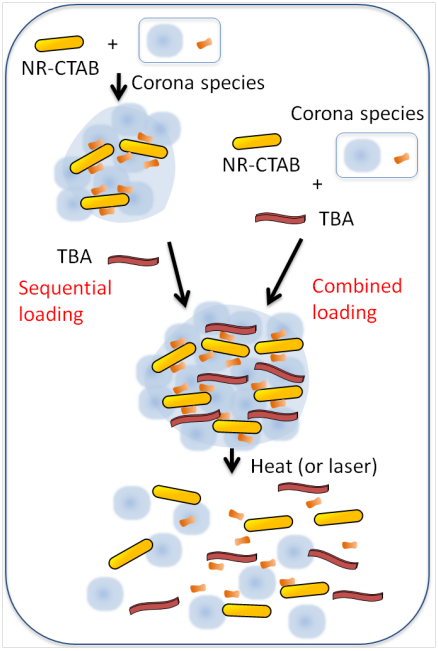

Figure 5-1. Scheme of combined and sequential assembly

NR-coronas were characterized by a number of techniques, namely, TEM, DLS, Zeta potential and absorbance spectroscopy. Loadings were calculated by either (1) heat displacement of the ssDNA from the NR-coronas or (2) by measurement of the unbound ssDNA (supernatant loss), and measured by fluorescence spectroscopy of the fluorophore tags on the ssDNA.

Optical characterization of both NR-HS-DNA (Fig. 5-2, top) and NB-HS-DNA (Fig. 5-2, middle) showed that the longitudinal surface plasmon resonance (SPR) of the NRs was still visible, with a minor red shift and slight broadening over the CTAB-NRs (Fig. 5-2, top). Red shifts and broadening of the SPR indicates that the NRs and NBs are clustering close to one another as the corona is formed. Both CNT-HS-DNA and CTAB-CNTs, however, showed absorption spectrum typical of Mie scatterers due to the lack of SPR in CNTs (Fig. 5-2, bottom).

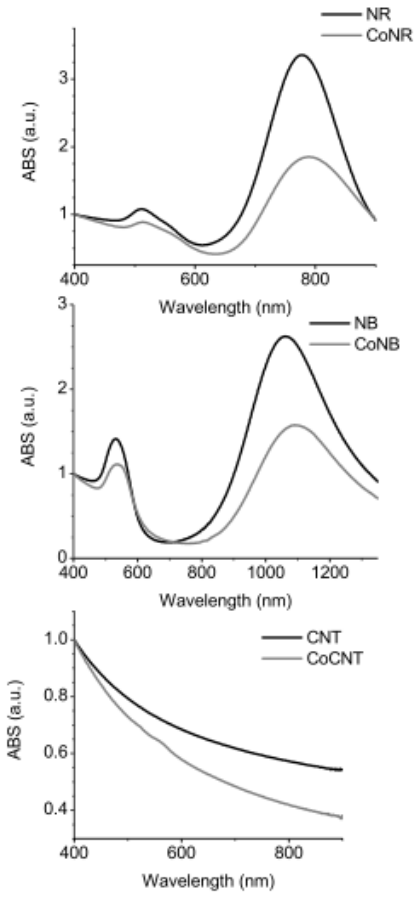

Figure 5-2. Absorbance spectra of the protein coronas

TEM images of all three types of NP-HS-DNA show a large, diffuse agglomerate containing many NPs, confirming that there is not one but many NP in a corona (Fig. 5-3).

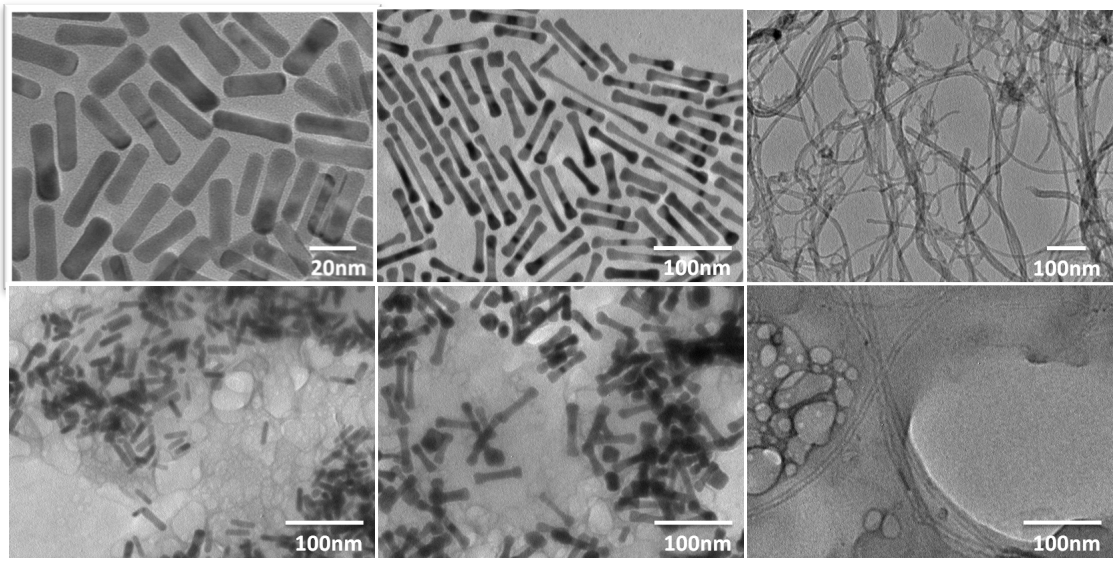

Figure 5-3. TEM images of NR, NB, CNT and CoNR, CoNB, CoCNT

Zeta-potential measurements of all three positively charged NPs show that as the NP-corona are formed; they adopt a negative charge (Fig. 5-4, bottom) due to the negative species that compose HS. DLS showed that when coronas are formed of HS, a larger species results. NRs have a $D_H = 32 \pm 15$ nm which increases to $D_H = 553 \pm 33$ nm with HS corona formation. The increase in D_H is also observed for NBs and CNTs (Fig. 5-4, top). These size increases suggest that HS can form large coronas around a cluster of multiple NPs.

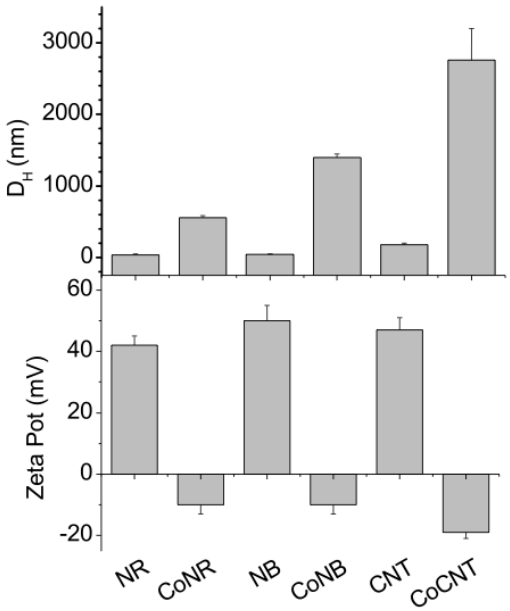

Figure 5-4. DLS measurements (top) and Zeta potentials (bottom) of NR, NB, CNT and CoNR, CoNB, CoCNT

5.3. Optimizing the protein corona

5.3.1. Different binding strategies and proteins

We first tested the formation of protein coronas using human serum (HS), human serum albumin (HSA) and equine serum (ES). The composition of the protein corona around nanoparticles of polymers, silica, gold, and other materials has been characterized by mass spectrometry and other techniques. It has been found that opsonins and apolipoproteins (ApoA1, etc.) bind strongly to the NP to constitute the "hard corona" [11] and are difficult to be removed. Surprisingly, the corona surrounding NPs does not have a high abundance of albumin, despite albumin making up nearly half of human serum. Instead, some studies have observed that human serum albumin (HSA) binds weakly to the NPs[12-14], making up the "soft corona." Corona composition varies with particle type, size, and surface chemistry[15], but in general, these two classes of corona proteins are generally observed.

We prepared protein coronas using the combined approach (CoNR) and the sequential approach (SeNR). We could observe that the particles behave differently depending on the type of protein added and the preparation method. In figure 5-5 we can observe the CoNR prepared with HS, ES and HSA (from left to right).

Figure 5-5. Variation of the corona components

For each of the corona formation strategies and proteins we measured both the absorbance of the particles and the DNA loading per NR. The combined loading strategy consisted in preparing 1mL of 1nM NRs, and after centrifugation, resuspending the remaining 20µl of concentrated NRs into 1ml of 1µM ssDNA, 5%HS and 5mM PB.

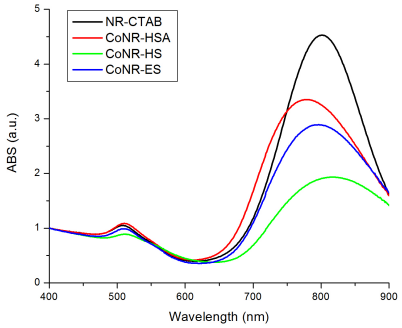

Figure 5-6. Absorbance of NR-coronas

In the combined approach, we can observe that the CTAB-NR (Fig. 5-6, black), are not aggregated, and after the addition of proteins + ssDNA, there is aggregation of the

particles (seen as a decrease in the absorbance ratio ABS800/ABS400). Initially, the NR-CTAB had an absorbance ratio of 4.4±0.17 and a SPR peak at 796±5.7nm (Fig. 5-6, black). We could observe that HSA was the protein that caused the lowest aggregation on the particles showing an absorbance ratio of 3.08±0.28, and SPR max at 783±5.2 (Fig. 5-6, red), while HS is responsible for the highest aggregation with an absorbance ratio of 1.77±0.32, and SPR max at 808±9.5 (Fig. 5-6, green). As for equine serum, the absorbance ratio was 2.48±0.79, and SPR max at 796±10 (Fig. 5-6, blue). With all three loading coronas, the SPR is still visible, which indicates that it is still possible to excite the NPs with a laser.

We also prepared the protein coronas by using the sequential approach. In order to do that, 1ml of 1nM NRs, were centrifuged and resuspended in 5% serum proteins, 5mM PB and incubated for 4h at 37ºC. After, NR-Coronas were washed twice in 5mM phosphate buffer, and resuspended in 1uM ssDNA, followed by overnight incubation at 37ºC.

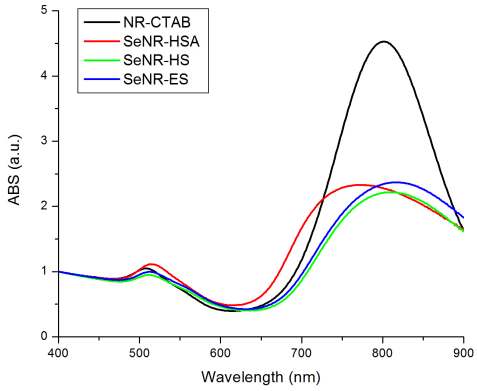

Figure 5-7. Absorbance of SeNR

By sequential loading, all the NRs had similar absorbance ratios. HSA-NRs had an absorbance ratio of 2.41±0.18, and a SPR peak at 777.5±6.36nm (Fig. 5-7, red). HS-NR had an absorbance ratio of 2.17±0.05 and the SPR peak was at 805±5.66nm (Fig. 5-7, green). Finally, the ES-NR had an absorbance ratio of 2.36±0.03 and an SPR peak at 805±18.4nm (Fig. 5-7, blue).

We then measured the loading on the NPs by supernatant loss -centrifuging the particles and measuring the amount of DNA that was not bound in order to calculate an approximate loading on the particles-. DNA concentration was measured by fluorescence spectroscopy of the fluorophore tag bound to the ssDNA. Measuring ssDNA loadings by supernatant loss showed similar results for all kinds of coronas (Fig. 5-8), but

overestimates the loading on the NRs, as ssDNA could be potentially released during the subsequent washes of the NPs.

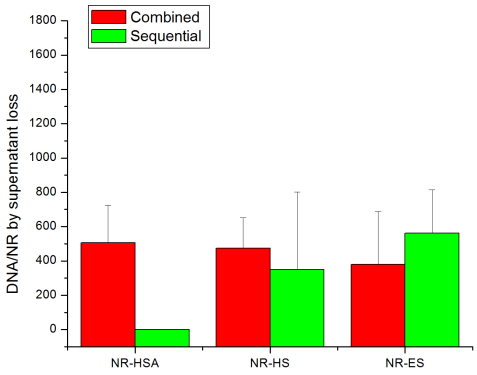

Figure 5-8. Loading from coronas as measured by supernatant loss

In order to confirm these results, we also heated the conjugated NRs at 90^{o}C for half hour and measured the fluorescence of the tagged ssDNA that could be released by heat displacement. While high temperature is able to disassemble the corona to release both HS and DNA, we note that heating does not displace the entire payload in the corona as was found previously[10]. Also, the amount of serum and payload released by heat displacement changes with time and underestimates the DNA loading. A more accurate quantification would require combining several techniques including chemically dissolving the NPs, displacing the proteins in the corona by detergents, etc. However, we have found thermal displacement to give consistent readings if the conditions are kept the

same, hence all measurements were done consistently to allow comparison. While HS, ES and HSA can form a corona around NPs, their ability to carry a DNA payload are very different. We note that the error bars are large compared to covalent attachment strategies, due to the complex nature of corona formation, as it involves non-covalent interactions between multiple species and it can undergo a constant dynamic exchange with its surrounding media.

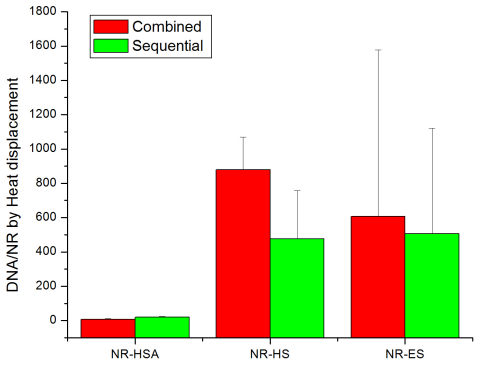

Figure 5-9. Loading of NR-coronas measured by heat displacement

We observe that both the ES and HS can yield high loading of payload on the NPs (>400 DNA/NP, Fig. 5-9), as they are comprised of mixtures of proteins, some of which are strong binders to the NPs. In contrast, we can observe that the HSA does not yield high loadings of ssDNA on the NPs (~0 DNA/NP), showing that even if HSA is in high concentration in serum, it is not a strong binder to the NRs, and confirms that HSA

does not bind strongly to the NRs, and it forms the weak corona. Even though a corona still forms, as evidenced by the increase in size by DLS (Fig. 5-10), the corona formed from HSA is clearly not suitable for loading DNA. Based on these results, it appears that other components in the HS, rather than HSA, are responsible for holding the corona and DNA payload together.

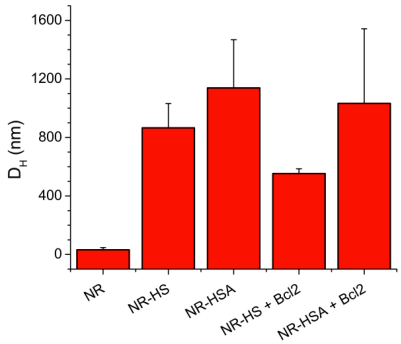

Figure 5-10. DLS of coronas formed with HS, ES and HSA

Initially, NR-CTAB have a D_H of 32nm, which increases after proteins start to form the corona around the NRs. NR-HS have a D_H of 865nm, and NR-HSA have a larger D_H (1138nm). In both cases, when the ssDNA is loaded with the HS, D_H decreases yielding 553nm and 1033nm for the NR-HS-ssDNA and NR-HSA-ssDNA, respectively (Fig. 5-10), indicating that the ssDNA and the proteins could be competing for the positively charged surface of the NPs.

5.3.2. 5/5/5 Optimal Conditions

We can further optimize the loading of ssDNA on the HS-loaded coronas by tuning the phosphate buffer (PB) concentration, CTAB concentration and HS concentration in the preparation solution. Tests were performed using the combined approach, as it gives more consistent loadings on the coronas, and with Human Serum (HS) as human serum proteins are already present in blood, and it enables for enhanced loading, as compared to HSA and ES.

5.3.2.1. Effect of phosphate buffer

We explored the effect of environmental factors on the loadings of NR-coronas. It has previously been shown that ssDNA loading varies with [PB], so charge screening of the electrostatic interactions between the DNA, corona proteins, and NRs can impact how much DNA is loaded. We prepared protein coronas with increasing concentrations of PB, and observed that 5mM PB is the optimal concentration in order to achieve a high loading of ssDNA on the protein coronas (Fig. 5-11).

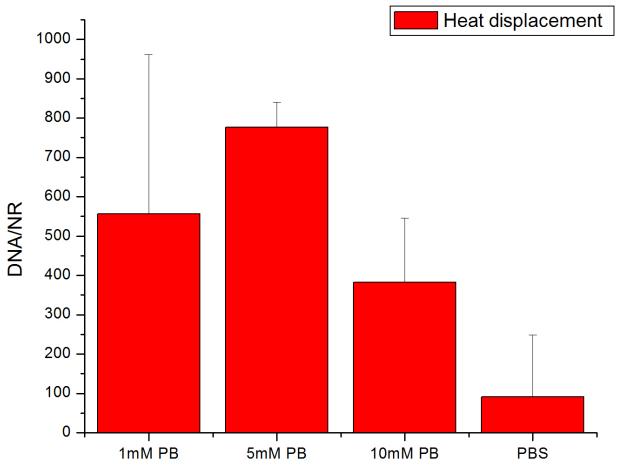

Figure 5-11. Loading of CoNRs, as a function of [PB]

We could also observe that the aggregation of the particles was dependent on the PB concentration. Increasing the PB concentration led to more stable particles, while decreased PB concentrations led to larger aggregates, as increased salt concentration leads to a diminished Debye length. We can observe in figure 5-12, in which the concentration of PB varies (from left to right) from 10mM PB, 20mM PB and PBS. However, large aggregates could be resuspended by sonication of the particles for 3min.

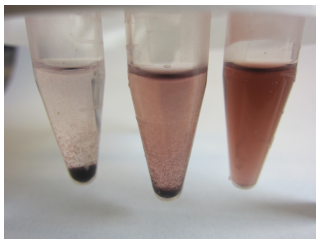

Figure 5-12. Stability of NR-coronas in different buffer strengths and buffers.

5.3.2.2. Effect of CTAB concentration

Since the positively charged CTAB is weakly bound to the NR/NB/CNT and can exist freely in dynamic flux with the CTAB on the NP's surface, the free CTAB can interact and form complexes with both DNA and the negatively charged corona proteins and be intimately involved either in facilitating corona formation on the NP surface or even avoiding it due to the possible formation of these new stable micelles. The concentration of CTAB on the NR solution was varied as well. NRs were prepared in increasing concentrations of CTAB, and then centrifuged. The pellet was resuspended in 1ml of 5%HS, 5mM PB; and the loadings of the particles were measured (Fig. 5-13). Initially, NRs were suspended in 0.5mM CTAB, 1mM CTAB, 5mM CTAB and 10mM CTAB, and the final CTAB concentrations in solution were approximately 0.01mM, 0.02mM, 0.1mM and 0.2mM CTAB after the dilutions, therefore, in all cases, the final CTAB concentrations were lower than the critical micelle concentration (cmc) of CTAB (cmc_{CTAB}=1.2mM[16, 17]), which indicates that no micelles of CTAB are present in the coronas. Thus, the only parameter that was varied is the concentration of free CTAB, and CTAB bound to the NPs. NRs are poorly passivated below the cmc, and well passivated above the cmc [10, 18]. Free CTAB plays a role in corona formation, at [CTAB] = 0.5 mM, which is below the cmc_{CTAB}, there was poor loading arising from poor corona formation (Fig. 5-13). At 1 mM of CTAB, which is approximately the

cmc_{CTAB}, loading of DNA was higher, and it continued to increase until a peak at [CTAB] = 5 mM. This shows that the concentration of CTAB can also be used to tune the loading of ssDNA on NR-HS-DNA.

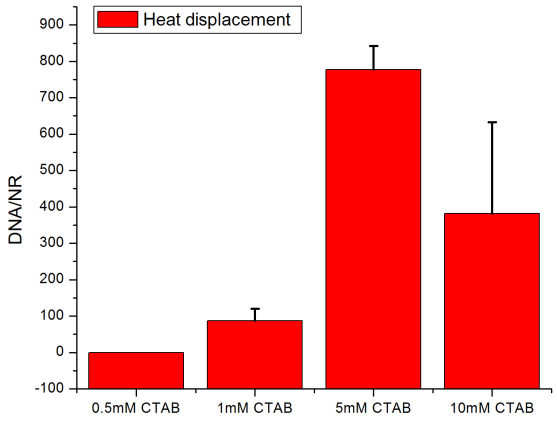

Figure 5-13. Loading of the NRs as a function of CTAB concentrations

5.3.2.3. Effect of HS concentration

The concentration of HS used in the corona formation and loading of DNA on the NR also appeared to affect the loading of payload. We varied the [HS] from 1 to 20% during corona formation and found that the loading was low at 1% HS and peaked at for 5% HS. At higher concentrations of HS, the loading decreased for 10%HS coronas, until it became negligible at 20% HS (Fig. 5-14), showing that it is possible to find an optimum for loading of ssDNA on the NR-coronas. At 1% HS, there is not enough serum to stabilize the coronas, and therefore loading is not achieved, and at 20%HS there may be

protein coronas (mostly negatively charged) that may be competing with the ssDNA to bind to the surface of the NRs.

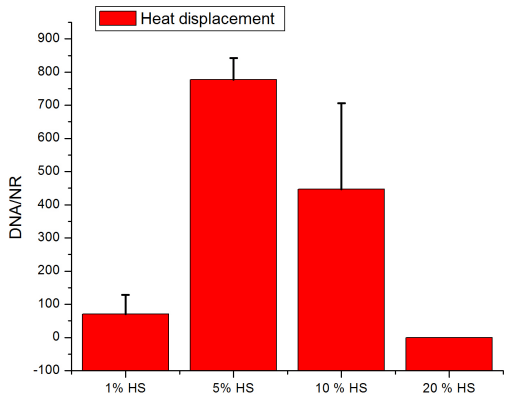

Figure 5-14. Loading of the NRs as a function of HS concentrations

5.3.3 Effect of particle material on loading

We tested different types of NPs and tested the loading that could be achieved by using the "5/5/5" (PB concentration (mM)/ CTAB concentration (mM) /HS%) optimal conditions, with the combined assembly approach. We chose NPs relevant for biological applications: gold nanorods (NRs), gold nanobones (NBs) and carbon nanotubes (CNTs).

We could observe an increase in D_H that indicated that the coronas were formed with the three types of particles (Fig. 5-4). Loadings per nanoparticle were measured as well. NB-HS-DNA had 710 ± 130 DNA/NB. This loading, as well as the loading density per surface area (give a 0.2 DNA/nm^2) is lower compared to NR (777 ± 64 DNA/NR, 1

DNA/nm^2) given the larger surface area per NB. CNT-HS-DNA had $17{\cdot}10^5 \pm 7{\cdot}10^5$ DNA/CNT (Fig. 5-15). Even with normalization to the estimated larger surface area of the CNTs, this loading density (7 DNA/nm^2) is much higher than what was achieved for the NRs and NBs. These results show that coronas can be formed and loaded with DNA on different NPs, though their actual surface area-normalized loading density differed.

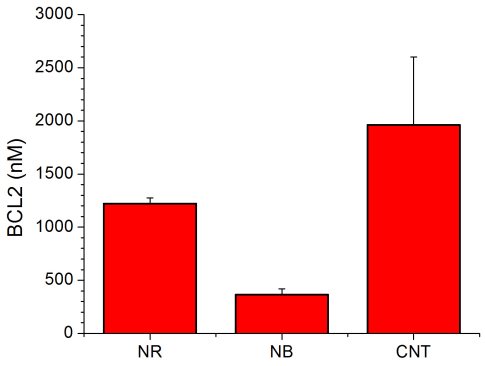

Figure 5-15. Loading of the NRs, NBs and CNTs

All these results with different NPs show that the surface effects e.g. surface area and surface coating ligand play a dominant role in influencing corona formation and loading, as opposed to the identity of the NP material. We note that because the concentration of free CTAB in each of the NPs is difficult to control, the NRs, NBs and CNTs may have different concentration of free CTAB, which would explain the slight differences in loadings in each of the three types of NPs.

5.4. Kinetics of formation of the protein coronas

By monitoring the kinetics of formation of protein coronas we were able to see a decrease in their AR, indicating that particles were interacting and coming within proximity of one another (Fig. 5-16). We also observed the appearance of an isosbestic point ~740nm during the corona formation, which indicated that throughout the reaction there was equilibrium between the particles in and out of the corona.

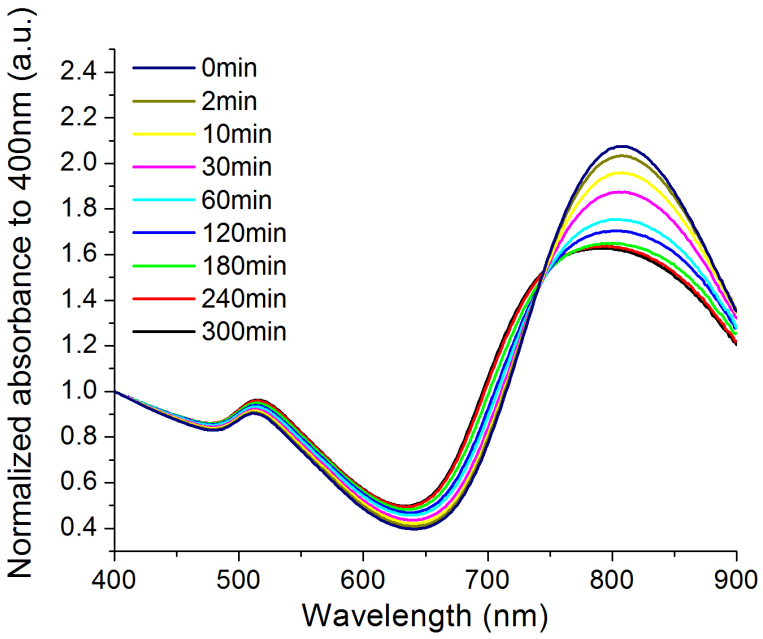

Figure 5-16. Formation of the protein coronas

5.5. Leakage from the NR-coronas

Because protein coronas are made of a number of non-covalent interactions, we tested the leakage from protein coronas after their formation. In order to do that, we measured the amount of ssDNA in the supernatant -released from the coronas- during a period of two weeks. Previously we found that by tuning the formation of the protein coronas it was possible to tune the loading on them. We found that it is also possible to tune the leakage from the protein coronas by changing the environmental conditions of the NPs.

The first factor we examined to tune the passive release is the effect of free CTAB concentration around the NRs before the coronas were formed. As it has been previously commented, the CTAB exists in a state of dynamic flux between being free in solution or passivating the NP surface. The critical micelle concentration of CTAB is cmc_{CTAB} = 1.2 mM [16, 17]. We have observed that the NRs are poorly passivated below the cmc, and well passivated above the cmc [10, 18] suggesting that the free CTAB plays a role in corona formation (Chapter 5.3.2.2) and hence the passive release profile. At [CTAB] = 0.5 mM, which is below the cmc_{CTAB}, there was minimal passive release of DNA observed, due to poor loading on the coronas (Fig. 5-13). At 1 mM of CTAB, which is approximately the cmc_{CTAB}, passive release of DNA was higher, and the release continued to increase until a peak at [CTAB] = 5 mM. This shows that the

concentration of CTAB can also be used to tune the passive release of DNA from NR-HS-DNA (Fig. 5-17, top). Nevertheless, CTAB did not change the low release profile during the first 4 days.

The concentration of HS used in the corona formation and loading of DNA on the NR also affected the passive release of payload. We varied the [HS] from 1 to 20% and found that the passive release after 15 days was low at 1% HS (300 ± 70 DNA/NR), before peaking at 700 ± 90 DNA/NR for 5% HS. At higher concentrations of HS, the passive released amount decreased (200 ± 140 DNA/NR for 10%HS coronas), where it became negligible at 20% HS (Fig. 5-17, middle). This non-monotonic passive release profile for [HS] is also similar to the loading profile from our earlier study (Chapter 5.3.2.3), where the loading also peaked at 5% HS and decreased with higher [HS]. This shows that the concentration of HS used to form the corona and load DNA can also be used to tune the passive release of payloads from corona.

Previously we found that charge screening of the electrostatic interactions between the DNA, corona proteins, and NRs can impact how much DNA is loaded [10]. We thus expect that tuning [PB] and therefore charge screening will also affect passive release amounts. The non-monotonic passive release profile (Fig. 5-17, bottom) is similar to the

loading profile in our previous study, with peak passive release occurring at 5 mM PB, showing that charge screening influences the integrity of the protein corona.

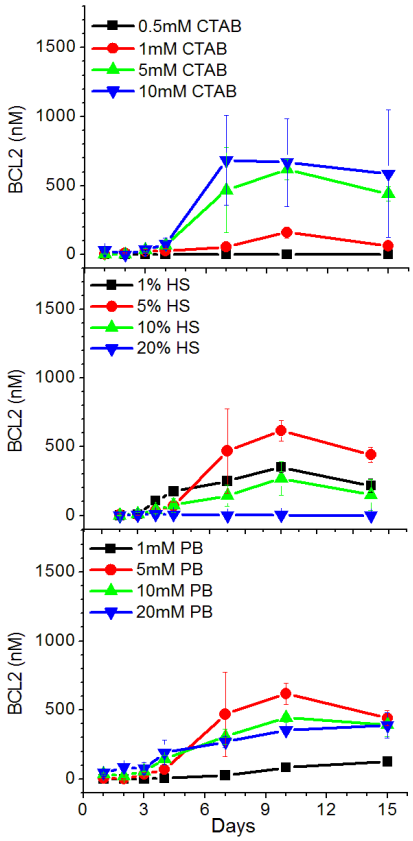

Figure 5-17. Leakage from NP-coronas, by tuning corona formation

The coronas around NPs are known to change when the NPs are placed in different environmental conditions. We explored the effect of making the NR-HS-DNA coronas in one phosphate buffer condition, before placing them in a new condition with different

ionic concentration. NR-HS-DNA were formed in [PB] = 5mM and then release profiles were measured in [PB] = 1mM, 5mM, 10mM, and 1X PBS. The release profile in 1 mM and 10 mM PB (Figure 5-18, black and green respectively) showed the same initial 3 day lag for coronas made and released in 5 mM (Fig. 5-18, red). For example, coronas made in 5 mM and then released in 1mM have release profiles in between those exposed only to 1 mM (Fig. 5-17, bottom, black) and those exposed only to 5 mM (Fig. 5-18, red). This shows that when the coronas are formed in one PB concentration and then used for release in another, the release profile retains some of its original release properties. Thus, the corona has some resilience and can be maintained in different buffer solutions. The release profile in 1X PBS showed that the lag was gone (Fig. 5-18, blue), indicating that the increase in charge screening affected the corona integrity.

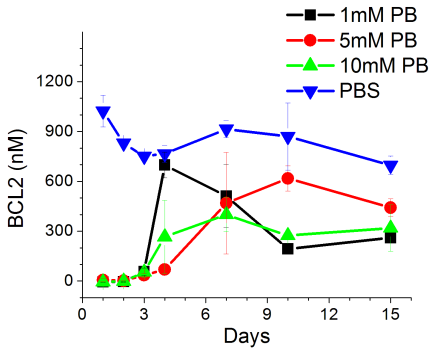

Figure 5-18. Changing the PB after formation of coronas

We next tested the ability of hard and soft corona proteins to block and minimize passive release of DNA from the NR-coronas. As we have previously commented, HSA could be a good blocking agent, as it forms coronas on the NPs but is not able to hold payload. We formed NR-HS-DNA by combined assembly and attempted to "block" their surface with either HS or HSA. We compared passive release of the DNA from NR-HS-DNA that were blocked by HS or HSA to NR-HS-DNA that were not blocked. Blocking was achieved by incubating NR-HS-DNA with additional HS or HSA, and then subsequent removal of free protein. Release from the blocked coronas was quantified by measuring the DNA in the supernatant as a function of time.

In the absence of blocking, NR-HS-DNA show little release of DNA in the first 4 days (Fig. 5.19, a, black), but released increased afterwards, with a large release at Day 7. The initial 3 – 4 day lag was observed previously for NRs coated with coronas of equine serum[10]. This could be due to the gradual hardening of the corona with time after its initial formation [4], which tends to hold the payload and thus slow the release rate. This initial lag is beneficial for laser triggered release experiments, where the corona can be used to hold the payload within the first three days without significant passive release.

The kinetics of the release changed with the use of different blocking agents on NR-HS-DNA. If the NR-coronas were blocked with soft corona proteins HSA, the amount of

payload released was lower (Fig. 5-19, a, green) compared to release from corona in the absence of blocking. This indicates that there was little protein exchange between HSA and proteins in the HS corona, and that the HSA was able to block and thus minimize the passive release from the corona. However, if blocking was attempted using HS, significant protein exchange would occur between the free HS proteins and those in the corona, resulting in ineffective blocking and significantly higher release of payloads in the first 4 days (Fig. 5-19, a, red). In fact, around 20 % (264 ± 83 DNA/NR) of payload was passively released at day 1. This confirms our earlier postulation that there are other protein components in HS apart from HSA that are perturbing the corona to release more payload. These protein components are most likely the "hard corona" proteins in HS that are able to exchange with the "hard corona" proteins on the NR because of similar binding affinity to the NRs. We have thus demonstrated that the selection of proteins can provide us with a handle to control the payload release rate.

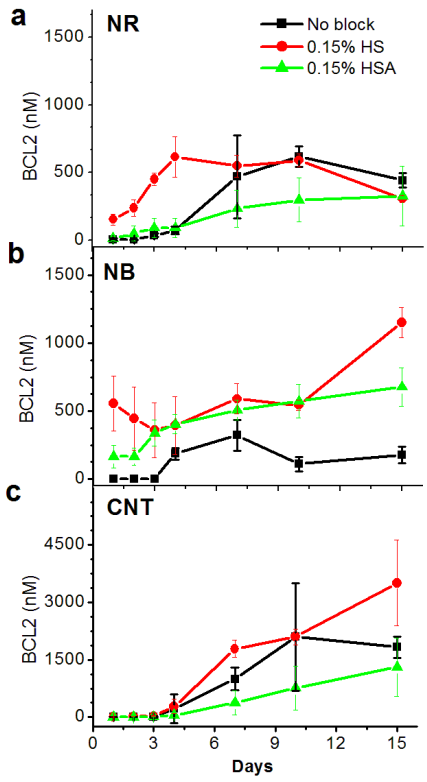

Figure 5-19. Formation of the protein coronas

The unblocked NB-HS-DNA passively released DNA with a profile similar to the NRs, starting with negligible release in the first 3 days and then increasing with time (Fig. 5-19, b, black). However, the use of HSA seemed to increase the amount of DNA released passively on the first days (350 ± 220 DNA/NB or 20 ± 9% of loaded DNA at Day 1) (Fig. 5-19, b, green). This amount is even higher (850 ± 280 DNA/NB or 50 ± 30% of loaded DNA) when HS was used (Fig. 5-19, b, red). While the release profile of NBs was

similar to that of NRs, the amount of released DNA from NBs is generally higher (reaching 70 ± 15% after 15 days with HSA block vs. 30 ± 15% with HSA block on NRs). This shows that the corona formed on larger NBs are apparently more prone to leakage and blocking by HSA is less effective for a leakier corona. As was previously reported, NP size can also influence corona formation[19-21].

CNT-HS-DNA also exhibited similar passive release profiles to NRs and NBs, with generally a higher amount of DNA being passively released with time. The same initial 3-day lag in the passive release was observed for all 3 cases (no blocking, blocking with HSA and blocking with HS), after which the release increased significantly (Fig. 5-19, c). After 3 days, the release amount was least with HSA blocking (Fig. 5-19, c, green), and increased significantly after corona exchange with HS (Fig. 5-19, c, red), similar to observations for NRs.

5.6. Conclusions

These results show that protein coronas can be used for enhanced loading on gold nanoparticles for both triggered release applications (where leaking needs to be minimized until there is an external signal), or for passive release applications. We can strategically tune the properties of NPs in order to enhance the loading by using different concentrations of human serum, CTAB or PB when preparing the coronas.

Exchange of corona proteins can help optimize the carrier properties of coronas surrounding NPs. Hard corona proteins exchange more and result in higher release, while soft corona proteins exchange less and can be used to decrease release. This strategy can be employed different types of nanoparticles, as the ligand on the NP seems to influence the release profiles more than the material identity of the NP. We can use these results to strategically design corona properties for a particular biological application.

5.7. Bibliography

[1] Monopoli MP, Walczyk D, Campbell A, Elia G, Lynch I, Baldelli Bombelli F, Dawson KA. Physical-Chemical Aspects of Protein Corona: Relevance to in Vitro and in Vivo Biological Impacts of Nanoparticles. Journal of the American Chemical Society 2011;133:2525.

[2] Monopoli MP, Aberg C, Salvati A, Dawson KA. Biomolecular coronas provide the biological identity of nanosized materials. Nat Nano 2012;7:779.

[3] Cedervall T, Lynch I, Foy M, Berggård T, Donnelly SA, Cagney G, Linse S, Dawson KA. Detailed Identification of Plasma Proteins Adsorbed on Copolymer Nanoparticles. Angewandte Chemie International Edition 2007;46:5754.

[4] Casals E, Pfaller T, Duschl A, Oostingh GJ, Puntes V. Time Evolution of the Nanoparticle Protein Corona. ACS Nano 2010;4:3623.

[5] Salvati A, Pitek AS, Monopoli MP, Prapainop K, Bombelli FB, Hristov DR, Kelly PM, Aberg C, Mahon E, Dawson KA. Transferrin-functionalized nanoparticles lose their targeting capabilities when a biomolecule corona adsorbs on the surface. Nature Nanotechnology 2013;8:137.

[6] Walczyk D, Bombelli FB, Monopoli MP, Lynch I, Dawson KA. What the Cell "Sees" in Bionanoscience. Journal of the American Chemical Society 2010;132:5761.

[7] Lynch I, Salvati A, Dawson KA. Protein-Nanoparticle Interactions What Does the Cell See? Nature Nanotechnology 2009;4:546.

[8] Pitek AS, O'Connell D, Mahon E, Monopoli MP, Baldelli Bombelli F, Dawson KA. Transferrin Coated Nanoparticles: Study of the Bionano Interface in Human Plasma. PLoS ONE 2012;7:e40685.

[9] Cedervall T, Lynch I, Lindman S, Thulin TBE, Nilsson H, Dawson KA, Linse S. Understanding the nanoparticle–protein corona using methods to quantify exchange rates and affinities of proteins for nanoparticles. Proceedings of the National Academy of Science 2007;104:2050.

[10] Kah JCY, Chen J, Zubieta A, Hamad-Schifferli K. Exploiting the protein corona around gold nanorods for loading and triggered release. ACS Nano 2012:Just Accepted.

[11] Lundqvist M, Stigler J, Cedervall T, Berggård T, Flanagan MB, Lynch I, Elia G, Dawson KA. The Evolution of the Protein Corona around Nanoparticles: A Test Study. ACS Nano 2011;5:7503.

[12] Dell'Orco D, Lundqvist M, Oslakovic C, Cedervall T, Linse S. Modeling the Time Evolution of the Nanoparticle-Protein Corona in a Body Fluid. PLoS ONE 2010;5:e10949.

[13] Treuel L, Malissek M, Grass S, Diendorf J, Mahl D, Meyer-Zaika W, Epple M. Quantifying the influence of polymer coatings on the serum albumin corona formation around silver and gold nanoparticles. Journal of Nanoparticle Research 2012;14:1.

[14] Lacerda SHD, Park JJ, Meuse C, Pristinski D, Becker ML, Karim A, Douglas JF. Interaction of Gold Nanoparticles with Common Human Blood Proteins. Acs Nano 2010;4:365.

[15] You CC, Verma A, Rotello VM. Engineering the nanoparticle-biomacromolecule interface. Soft Matter 2006;2:190.

[16] Bahri MA, Hoebeke M, Grammenos A, Delanaye L, Vandewalle N, Seret A. Investigation of SDS, DTAB and CTAB micelle microviscosities by electron spin resonance. Colloids and Surfaces A: Physicochemical and Engineering Aspects 2006;290:206.

[17] Majhi PR, Moulik SP. Energetics of Micellization: Reassessment by a High-Sensitivity Titration Microcalorimeter. Langmuir 1998;14:3986.

[18] Alper J, Crespo M, Hamad-Schifferli K. Release Mechanism of Octadecyl Rhodamine B Chloride from An Nanorods by Ultrafast Laser Pulses. Journal of Physical Chemistry C 2009;113:5967.

[19] Lundqvist M, Stigler J, Elia G, Lynch I, Cedervall T, Dawson KA. Nanoparticle size and surface properties determine the protein corona with possible implications for biological impacts. Proceedings of the National Academy of Sciences 2008;105:14265.

[20] Tenzer S, Docter D, Rosfa S, Wlodarski A, Kuharev J, Rekik A, Knauer SK, Bantz C, Nawroth T, Bier C, Sirirattanapan J, Mann W, Treuel L, Zellner R, Maskos M, Schild H, Stauber RH. Nanoparticle Size Is a Critical Physicochemical Determinant of the Human Blood Plasma Corona: A Comprehensive Quantitative Proteomic Analysis. ACS Nano 2011;5:7155.

[21] Walkey CD, Olsen JB, Guo H, Emili A, Chan WCW. Nanoparticle Size and Surface Chemistry Determine Serum Protein Adsorption and Macrophage Uptake. Journal of the American Chemical Society 2012;134:2139.

6. Switching on and off blood clotting with light

6.1. Introduction

Nature has engineered the blood clotting cascade to form clots with temporal and spatial precision. Current control of blood clotting is achieved predominantly by anticoagulants and thus inherently one-sided. Here we use a pair of nanorods (NRs) to provide two-way control of the blood clotting cascade by utilizing their ability to selectively release species on their surface under two different laser excitations. We selectively trigger release of a thrombin binding aptamer from one NR, inhibiting blood clotting and resulting in increased clotting time. We then release the complementary DNA as an antidote from the other NR, reversing the effect of the aptamer and restoring blood clotting. Thus, the NR pair acts as an on/off switch. One challenge for nanobiotechnology is the bio-nano interface[1-3], where coronas of weakly adsorbed proteins can obscure biomolecular function. We exploit these adsorbed proteins to increase aptamer and antidote loading on the NRs[4].

Nanotechnology has great potential as an enabling technology for biology because nanoparticles can be designed to interface directly with biomolecules. In particular, external laser excitation of nanoparticles can trigger payload release[5, 6], so

nanoparticles can act as handles for controlling biological processes. Gold nanorods (NRs) have gained considerable interest for therapeutic applications because they can be selectively excited at wavelengths where tissue does not absorb to release multiple species that can impact complex processes, such as gene expression[5, 7-9] so extension to control blood clotting is promising.

Thrombin inhibitors are of great interest as candidates for anticoagulants because thrombin, which cleaves fibrinogen into fibrin to form the clot, is at the apex of the clotting cascade[10, 11]. We used ssDNA thrombin binding aptamers (TBA) to bind and inhibit thrombin and blood coagulation. We then used complementary DNA as an antidote because it can reverse TBA's effect by base-pairing with it (Fig. 6-1). Selective excitation of two different NRs to release TBA and its antidote enables the pair to act as an on/off switch for coagulation. Coronas made from human serum (HS) loaded with NRs and TBA (NR-HS-TBA) + coronas loaded with NBs and antidote (NB-HS-anti) can be irradiated at 800nm, in order to melt the NRs, and release the TBA in order to increase blood clotting time. Following that, 1100nm irradiation can trigger the release of the ssDNA antidote. The antidote and the TBA can form a hybrid, and therefore blood clotting would be restored (Fig. 6-1).

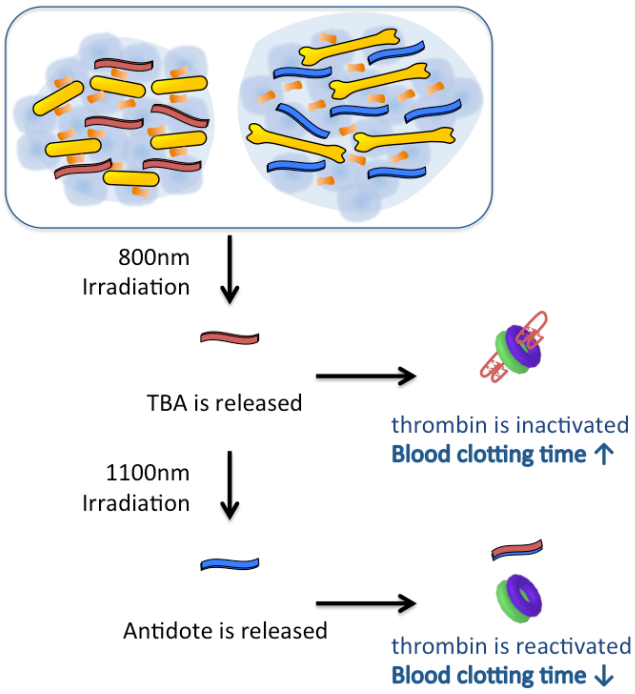

Figure 6-1. Scheme of the selective release approach

One critical challenge for nanobiotechnology is the difficulty of controlling the bio-nano interface. Proteins adsorb on nanoparticles to form coronas[1, 3, 12] that can obscure the function of biomolecules on the nanoparticle surface or result in unpredictable behavior. However, protein coronas can possess beneficial properties, so we used them here to increase DNA loading on the NRs[4].

Here we build upon Chapters 2-5 in order to better engineer NRs as carriers for TBA and antidote. We have observed that coronas can be engineered to load high

concentrations of payload, and that they can be designed to avoid leakage during the first 4 days after preparation (Chapter 5). Moreover, we have observed that thiolated TBA released from NRs retains only 64% functionality (Chapter 4). We aim to take advantage of protein coronas in order to enhance the concentration and functionality of the released TBAs and antidotes.

6.2. Effect of TBA and antidote in thrombin clotting tests

TBA has been identified by SELEX to bind and inhibit thrombin, the protein at the apex of the blood clotting cascade, which cleaves fibrinogen into fibrin, which forms the clot[13, 14]. TBA folds into a double G-quartet and binds to exosite I, so it inhibits activity by preventing fibrinogen binding[15-19]. Thrombin inhibition results in an increase in blood clotting time, t_{plasma}. We verified TBA's ability to inhibit clotting by measuring its effect on t_{plasma} in a thrombin test, with 10nM thrombin[20]. Fluorecently labelled TBA (5' GGTTGGTGTGGTTGG-TMR 3') was added into blood at increasing amounts. Blood with no TBA was normalized as t_{plasma} = 1.0. Increasing TBA concentration increased t_{plasma} (Fig. 6-2, top), indicating that TBA inhibited thrombin and consequently the blood coagulation cascade.

We verified that antidote could reverse TBA's effect. Fluorecently labelled antidote had a sequence of 5' CCAACCACACCAACC-FAM 3'. As antidote:TBA was increased from 0:1 to 2:1, t_{plasma} started at 4.4 and decreased (Fig. 6-2, bottom). Thus, antidote could successfully inhibit TBA by forming a double strand with it and preventing it from folding into the G-quartet structure necessary for thrombin binding (Fig. 1)[20]. $\Delta G_{binding}$ (TBA-thrombin) = -35.6 kJ/mol, where $\Delta G_{binding}$ (TBA-antidote) = -67 kJ/mol[17, 21], so TBA's affinity for antidote is stronger than for thrombin. Blood clotting time was

restored to its original value at 1:1 TBA:antidote, indicating excess antidote was not needed to reverse TBA's function[22, 23].

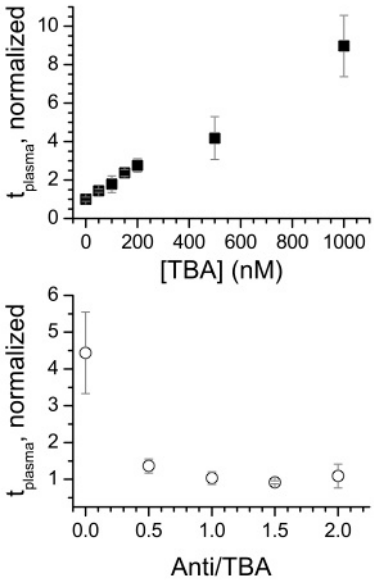

Figure 6-2. Calibration of TBA (top) and antidote:TBA, with [TBA]=500nM(bottom)

6.3. Preparation and characterization of NR-coronas

Cetyltrimethylammonium bromide (CTAB)-coated gold particles that absorbed at two distinct wavelengths were synthesized (see Chapter 2: Materials and Methods)[24-26]. Rod-shaped nanorods (NRs) with an aspect ratio (AR) = 3.7 and D_H = 45 nm had a longitudinal surface plasmon resonance (SPR) at 763 nm (Fig. 6-3, 6-5). Bone-shaped "nanobones" (NBs) with AR = 4.8 and D_H = 55 nm had a SPR at 1065 nm (Fig. 6-3, 6-5). Because NRs and NBs exhibited distinct absorption features, selective excitation by fs-pulsed lasers was possible. 800 nm irradiation of a NR-NB mixture resulted in melting of the NRs only, seen by a decrease of the SPR at 800 nm (Chapter 4, Fig. 4-8). Melting induces the NRs to change shape to spheres, which shifts and decreases their SPR[27]. The SPR at 1100 nm did not change, indicating that NBs were not melted because 800 nm coincides with a minimum in their absorption (Fig. 6-3, bottom, blue line). Likewise, NRs do not absorb at 1100 nm (Fig. 6-3, top, red line), so 1100 nm irradiation resulted in a decrease of the NB SPR but did not affect the NR SPR, indicating selective melting of the NBs (Chapter 4, Fig. 4-9)[5]. Melting of the NRs and NBs separately was confirmed (Chapter 4, Fig. 4-4 and 4-5 respectively).

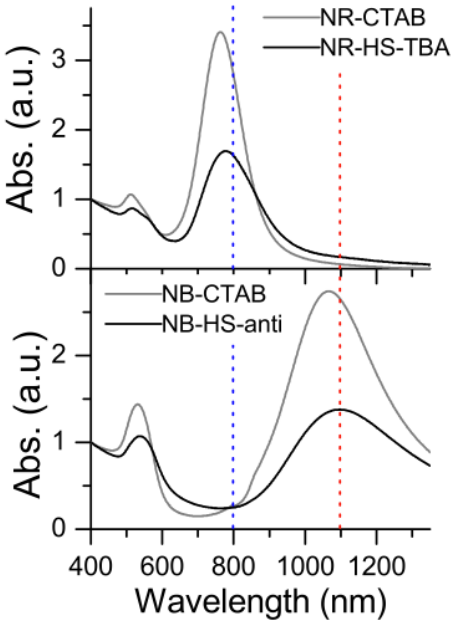

Figure 6-3. Absorbance spectra of NR, NB, NR-HS-TBA and NB-HS-anti

While DNA conjugation to gold NRs can be achieved by thiol-Au bonding[28], we used protein coronas because they exhibit high payload capacity while still enabling triggered release *via* laser excitation of the NR. Coronas of human serum (HS) were formed around the particles[4] and NR-coronas were loaded with TBA (NR-HS-TBA), NB-coronas with antidote (NB-HS-antidote). SPR of NR-HS-TBA was at 777nm, and SPR of NB-HS-antidote was at 1093nm. Loadings were quantified by heating the sample for 30 min and 90 °C and measuring the fluorescence spectroscopy of the supernatant, yielding 674TBA/NR and 1307Anti/NB (Fig. 6-4).

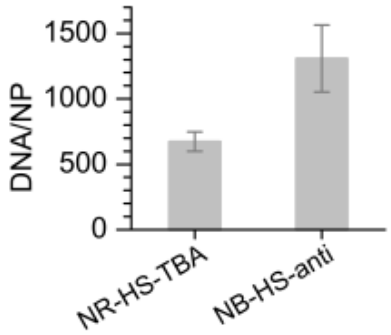

Figure 6-4. Loading of NR-HS-TBA and NB-HS-anti

The NR-HS-TBA had D_H = 662 nm, and NB-HS-antidote D_H = 938 nm (Fig. 6-5), as compared to initial CTAB-NR, with a D_H = 45 nm and CTAB-NBs, with a D_H = 55 nm, indicating that a corona contains multiple particles. Zeta potentials for NR-HS-TBA (-9.8mV) and NB-HS-anti (-10.1mV) were negative because HS is predominantly composed of negatively charged species (Fig. 6-5)[29]. Likewise, the zeta potentials of NR-CTAB (42.2mV) and NB-CTAB (50.2mV) are positive because CTAB is a positive surfactant.

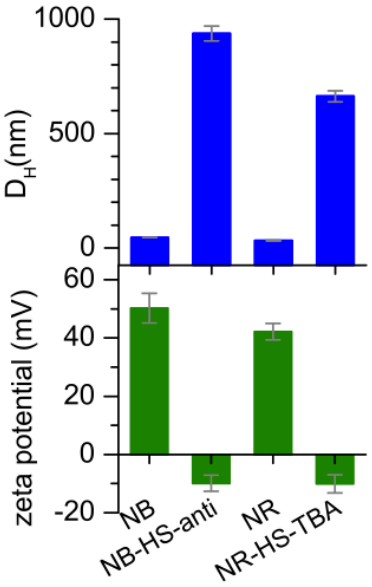

Figure 6-5. DLS and Zeta potential of NB-CTAB, NB-HS-anti, NRs-CTAB and NR-HS-anti

6.4. Single laser irradiations for the release of TBA and antidote

Laser irradiation of NR-HS-DNA could trigger DNA release. First, NB-HS-TBA (Fig. 6-6, black) were irradiated at 1100 nm and their SPR decreased, confirming NB melting (Fig. 6-6, red). Released antidote quantified by fluorescence was [anti] = 129 nM, or 430 anti/NB-HS-antidote (Fig. 6-6, inset).

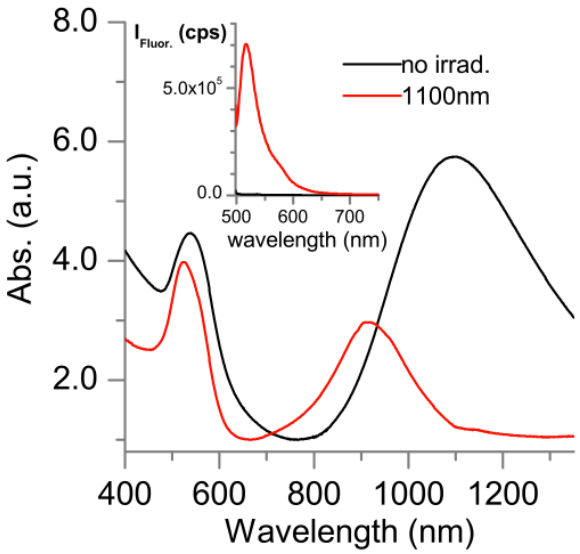

Figure 6-6. 1100nm irradiation of NB-HS-anti. Melting and release (inset)

Similarly, NR-HS-TBA (Fig. 6-7, black) were irradiated at 800 nm and their SPR decreased (Fig. 6-7, red), confirming melting, and released [TBA] = 663 nM or 228 TBA released/NR-HS-TBA (Fig. 6-7, inset).

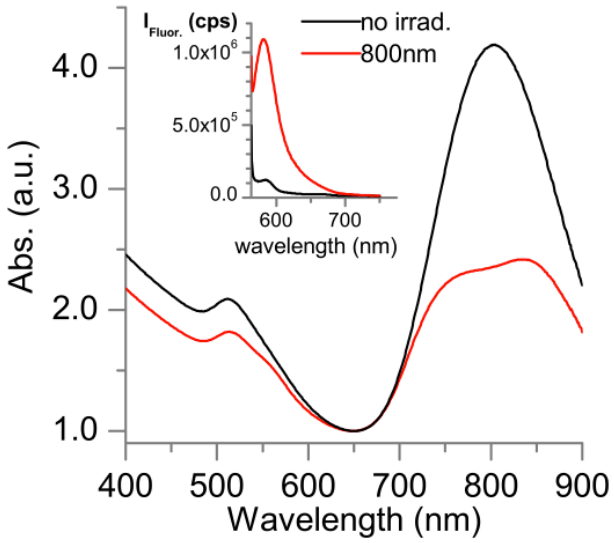

Figure 6-7. 800nm irradiation of NR-HS-TBA. Melting and release (inset)

We introduced released TBA in blood, in a aPTT clotting test, with 0nM thrombin added, and t_{plasma} increased to 1.61 (Fig. 6-8, red), comparable to the effect of free [TBA] = 609 nM (Fig. 3-8, red dot for released TBA, and red stars for TBA calibration). As compared to the supernatant from the NR-HS-TBA that was not exposed to the laser irradiation (t_{plasma}=1.0). Thus, TBA was ~94% functional in coagulation, which could be due to slight damage from the laser or steric hindrance by other released corona species. These experiments show that laser irradiation can release TBA from coronas on NRs, and released TBA is largely functional and can impact coagulation.

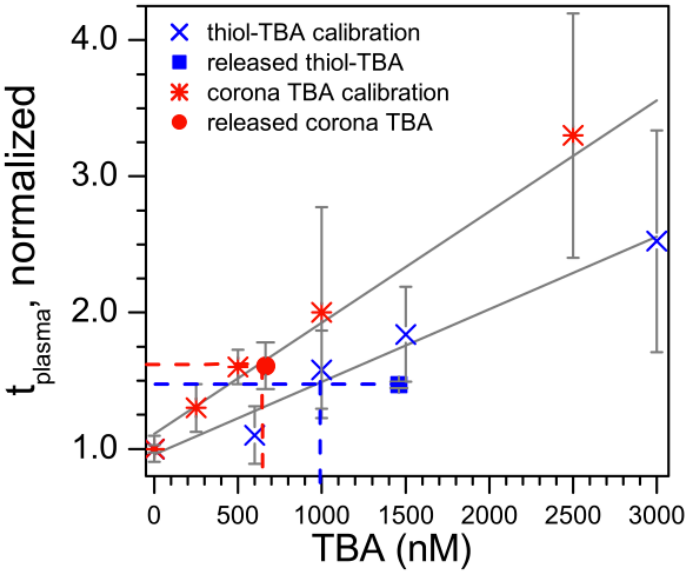

Figure 6-8. Comparison of HS-TBA-Bock release, thiolated TBA-NRs and calibrations

Using coronas for DNA loading has several advantages over covalent attachment. Compared to NRs conjugated to thiolated TBA (thiol-TBA), coronas had higher loadings and resulted in greater released DNA/NR. Analogous experiments performed with covalently attached thiol-TBA (Chapter 4) released 1.46 μM TBA from 11.2 nM NRs (Fig. 6-7, released thiolated TBA is shown by a blue square, and thiolated TBA calibration is shown by blue x), approximately half of what could be released from NR-HS-TBA (130 released TBA/NR-thiol-TBA vs. 223 released TBA/NR-HS-TBA). Furthermore, this NR concentration is optically dense, limiting absorption and necessitating long irradiation times (~30 min). Also, the functionality of released thiol-TBA was deteriorated.

Released thiol-TBA resulted in t_{plasma} = 1.47 (Fig. 6-8, blue), comparable to the effect of free [thiol-TBA] = 959 nM (Fig. 6.7, blue square and dashed line), exhibiting only 64% functionality. This is significantly lower compared to TBA from the corona, and could be attributed increased laser damage[30] due to it being directly attached to the NR combined with the long irradiation times. Thus, using coronas for loading can improve both yield and functionality of DNA, while also reducing irradiation time.

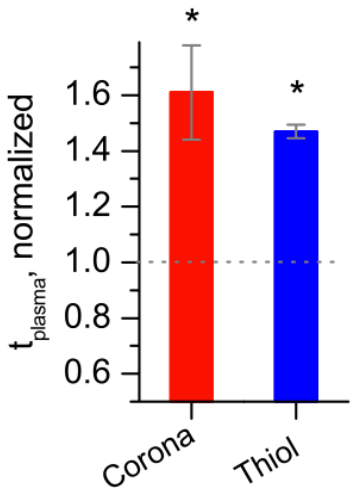

Figure 6-9. Comparison of HS-TBA-Bock release and thiolated TBA-NRs

6.5. Selective release of TBA and antidote for the control of blood clotting

We selectively released TBA and antidote to inhibit and then restore blood clotting. First, a NR-HS-TBA + NB-HS-antidote mixture (Fig. 6-10, black) was exposed to 800 nm irradiation. The 800 nm SPR decreased but the 1100 nm SPR was unaffected, confirming selective melting of the NRs under the 800nm irradiation(Fig. 6-10, red).

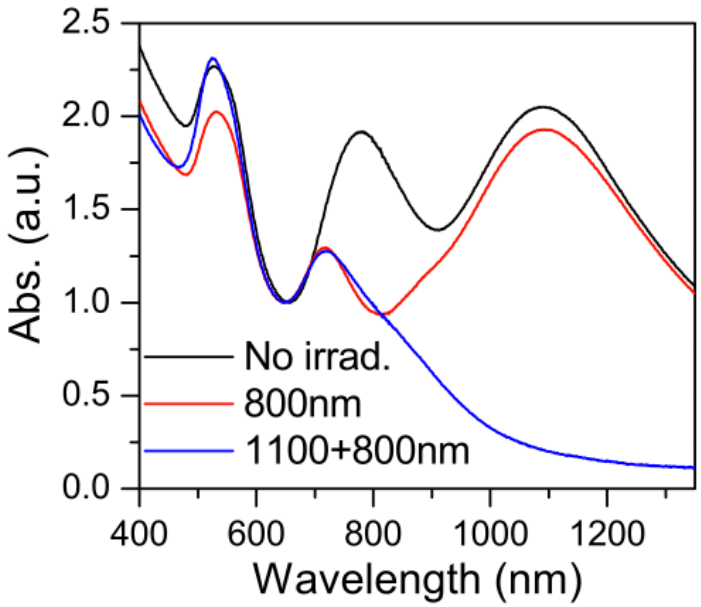

Figure 6-10. Comparison of HS-TBA-Bock release and thiolated TBA-NRs

TMR fluorescence in the supernatant due to released TBA increased while FAM fluorescence due to the antidote did not increase as much, illustrating that the NRs

preferentially released payload (Fig. 6-11, red). Quantifying release showed that 800 nm irradiation released 107 nM TBA (252 released TBA/NR), but only 1.3 nM antidote.

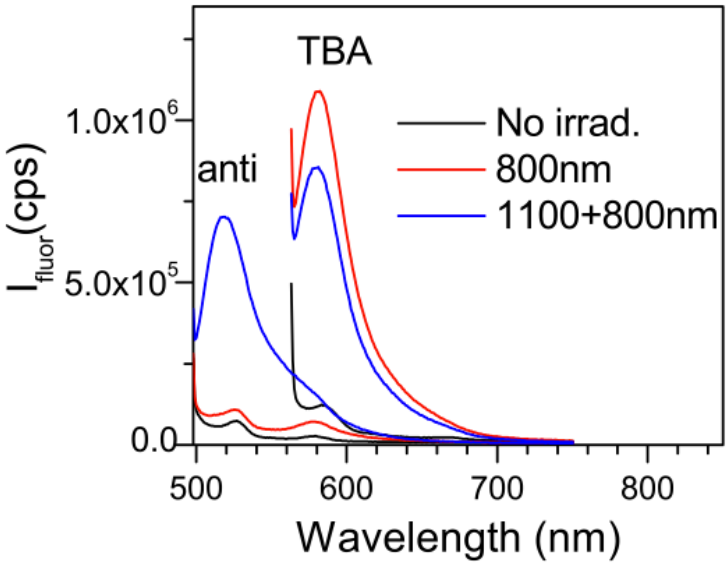

Figure 6-11. Comparison of HS-TBA-Bock release and thiolated TBA-NRs

Released species introduced to blood resulted in an increase in t_{plasma} to 1.73 (Fig. 6-12, 800nm), indicating that released TBA inhibited thrombin and thus blood coagulation. Next, the NR-HS-TBA + NR-HS-antidote mixture was irradiated at 1100 nm. The 1100 nm SPR decreased, confirming NB melting (Fig. 6-10, blue). FAM fluorescence increased, indicating that 152 nM antidote was released (692 released antidote/NB) (Fig.6-11, blue), while 63 nM TBA was released. The effect on coagulation was t_{plasma} =

0.88, demonstrating that released antidote could reverse the effect of TBA and restore coagulation to its original t_{plasma} (Fig. 6-12, 1100&800nm).

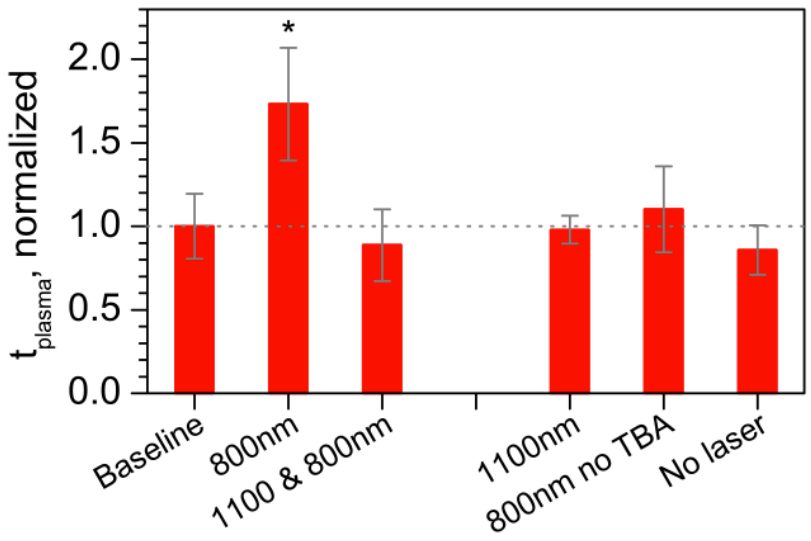

Figure 6-12. Comparison of HS-TBA-Bock release and thiolated TBA-NRs

To test selectivity of the switch, 1100 nm irradiation alone on NR-HS-TBA + NB-HS-anti (Fig. 6-12, 1100nm) did not significantly change t_{plasma} (0.98, Fig. 6-11), showing that antidote release alone does not affect coagulation. The mixture of NR-HS-TBA and NS-HS-anti (Fig. 6-13, blue) was irradiated at 1100nm, and melting of the NBs as a decrease on their SPR was observed (Fig. 6-13, a, red), while NR-HS-TBA did not melt. 216nM antidote and 4nM TBA were released (Fig. 6-13, b, red).

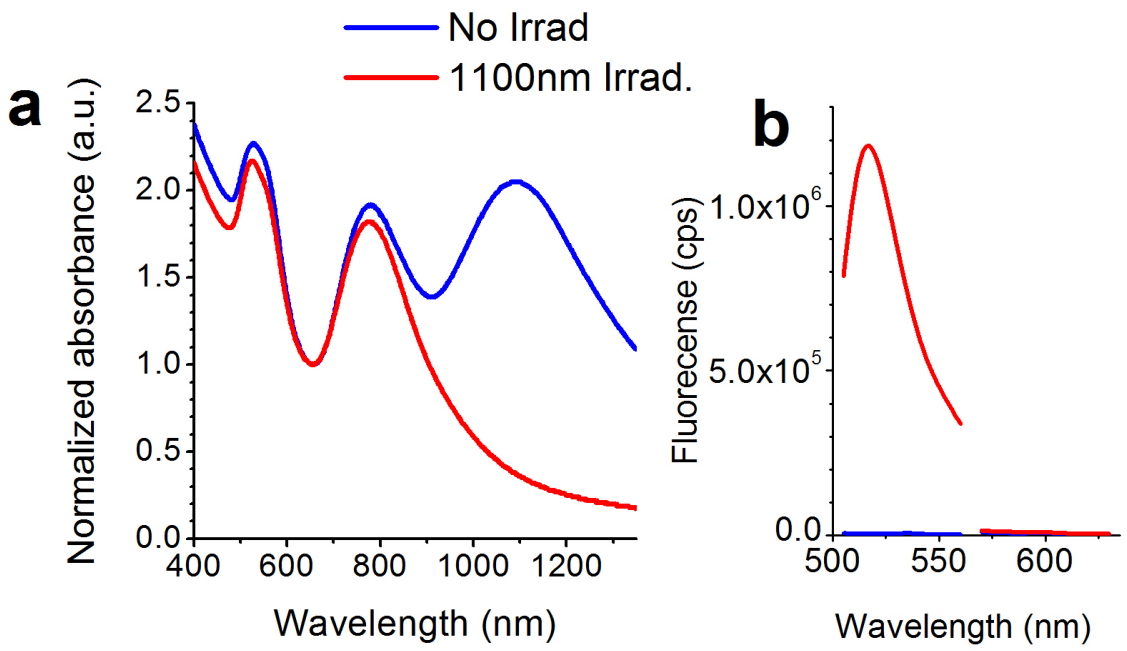

Figure 6-13. 1100nm irradiation of the NR-HS-TBA and NB-HS-antidote. Left: Absorbance. Right: fluorescence of the released species

To test whether HS release affects coagulation, NR-HS were prepared without TBA and mixed with NB-HS-anti. 800 nm irradiation resulted in no significant change in t_{plasma} (1.1), (Fig. 6-12, 800nm no TBA) confirming that the presence of TBA was necessary to affect coagulation. Finally, we verified that the presence of NR-HS-TBA + NB-HS-anti mixture with blood did not affect t_{plasma} (0.86) (Fig. 6-12, No laser).

Because protein coronas and ssDNA (TBA and antidote) are not covalently bound to the NPs, there is the possibility of disruption of the corona around the NRs, by exchange with blood proteins and other small biomolecules. This does indeed happen, and can be

measured. We introduced NR-HS-TBA directly into blood, and measured t_{plasma} (Fig. 6.14, NR). This value can be compared to the increase in t_{plasma} from released TBA from coronas (Fig. 6.14, 800nm), and we can observe that even though there is an increase in t_{plasma} due to the leakage of TBA from the coronas, the increase on t_{plasma} when NRs are irradiated at 800nm is still much higher. The increase on t_{plasma} due to leakage from the coronas is equivalent to 38nM TBA -or 89 TBA/NR-, which represent a 14% release from coronas, as compared to the 42% released achieved by laser irradiation. We also introduced NR-HS-TBA and NB-HS-antidote into blood and measured the effect of TBA+antidote leaked from coronas into blood (Fig. 6.14, NB+NR), and the effect of TBA+antidote released by laser irradiations from NR-coronas (Fig. 6.14, 800&1100). We observe that when NRs and NBs leak both TBA and antidote into blood, there is no change in t_{plasma} , as the antidote and TBA hybridize.

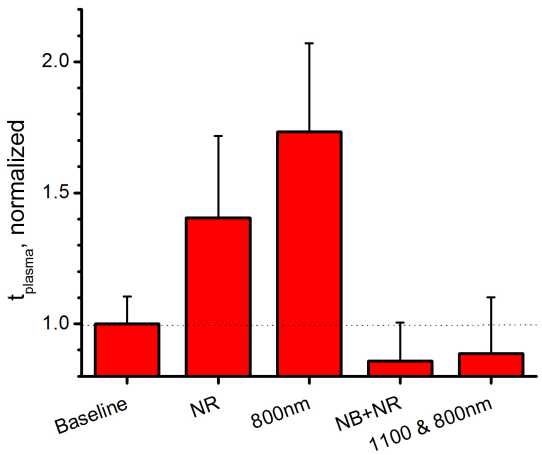

Figure 6-14. Measurement of the effect of particles in blood.

6.4. Conclusions

This work demonstrates that external laser excitation can selectively release a thrombin inhibitor and its antidote, allowing the NR/NB pair to act as an on/off switch for blood clotting. Blood clotting time is increased after 800nm laser irradiation of the mixture due to the release of TBA only. After 1100nm irradiation, blood clotting time returns to its original value, as antidote is released and base-pair with the TBA, leaving thrombin free to form blood clots.

Protein coronas represent an advantage in the release of ssDNA, as they enable enhanced loading on the particles, doubling the ssDNA/NP released. Furthermore, ssDNA released from protein coronas is highly functional compared to the TBA released from covalent attachment.

On the other hand, NR-coronas have shown to leak small amounts of TBA in blood. However, TBA leaked from the NR-coronas due to protein exchange in blood represents a 14% TBA leaked, as compared to the 40% TBA that can be released from NR-coronas though laser irradiation. More research can be done in order to further decrease the concentration of TBA that leaks from the NR-coronas in blood.

6.5. Bibliography

[1] Lynch I, Salvati A, Dawson KA. Protein-nanoparticle interactions: What does the cell see? Nature Nanotechnology 2009;4:546.

[2] Lundqvist M, Stigler J, Elia G, Lynch I, Cedervall T, Dawson KA. Nanoparticle size and surface properties determine the protein corona with possible implications for biological impacts. Proceedings of the National Academy of Sciences 2008;105:14265.

[3] Monopoli MP, Aberg C, Salvati A, Dawson KA. Biomolecular coronas provide the biological identity of nanosized materials. Nat Nano 2012;7:779.

[4] Kah JCY, Chen J, Zubieta A, Hamad-Schifferli K. Exploiting the Protein Corona around Gold Nanorods for Loading and Triggered Release. ACS Nano 2012;6.

[5] Wijaya A, Schaffer SB, Pallares IG, Hamad-Schifferli K. Selective Release of Multiple DNA Oligonucleotides from Gold Nanorods. ACS Nano 2008;3:80.

[6] Huschka R, Zuloaga J, Knight MW, Brown LV, Nordlander P, Halas NJ. Light-Induced Release of DNA from Gold Nanoparticles: Nanoshells and Nanorods. Journal of the American Chemical Society 2011;133:12247.

[7] Lee SE, Sasaki DY, Park Y, Xu R, Brennan JS, Bissell MJ, Lee LP. Photonic Gene Circuits by Optically Addressable siRNA-Au Nanoantennas. ACS Nano 2012;6:7770.

[8] Barhoumi A, Huschka R, Bardhan R, Knight MW, Halas NJ. Light-induced release of DNA from plasmon-resonant nanoparticles: Towards light-controlled gene therapy. Chemical Physics Letters 2009;482:171.

[9] Yamashita S, Fukushima H, Akiyama Y, Niidome Y, Mori T, Katayama Y, Niidome T. Controlled-release system of single-stranded DNA triggered by the photothermal effect of gold nanorods and its in vivo application. Bioorganic & Medicinal Chemistry 2011;19:2130.

[10] Lefkovits J, Topol EJ. Direct thrombin inhibitors in cardiovascular medicine. Circulation 1994;90:1522.

[11] Joachimi A, Mayer G, Hartig JS. A new anticoagulant-antidote pair: Control of thrombin activity by aptamers and porphyrins. Journal of the American Chemical Society 2007;129:3036.

[12] Walkey CD, Olsen JB, Guo H, Emili A, Chan WCW. Nanoparticle Size and Surface Chemistry Determine Serum Protein Adsorption and Macrophage Uptake. Journal of the American Chemical Society 2012;134:2139.

[13] Bock LC, Griffin LC, Latham JA, Vermaas EH, Toole JJ. Selection of single-stranded DNA molecules that bind and inhibit human thrombin. 1992;355:564.

[14] Tasset DM, Kubik MF, Steiner W. Oligonucleotide inhibitors of human thrombin that bind distinct epitopes. 1997;272:688.

[15] Padmanabhan K, Padmanabhan KP, Ferrara JD, Sadler JE, Tulinsky A. The structure of alpha-thrombin inhibited by a 15-mer single-stranded-DNA aptamer. Journal of Biological Chemistry 1993;268:17651.

[16] Kim YM, Phillips JA, Liu HP, Kang HZ, Tan WH. Using photons to manipulate enzyme inhibition by an azobenzene-modified nucleic acid probe. Proceedings of the National Academy of Sciences of the United States of America 2009;106:6489.

[17] Pagano B, Martino L, Randazzo A, Giancola C. Stability and binding properties of a modified thrombin binding aptamer. Biophysical Journal 2008;94:562.

[18] de Puig H, Federici S, Baxamusa SH, Bergese P, Hamad-Schifferli K. Quantifying the Nanomachinery of the Nanoparticle-Biomolecule Interface. Small 2011;7.

[19] Macaya RF, Schultze P, Smith FW, Roe JA, Feigon J. Thrombin-binding DNA aptamer forms a unimolecular quadruplex structure in solution. Proceedings of the National Academy of Sciences of the United States of America 1993;90:3745.

[20] Müller J, Freitag D, Mayer G, Pötzsch B. Anticoagulant characteristics of HD1-22, a bivalent aptamer that specifically inhibits thrombin and prothrombinase. Journal of Thrombosis and Haemostasis 2008;6:2105.

[21] Markham NR, Zuker M. DINAMelt web server for nucleic acid melting prediction. Nucleic Acids Research 2005;33:W577.

[22] Rusconi CP, Roberts JD, Pitoc GA, Nimjee SM, White RR, Quick G, Scardino E, Fay WP, Sullenger BA. Antidote-mediated control of an anticoagulant aptamer in vivo. Nat Biotech 2004;22:1423.

[23] Schwienhorst A. Direct thrombin inhibitors--a survey of recent developments. Cellular and Molecular Life Sciences CMLS 2006;63:2773.

[24] Sau TK, Murphy CJ. Seeded High Yield Synthesis of Short Au Nanorods in Aqueous Solution. Langmuir 2004;20:6414.

[25] Gou L, Murphy CJ. Fine-Tuning the Shape of Gold Nanorods. Chemistry of Materials 2005:3668

[26] Jana NR. Gram-scale synthesis of soluble, near-monodisperse gold nanorods and other anisotropic nanoparticles. Small 2005;1:875.

[27] Link S, Burda C, Nikoobakht B, El-Sayed MA. Laser-induced shape changes of colloidal gold nanorods using femtosecond and nanosecond laser pulses. Journal of Physical Chemistry B 2000;104:6152.

[28] Wijaya A, Hamad-Schifferli K. Ligand Customization and DNA Functionalization of Gold Nanorods via Round-Trip Phase Transfer Ligand Exchange. Langmuir 2008;24:9966.

[29] Casals E, Pfaller T, Duschl A, Oostingh GJ, Puntes V. Time Evolution of the Nanoparticle Protein Corona. ACS Nano 2010;4:3623.

[30] Jain PK, Qian W, El-Sayed MA. Ultrafast Cooling of Photoexcited Electrons in Gold Nanoparticle−Thiolated DNA Conjugates Involves the Dissociation of the Gold−Thiol Bond. Journal of the American Chemical Society 2006;128:2426.

7. Conclusions and future directions

7.1. Summary of the work

We have been able to utilize gold nanoparticles in order to create a two-way optical switch of blood clotting, in a way that enables a localized, selective, specific and externally activated control of the clot formation process. Gold nanoparticles with different aspect ratios can be selectively excited with lasers in order to release payloads on their surface. We use this idea to selectively release thrombin binding aptamers (TBA) and their antidotes. Released TBA can bind to thrombin and increase blood clotting time; and the antidote can bind to TBA in order to reverse its effects and result in normal clotting times. Moreover, protein coronas enable enhanced release and functionality of the payloads compared to covalent attachment strategies. Covalent attachment techniques are also introduced and used for quantification of the interactions between thrombin and TBA, when TBA is bound to the surface of NRs.

This approach can be extended to any application that requires the creation of an on/off switch or the release of multiple biomolecules in a localized and externally controlled manner, such as in cancer applications, where great improvements could be made if it were possible to release different drugs in a time and space controlled manner, or in

controlled gene expression. Below is a summarized list of the main conclusions of the thesis, while more extended conclusions can be found in each chapter of the thesis.

In Chapter 3 of this thesis, we have discussed the interactions of *biological nanomachines at the NP interface*. We have both studied both the hybridization of DNA on surfaces, and the assembly of NRs induced by the presence of a binding biomolecule –in our case thrombin. First, we have studied the thermodynamics of the assembly and disassembly of NRs, and introduced a model to explain the thermodynamics of NR assembly in the presence of thrombin. This model is completely general and enables for the calculation of the surface work that is produced on the NRs surface during the assembly process. We extend this work in order to compare between NRs with different surface chemistries (See Chapter 3.2.4, for more conclusions on this work). Also, the kinetics of the binding process has been introduced. We have used a simplified model to explain the kinetics of TBA decorated-NRs assembly due to the presence of thrombin (See Chapter 3.3.4, for more conclusions on this work). DNA hybridization at the interface has been introduced. We have been able to describe it by using Langmuir's approach of surface absorption. We calculated the binding efficiency of complementary DNA on the surface of NRs with different surface chemistries, and, although more experimentation needs to be done to obtain more concluding results, we have observed a clear difference in the binding

efficiency depending on the surface properties of the particles (See Chapter 3.4.3, for more conclusions on this work). Also, a model to explain the NRs disassembly after the addition of TBA's complementary sequence has been introduced (Chapter 3.5.3, for more conclusions on this work). All of these results help to quantitatively describe the physical properties of the interface of biomolecules with nanomaterials, which can aid applications in which nanomaterials are used for biological applications. However, many challenges remain for the interface, and more experimentation needs to be done in order to be able to give details on the thermodynamics of the NRs disassembly process (see Chapter 3.6 for more conclusions on this work).

In Chapter 4, we were able to melt NR-NB mixtures selectively and to release covalently bound ssDNA from NRs by using a fs laser excitation. However, the concentration of NPs that were necessary to be used in the control of blood clotting was prohibitively high (12nM), therefore we decided to test new loading strategies on the NRs that could enable for enhanced loading of ssDNA on the NPs, and therefore permit a lower concentration of NPs (see Chapter 4.5 for further conclusions on this work).

In Chapter 5, we used *coronas of absorbed proteins as "sponges" for high payload capacity*. Basically, human serum could hold large amounts of ssDNA (~6x monolayer ssDNA coverage compared to loading by covalent chemistry0. We found the parameters

that played a most important role in the formation of protein coronas, and searched the best conditions for an external release application, in which leakage from the protein coronas could be minimized until there is an external signal such as laser irradiation. We show that 5mM PB, 5mM CTAB and 5% HS enable for an enhanced loading on the NPs, while keeping the leakage minimized. Moreover, we observed that by tuning the formation process of protein coronas on NPs, it is possible to modify the passive release profile, which would enable us to engineer coronas with controlled passive release profiles, in order to decide when maximum release would occur and the speed of the release from the coronas. Because the formation of protein coronas on nanoparticles is inevitable, using them for enhanced loading and controlled release opens up new possibilities in nanobiotechnology and nanomedicine, where the current practise is to focus on preventing binding of proteins on the nanoparticles (see Chapter 5.6 for more conclusions on this work).

Finally, in Chapter 6, we show that *selective and externally controlled release from NR-coronas is possible and it can be used to control blood clotting*. We demonstrate that both NRs and NBs can be selectively excited in order to release TBA and antidote respectively. Moreover, we show that ssDNA released from NR coronas is higher (double) than the amount released from covalently bound TBA on NRs, due to the

enhanced loading that coronas permit. Moreover, we could observe that TBA released from protein coronas is highly functional (94%) as compared to the thiolated TBA released from covalent binding that exhibited a 64% functionality (see Chapter 6.4 for further conclusions on this work).

These results show that nanomaterials can be used for triggered release. While the interface of nanomaterials with biological systems presents many challenges, physical characterization of the interface properties can be used to yield a deeper insight and ultimately better control. In addition, protein coronas present a unique challenge for nanomaterials, but can be exploited for enhanced release capabilities of the NRs, and also for biocompatibility, as serum proteins are already present in blood.

7.1.1. Limitations and further studies

Although the results of this work are very promising, and *in vitro* tests show that gold nanorods can be used to control blood clotting, there are a number of limitations that need to be taken into account, especially if we aim to use the selective release of TBAs and antidotes *in vivo*.

The first of them are the interactions of coronas of NPs with other proteins in blood. Due to the fact that protein coronas and ssDNA (TBA and antidote) are not covalently

bound to the NPs, there is the chance that the corona around the NRs will exchange with blood proteins. This does indeed happen, and can be measured. However, the increase in t_{plasma} due to leakage from protein coronas into blood is much lower than the increase in t_{plasma} after laser irradiation. Indicating that although there is exchange of proteins from the corona, most of the TBA is retained.

Other limitations include the size of the NP-coronas. By DLS, we have been able to measure the particle's hydrodynamic diameter to be ~600nm. Although this is still small enough for transport in the bloodstream without blocking the capillaries (NR-coronas are still much smaller than red blood cells), some flow simulations should be done in order to ensure that NR-coronas do not incur a risk of obstructing capillaries, especially in the brain, kidneys and lungs.

Also, shear stress measurements by rheology and computer simulations[1] should be performed on NR-coronas to measure if disruption of the coronas is possible when they are under shear stresses due to blood flow. Some preliminary experiments have been performed by pipetting NR-coronas through capillaries, and no release of TBA was observed. However, those experiments were very preliminary and done by hand, so it was not possible to measure the shear stresses acting on the coronas during pipetting.

Therefore, further experiments need to be performed in order to obtain quantitative information.

New limitations may arise when testing the system *in vivo*. TBA used in this work is highly specific and has a poor effect when targeting non-human thrombin. However, in order to use TBAs in a clinical environment it is necessary to perform *in vivo* tests with animals on the first place. This limitation has been overcome by sequencing new aptamers that can target thrombin from different animal species by using "toogle" SELEX[2]. Moreover, these new aptamers and their antidotes have already been tested *in vivo* and it has been shown that blood clotting can be switched on and off by adding the modified TBA and modified antidotes[3]. Nevertheless, localized and external control of the blood clotting has not yet been achieved, to the best of our knowledge.

Other limitations are related to the concentration of NRs that can be introduced in blood, and the concentration of NRs that can be melted by laser irradiation. These concentrations will depend on the toxicity of the particles, and the concentration of NRs that can be introduced in the body without causing side effects would need to be known, as well as the release yields of TBA and antidotes *in vivo*.

The concentration of payloads released *in vivo* from the coronas may decrease due to absorption and scattering of the laser light by the tissue. As we have previously

introduced, laser light with wavelengths between 600-1300nm should be mostly tissue and blood transparent[4-8]. However, some absorption and scattering effects do exist, which leads to a poor penetration of laser light in tissue, reaching only a few mm in penetration[7, 9-11]. This issue could be potentially overcome by using optical fiber which can be produced with diameters than $<$ 1mm in order to introduce the laser light into the desired part of the body.

7.1.2. Advantages

Although limitations do exist, we believe that the advantages of creating a localized control of blood clotting would be noteworthy, as they would enable much safer surgery on patients.

When performing surgery on patients that are treated with heparin and warfarin, the current practice is to wait until the effects of the drug have stopped in order to avoid a high risk of bleeding. However, in situations where emergency surgery is necessary and waiting for heparin/warfarin clearance cannot be realistically achieved, patients are currently given frozen plasma (or prothrombin in rare occasions) to stop the effects of the anticoagulants. However, there is little control in blood clotting when giving frozen plasma to patients, and consequently it is a dangerous practice. Therefore, the introduction of an anticoagulant/antidote pair would be very beneficial.

Moreover, the reason most patients are given anticoagulants is because they tend to form blood clots when blood is flowing normally and there is a high risk of formation of blood clots when the effect of the anticoagulants in the system is stopped -through the use of the antidotes-, because the formed blood clots can later travel through the body and potentially cause strokes. Therefore, the introduction of a localized and externally controlled switch for blood clotting would be beneficial, as it would enable to stop the activity of the anticoagulant only in one specific area, while still preventing the formation of blood clots elsewhere.

7.2. Future prospects and applications

While the issue of the interface of nanomaterials with biology is still an open challenge, where we have much to learn, this work can enable new applications and potentially open up many research possibilities.

7.2.1. Control of blood clotting using gold nanorods in vivo

The first opportunity that this work introduces is testing the optical switch for blood clotting *in vivo.* Modified aptamers that can target thrombin from mice, pigs and humans can be used[3], and their release from NR-coronas could be tested. These experiments can be also performed *in vivo*, to design an optical switch for blood clotting with potential clinical applications.

In order to release TBAs and antidotes in the site of injury, two methods can be envisioned. (1) Directing the laser light only in the site of interest, and therefore only the NRs in that area would release TBAs and antidotes, (2) biochemically modifying the proteins used for the formation of the NR-coronas, in order to enable tumor targeting and (3) including the NR-coronas in hydrogels[12, 13], that could be introduced in the site of interest, and directing the laser light in that area as well. This last method would

enable the externally controlled selective release of the biomolecules, while minimizing the concentration of NR-coronas introduced in the body.

7.2.2. Triggered release for combinational therapy

Other conditions that require the use of combinational therapy, where more than one drug needs to be used in a certain order or simultaneously, would as well benefit from the use of optical switches. A prime example of this is cancer.

Anticancer drugs are generally cytotoxic for both cancerous and normal cells. Moreover, drug resistance in cancer appears due to (1) low vascularization of tumors that can reduce drug access and protect cancerous cells from cytotoxicity of the drug; and also, (2) through biochemical alterations of cancerous cells that can affect the transport of drugs into the cells[14, 15].

By using gold nanoparticles, it would be possible to selectively release multiple anticancer drugs in the tumor site; selective release would enable for the possibility of externally controlling the release of different drugs that could (1) on the first place silence the genes that prevent the transport of cancer drug in the tumor[16] and (2) later release anticancer drugs, such as doxorubicin[17].

By using selected aptamers that can target cancerous cells, gold nanoparticles could be directed to the tumor[18-23]. Tumor cell targeting and drug delivery by light irradiation has previously been demonstrated[24], but to the best of our knowledge, selective release from multiple NR-coronas to achieve combinational therapy in cancer has yet to be tested. Another advantage of using NR-coronas for the release of drugs in cancers is that they are good contrast agents for computed tomography (CT)[22], and therefore it would be possible to use them as well to monitor of the tumors during the therapy.

7.2.3. Switchable enhancement of *in vitro* translation with light

Previous work from the Hamad-Schifferli group has shown that using gold nanoparticles for nonspecific absorption of proteins can enhance *in vitro* translation[25]. Following this approach, and knowing that near-infrared (NIR) CW laser irradiation results in localized heating of the NPs, without melting them or releasing the thiol-gold bonds[26], it is possible to envision a situation in which *in vitro* translation of proteins could be externally controlled by localized heating of the NRs.

Translation of the mRNA that encodes a protein involves the ribosomes, mRNA and many other species, that can nonspecifically adsorb on NPs and result in enhanced translation, when the NPs are covalently linked with ssDNA that binds specifically to the mRNA of interest[25]. Therefore, NP-ssDNA conjugates could be introduced in a

cell-free translation system such as retic lysate or wheat germ mix and result in enhanced translation. Through CW laser irradiation, it is possible to selectively heat the NPs, resulting in disruption of the nonspecific interactions, and therefore the translation of the protein. After stopping laser irradiation it would be possible to enhance protein translation again, because the CW laser irradiation does not break the covalent bonds between the DNA and the NPs.

7.2.4. Nanobiomachinery and protein-NR / DNA-NR origamis

Biomolecular nanomachines can be used for collective behaviour of NPs. In *Chapter 3*, we have shown that the addition of proteins (thrombin) and ssDNA (antidote) can be used in order to assemble and disrupt nanoparticle assemblies, due to the specific interaction of thrombin and TBA, where thrombin can bind to two different TBAs bound to different NRs. Also, the introduction of ssDNA complementary to TBA can disrupt the aggregates, as it can bind to TBA and therefore release thrombin. Similarly, it has also been shown that assemblies of NP-ssDNA can be prepared by using partially complementary ssDNA that can bind to two different ssDNA on the NPs[27, 28]. NP assemblies have the great advantage that they can be easily characterized, and the energies of binding and disrupting the aggregates can be measured by absorbance spectroscopy using the thermodynamic approach explained in *Chapter 3.2*.

Inspired in DNA origami[29] which have been used for drug delivery[30]; NR-DNA assemblies could be as well used for enhanced loading of payloads, such as intercalating species such as doxorubicin or DNA binding proteins, while maintaining its optical properties due to the gold nanoparticles. Furthermore, the nanoparticles enable selective and localized release by laser irradiation.

The NP-DNA assemblies could be prepared in order to have different sizes and shapes through direct assembly or in a layer-by-layer approach by surface modification of the ssDNA-decorated-NPs, or by tuning the concentration of linker ssDNA. It is known that anticancer drugs such as mitoxantrone, doxorubicin or elliptisine can intercalate within the dsDNA[31, 32], and therefore it would be possible to encapsulate them in the NP assemblies. Once these drugs are encapsulated in the NP-DNA carriers, they could be released by laser irradiation of the NPs at their SPR.

7.3. Bibliography

[1] Korin N, Kanapathipillai M, Matthews BD, Crescente M, Brill A, Mammoto T, Ghosh K, Jurek S, Bencherif SA, Bhatta D, Coskun AU, Feldman CL, Wagner DD, Ingber DE. Shear-Activated Nanotherapeutics for Drug Targeting to Obstructed Blood Vessels. Science 2012;337:738.

[2] White R, Rusconi C, Scardino E, Wolberg A, Lawson J, Hoffman M, Sullenger B. Generation of species cross-reactive aptamers using "toggle" SELEX. Molecular Therapy 2001;4:567.

[3] Rusconi CP, Roberts JD, Pitoc GA, Nimjee SM, White RR, Quick G, Scardino E, Fay WP, Sullenger BA. Antidote-mediated control of an anticoagulant aptamer in vivo. Nature Biotechnology 2004;22:1423.

[4] Janssen FJ. Study of absorption and scattering factors of light in whole-blood. Medical & Biological Engineering 1972;10:231.

[5] Hardy JD, Hammel HT, Murgatroyd D. Spectral transmittance and reflectance of excised human skin. Journal of Applied Physiology 1956;9:257.

[6] Kolarova H, Ditrichova D, Wagner J. Penetration of the laser light into the skin in vitro. Lasers in Surgery and Medicine 1999;24:231.

[7] Eichler J, Knof J, Lenz H. Measurements on depth of penetration of light (0.35-1.0mu-m) in tissue. Radiation and Environmental Biophysics 1977;14:239.

[8] Ying-Ying Huang MHaAC-HC. Low-level laser therapy: an emerging clinical paradigm. SPIE Newsroom, 2009.

[9] Zdrojkow.Rj, Longini RL. Optical transmission through whole blood illuminated with highly collimated light. Journal of the Optical Society of America 1969;59:898.

[10] Cabrera-Trujillo JM, Montejano-Carrizales JM, Rodriguez-Lopez JL, Zhang W, Velazquez-Salazar JJ, Jose-Yacaman M. Nucleation and Growth of Stellated Gold Clusters: Experimental Synthesis and Theoretical Study. Journal of Physical Chemistry C 2010;114:21051.

[11] Schmitt JM, Zhou GX, Walker EC, Wall RT. Multilayer model of photon diffusion in skin. Journal of the Optical Society of America a-Optics Image Science and Vision 1990;7:2141.

[12] Artzi N, Shazly T, Crespo C, Ramos AB, Chenault HK, Edelman ER. Characterization of Star Adhesive Sealants Based On PEG/Dextran Hydrogels. Macromolecular Bioscience 2009;9:754.

[13] Artzi N, Oliva N, Puron C, Shitreet S, Artzi S, Ramos AB, Groothuis A, Sahagian G, Edelman ER. In vivo and in vitro tracking of erosion in biodegradable materials using non-invasive fluorescence imaging. Nature Materials 2011;10:704.

[14] Brigger I, Dubernet C, Couvreur P. Nanoparticles in cancer therapy and diagnosis. Advanced Drug Delivery Reviews 2012;64:24.

[15] Gottesman MM. Mechanisms of cancer drug resistance. Annual Review of Medicine 2002;53:615.

[16] Huschka R, Barhoumi A, Liu Q, Roth JA, Ji L, Halas NJ. Gene Silencing by Gold Nanoshell-Mediated Delivery and Laser-Triggered Release of Antisense Oligonucleotide and siRNA. Acs Nano 2012;6:7681.

[17] Kah JCY, Chen J, Zubieta A, Hamad-Schifferli K. Exploiting the protein corona around gold nanorods for loading and triggered release. ACS Nano 2012:Just Accepted.

[18] Bagalkot V, Zhang L, Levy-Nissenbaum E, Jon S, Kantoff PW, Langer R, Farokhzad OC. Quantum dot - Aptamer conjugates for synchronous cancer imaging, therapy, and sensing of drug delivery based on Bi-fluorescence resonance energy transfer. Nano Letters 2007;7:3065.

[19] Chen XL, Huang YF, Tan WH. Using Aptamer-Nanoparticle Conjugates for Cancer Cells Detection. Journal of Biomedical Nanotechnology 2008;4:400.

[20] Herr JK, Smith JE, Medley CD, Shangguan DH, Tan WH. Aptamer-conjugated nanoparticles for selective collection and detection of cancer cells. Analytical Chemistry 2006;78:2918.

[21] Huang YF, Chang HT, Tan WH. Cancer cell targeting using multiple aptamers conjugated on nanorods. Analytical Chemistry 2008;80:567.

[22] Kim D, Jeong YY, Jon S. A Drug-Loaded Aptamer-Gold Nanoparticle Bioconjugate for Combined CT Imaging and Therapy of Prostate Cancer. Acs Nano 2010;4:3689.

[23] Medley CD, Bamrungsap S, Tan W, Smith JE. Aptamer-Conjugated Nanoparticles for Cancer Cell Detection. Analytical Chemistry 2011;83:727.

[24] Huang YF, Sefah K, Bamrungsap S, Chang HT, Tan W. Selective Photothermal Therapy for Mixed Cancer Cells Using Aptamer-Conjugated Nanorods. Langmuir 2008;24:11860.

[25] Park S, Hamad-Schifferli K. Enhancement of In Vitro Translation by Gold Nanoparticle-DNA Conjugates. Acs Nano 2010;4:2555.

[26] Chen CC, Lin YP, Wang CW, Tzeng HC, Wu CH, Chen YC, Chen CP, Chen LC, Wu YC. DNA-gold nanorod conjugates for remote control of localized gene expression by near infrared irradiation. Journal of the American Chemical Society 2006;128:3709.

[27] Jin RC, Wu GS, Li Z, Mirkin CA, Schatz GC. What controls the melting properties of DNA-linked gold nanoparticle assemblies? Journal of the American Chemical Society 2003;125:1643.

[28] Geerts N, Eiser E. DNA-functionalized colloids: Physical properties and applications. Soft Matter 2010;6:4647.

[29] Douglas SM, Dietz H, Liedl T, Hoegberg B, Graf F, Shih WM. Self-assembly of DNA into nanoscale three-dimensional shapes. Nature 2009;459:414.

[30] Jiang Q, Song C, Nangreave J, Liu X, Lin L, Qiu D, Wang Z-G, Zou G, Liang X, Yan H, Ding B. DNA Origami as a Carrier for Circumvention of Drug Resistance. Journal of the American Chemical Society 2012;134:13396.

[31] Cummings J, Bartoszek A, Smyth JF. Determination of covalent binding to intact DNA, RNA, and oligonucleotides by intercalating anticancer drugs using high-performance liquid-chromatography – studies with doxorubicin and NADPH cytochrome-P-450 reductase. Analytical Biochemistry 1991;194:146.

[32] Traganos F, Kapuscinski J, Darzynkiewicz Z. Caffeine modulates the effects of DNA-intercalating drugs invitro – a flow cytometric and spectrophotometric analysis of

caffeine interaction with novantrone, doxobubicin, ellipticine, and the doxorubicin analog AD198. Cancer Research 1991;51:3682.

[33] Wang L, Li Y-F, Zhou L, Liu Y, Meng L, Zhang K, Wu X, Zhang L, Li B, Chen C. Characterization of gold nanorods in vivo by integrated analytical techniques: their uptake, retention, and chemical forms. Analytical and Bioanalytical Chemistry 2010;396:1105.